

Contents lists available at ScienceDirect

Journal of Aerosol Science

journal homepage: www.elsevier.com/locate/jaerosci



Overview of methods to characterize the mass, size, and morphology of soot

Timothy A. Sipkens ^a, Adam Boies ^b, Joel C. Corbin ^a, Rajan K. Chakrabarty ^c, Jason Olfert ^d, Steven N. Rogak ^{e,*}

- ^a National Research Council Canada, 1200 Montreal Road, Ottawa, K1A 0R6, Ontario, Canada
- ^b Engineering Department, University of Cambridge, Trumpington Street, Cambridge, CB2 1PZ, United Kingdom
- ^c Department of Energy, Environmental and Chemical Engineering, Washington University, 1 Brookings Drive, St. Louis, 63130-4899, MO, USA
- ^d Department of Mechanical Engineering, University of Alberta, 10-340 Donadeo Innovation Centre for Engineering, Edmonton, T6G 2H5, Alberta, Canada
- ^e Department of Mechanical Engineering, University of British Columbia, 6250 Applied Science Lane, Vancouver, V6T 1Z4, British Columbia, Canada

ARTICLE INFO

Editor: Dr. Chris Hogan

Keywords:
Combustion aerosols
Soot
Morphology
Electron microscopy
Light scattering
Aerosol classifiers

ABSTRACT

Combustion and other high-temperature processes can produce solid aerosol nanoparticles with complex morphologies, including fractal-like aggregates of primary particles. Characterizing these morphologies, as well as particle mass, is key to understanding their behavior in natural and engineered systems, and it can provide clues to the origin of the particles. We focus here on the characterization of soot, although most of the techniques apply to other aerosol aggregates. A complete description of these aerosols would include the mass and morphology of every particle. In practice, it is possible to obtain detailed information on individual particles from microscopy of extracted samples. A particular focus of this review, tandem classifier/detector systems can determine 2-dimensional mass and mobility distributions that may be interpreted through the lens of fractal models. Very fast in situ light scattering measurements can be used to determine the structure factor, related to fractal dimension, and the aggregate and primary particle size distributions. These approaches are complementary when there are appropriate models to connect morphological details to optical and transport characteristics of the particles. Over the last few decades these models have become more sophisticated, requiring more information on the particle structure and properties, but also facilitating more sophisticated inferences from in-situ and online measurement techniques.

1. Introduction

Combustion-generated particles have a broad range of impacts, ranging from climate science (Arias et al., 2021; Pöschl, 2005; Stocker, 2014) to human health (Lighty, Veranth, & Sarofim, 2000) to engineered nanomaterials (Li, Shao, et al., 2016). Brownian coagulation of solid particles making up these aerosols, combined with surface growth, oxidation, fragmentation, and rearrangement, produces non-spherical shapes. This morphology affects our interpretation of measurements, the impact of these particles in the environment (Baker, Tyler, & Galloway, 2014; Rastogi et al., 2017), particle toxicity (Sengul & Asmatulu, 2020), and particle utility as an additive (Naseem & Durrani, 2021). In some cases, the structures are distinctive and may provide clues as to the origin of

E-mail address: rogak@mech.ubc.ca (S.N. Rogak).

^{*} Corresponding author.

Nomenclatur	e	
Symbols		
A_{pa}	Projected area of aggregate	
$\beta_{ m abs}$	Absorption coefficient	
β_{ext}	Extinction coefficient	
$\beta_{\rm sca}$	Scattering coefficient	
C_{c}	Cunningham slip correction	
χ	Dynamic shape factor	
$C_{ m ov}$	Coefficient of overlap (of primary particles)	
d_{A}	Projected area-equivalent diameter	
d_{ae}	Aerodynamic diameter	
D_{α}	$N_{\rm p} - A_{\rm pa} - d_{\rm p}$ exponent	
$D_{ m E}$	Euclidean dimension	
$D_{ m f}$	Fractal dimension	
$d_{ m g}$	Geometric mean diameter, GMD	
D_{m}	Mass-mobility exponent	
$d_{ m m}$	Mobility diameter	
$d_{ m p}$	Primary particle diameter	
D_{TEM}	TEM dimension	
$d_{ m ve}$	Volume-equivalent diameter	
k_{α}	$N_{\rm p} - A_{\rm pa} - d_{\rm p}$ prefactor	
$k_{ m f}$	Fractal prefactor	
Λ	Instrument transfer function	
λ	Wavelength, of light	
$\lambda_{ m g}$	Mean free path of gas	
m	Complex index of refraction	
$m_{ m p}$	Single/individual particle mass	
μ	Gas viscosity	
$N_{ m p}$	Number of primary particles in an aggregate	
$\Omega^{}$	Solid angle	
$R_{\rm g}$	Radius of gyration, $R_{g,2D}$ is 2D variant	
ρ	Density function, see Eq. (2)	
$ ho_0$	Standard density (or water), $\rho_0 = 1000 \text{ kg/m}^3$	
$ ho_{ m eff}$	Effective density	
$ ho_{ m m}$	Material density	
$R_{ m m}$	Classifier resolution	
$\sigma_{ m g}$	Geometric mean diameter	
$\sigma_{ m abs}$	Absorption cross-section of primary particle	
$\sigma_{ m abs}$	Absorption cross-section	
$\sigma_{ m ext}$	Extinction cross-section	
$\sigma_{ m sca}$	Scattering cross-section	
τ	Particle relaxation time	
θ	Scattering angle	
$Z_{ m p}$	Electrical mobility	
A^{P}	Area, disambiguation	

the particles and the physical processes involved in their formation. These complex structures can arise in combustion-generated particles composed of various materials, including metal oxides (Camenzind, Caseri, & Pratsinis, 2010; Li, Ren, Biswas, & Stephen, 2016; Pratsinis, 1998; Strobel, Baiker, & Pratsinis, 2006; Teoh, Amal, & Mädler, 2010) and carbon, the latter of which itself includes a range of particle types including carbon nanoparticles (Graves et al., 2020; Kim, Mulholland, Kukuck, & Pui, 2005), tarballs (Pósfai et al., 2004), and soot. This review focuses on soot, even if many of the discussed approaches below are applicable to other solid nanoparticles.

$A_{s,m}$	Diffusion-based surface area
$A_{\rm s}$	Surface area
B	Mechanical mobility
$C(\mathbf{r})$	Density correlation, where \mathbf{r} is radius from center of mass
D	Exponent/dimension
d	Particle diameter
D_{β}	$N_{\rm p}-2R_{\rm g}-d_{\rm m}$ exponent
d_{cmd}	Count median diameter
$D_{ m m,0}$	$N_{\rm p}-d_{\rm m}-d_{\rm p}$ exponent
$d_{ m mmd}$	Mass median diameter
d_{opt}	Optical diameter
$d_{\rm p,100}$	Primary particle diameter of a $d_A = 100$ nm particle
e	Elementary charge
$E(\mathbf{m})$	Absorption function
$F(\mathbf{m})$	Scattering function, square of Lorenz-Lorenz factor
$G(\cdot)$	Scattering cross-section form factor
h	Absorption correction, ratio of RDG-FA to measured
I	Scattering intensity
i	$\sqrt{-1}$ or measured current (Section 4.4)
k	Mass-mobility prefactor
L	Length of aggregate, from TEM
l	Measurement path length, optical
M	Mass concentration
M_2	2nd moment of the distribution
$M_{\rm v}$	vth moment of size distribution
m_{100}	Mass of a $d_{\rm m} = 100$ nm particle
N	Number concentration
n	Number of elementary charges
$N_{\rm a}$	Number of aggregates
P	Perimeter of aggregate, from TEM
Q	Optical efficiency
q	Particle charge or Q-factor (Section 6)
$R_{\rm s}$	Smoluchowski radius
r_{12}	Distance between two primary particles
S	Particle size
$S(q, R_{\rm g})$	Structure factor, optical
s *	Classifier size setpoint
$V_{ m pr}$	Probe volume
\dot{W}	Width of aggregate, from TEM
x	Size parameter, optics
$x_{\rm a}$	Size parameter, with respect to aggregate size
$x_{\rm p}$	Size parameter, with respect to primary particle
Y	Quantity of particles, e.g., number or mass
Kn	Knudsen number
Acronyms	
AAC	Aerosol Aerodynamic Classifier
AAE	Absorption Ångström exponent

The term *soot* has meant different things over time and in different research and engineering communities. Reviews by Petzold et al. (2013) and Michelsen et al. (2020) provide consistent discussions of the nomenclature, although the first is centered on atmospheric impacts research and the second on combustion and soot formation. Here, we use the term soot to mean *mature* soot

AMS Aerosol mass spectrometer
APM Aerosol Particle Mass Analyzer
APS Aerodynamic Particle Sizer

BC Black carbon

BET Brunauer–Emmett–Teller analysis

CAPS Cavity attenuated phase shift spectroscopy
CCN Cloud condensation nuclei counter

CMAD Count median aerodynamic diameter

CMD Count median diameter
CPC Condensation particle counter
CPMA Centrifugal Particle Mass Analyzer
DBS Diffusion broadening spectroscopy
DDA Discrete dipole approximation
DLCA Diffusion-limited cluster aggregation

DLS Dynamic light scattering
DMA Differential mobility analyzer
DMPS Differential mobility particle sizer

DMS Differential mobility spectrometer, e.g., DMS500

EEPS Engine exhaust particle sizer
ELPI Electrical Low Pressure Impactor

ELS Elastic light scattering
ELS Elastic light scattering

FIMS Fast integrated mobility spectrometer

FMPS Fast mobility particle sizer **GMD** Geometric mean diameter GSD Geometric standard deviation LAS Laser Aerosol Spectrometer LEO Leading-edge-only, for SP2 LII Laser-induced incandescence LOSA Line-of-sight attenuation LPI Low pressure impactor

M2AS Mass & Mobility Aerosol Spectrometer
MAAP Multi Angle Absorption Photometer

MAC Mass absorption coefficient

MAELS Multiangle elastic light scattering, interchangeable with MALS

MALS Multiangle light scattering MEC Mass extinction coefficient

MMAD Mass median aerodynamic diameter

MMD Mass median diameter

MOUDI Microorifice uniform deposit impactor

MSC Mass scattering coefficient
MSTM Multiple sphere T-matrix
OPC Optical particle counter
OPS Optical Particle Sizer
PAX Photoacoustic Extinctiometer

PAX Photoacoustic Extinctiometer
PCS Photon correlation spectroscopy

PMA Particle mass analyzer

PSAP Particulate Soot Absorption Photometer

PSL Polystyrene latex (spheres)
QELS Quasi-elastic light scattering

RDG-FA Rayleigh Debye Gans-fractal aggregate theory

as defined by Michelsen et al. (2020), which are light absorbing particles with a complex morphology. Such particles often account

for most of the light absorption by atmospheric aerosols, and are often referred to in atmospheric science as black carbon.

SAXS	Small angle X-ray scattering				
SELPI	Single-stage ELPI				
SEM	Scanning electron microscope				
SEMS	Scanning electrical mobility spectrometer				
SMPS	Scanning mobility particle sizer				
SP2	Single-Particle Soot Photometer				
SPC	Single particle counter, another name for an OPC				
SPMS	Single-particle mass spectrometry				
SSA	Single scattering albedo				
STEM	Scanning transmission electron microscopy				
STM	Scanning tunneling electron microscopy				
TDMA	Tandem differential mobility analyzer				
TEM	Transmission electron microscope				
TEOM	Tapered element oscillating microbalance				
TOF	Time of flight				
TOF-AMS	Time of flight-aerosol mass spectrometer				
UHSAS	Ultra-High Sensitivity Aerosol Spectrometer				
USAXS	Ultra small angle X-ray scattering				
WALS	Wide angle light scattering				

Soot exists as aggregates of primary particles. The term *aggregate* usually refers to clusters of strongly bonded, overlapping primary spheres while *agglomerates* refers to weakly bonded primary particles with point contacts (Eggersdorfer & Pratsinis, 2014). We use the term *aggregates* throughout while acknowledging that real soot can contain features of agglomerates and aggregates. We also use the term *typical* soot to describe those properties of soot which have been observed to remain similar on average, across a range of combustion sources and conditions. While unusual sources and conditions can lead to unusual properties, it is essential to describe the properties of typical soot before such exceptions can be identified. In addition, soot is often internally mixed with other materials, such as semivolatile organics or inorganics like sulfate. The characterization of such *coatings* is complex, and is not considered in this review (for this topic, see the review of Riemer, Ault, West, Craig, and Curtis (2019)).

This review focuses on the measurement of the mass, *equivalent diameters*, and morphology (of features larger than a nanometer) for individual soot particles. We focus on the properties of single particles and the corresponding distributions. Where appropriate, we also mention how those properties influence aggregate properties (mass concentration, total light scattering, size distributions), especially when the specific properties of soot play a role. Soot morphology can vary substantially during formation, as particles undergo clustering, inception, and growth of primary particles (Kelesidis, Goudeli, & Pratsinis, 2017a; Thomson, 2022), or after internal mixing causes further restructuring (Corbin, Modini, & Gysel-Beer, 2023; Enekwizu, Hasani, & Khalizov, 2021). Therefore, a sound characterization of the mass, size, and morphology of soot is often necessary understand the processes behind combustion aerosol formation, or the interaction of soot particles with the environment.

The majority of research efforts in characterizing combustion-generated aggregates make use of three complementary approaches: microscopy, aerosol classification and detection, and optical characterization. Connecting these methods are theoretical models of morphology and particle physical properties (e.g., transport phenomena, light scattering). Further, woven into these models are material properties (e.g., density, refractive index), which we assume here are known *a priori* or might possibly be inferred from the physical measurements. Particle chemical composition and nanostructure also play an important role but are outside the scope of our review. For soot chemistry and nanostructure, we refer the reader to previous reviews (Appel, Bockhorn, & Frenklach, 2000; Michelsen et al., 2020).

This review is structured as follows. For each topic, we include an abridged introduction to a range of characterization techniques, while pointing out related reviews in the literature for readers who are new to the field. A timeline of such reviews is mapped out in Fig. 1. We start by defining what we desire in an adequate characterization of morphology and size, from theoretical and experimental perspectives (Section 2). Next, we discuss microscopy and image analysis (Section 3), which are laborious but provide tremendous detail on a relatively small number of particles. Following this, we review aerosol classifiers and detectors (Sections 4 and 5), which can be used in tandem to provide a useful level of detail on aerosol populations without the artifacts that might be present in sampling for microscopy. Finally, we review the use of optical diagnostics for complementary characterization (Section 6). Each section is written in such a way that the reader can begin at any one section, according to their interest.

2. Complete physical characterization of soot

The composition and morphological structure of soot (and other solid combustion aerosols) has been the focus of intense research. A truly complete characterization of particle morphology would involve specifying the coordinates of all points on a particle surface — which is neither practical nor necessary. A useful level of detail is one that helps us relate the various physical measurements of the

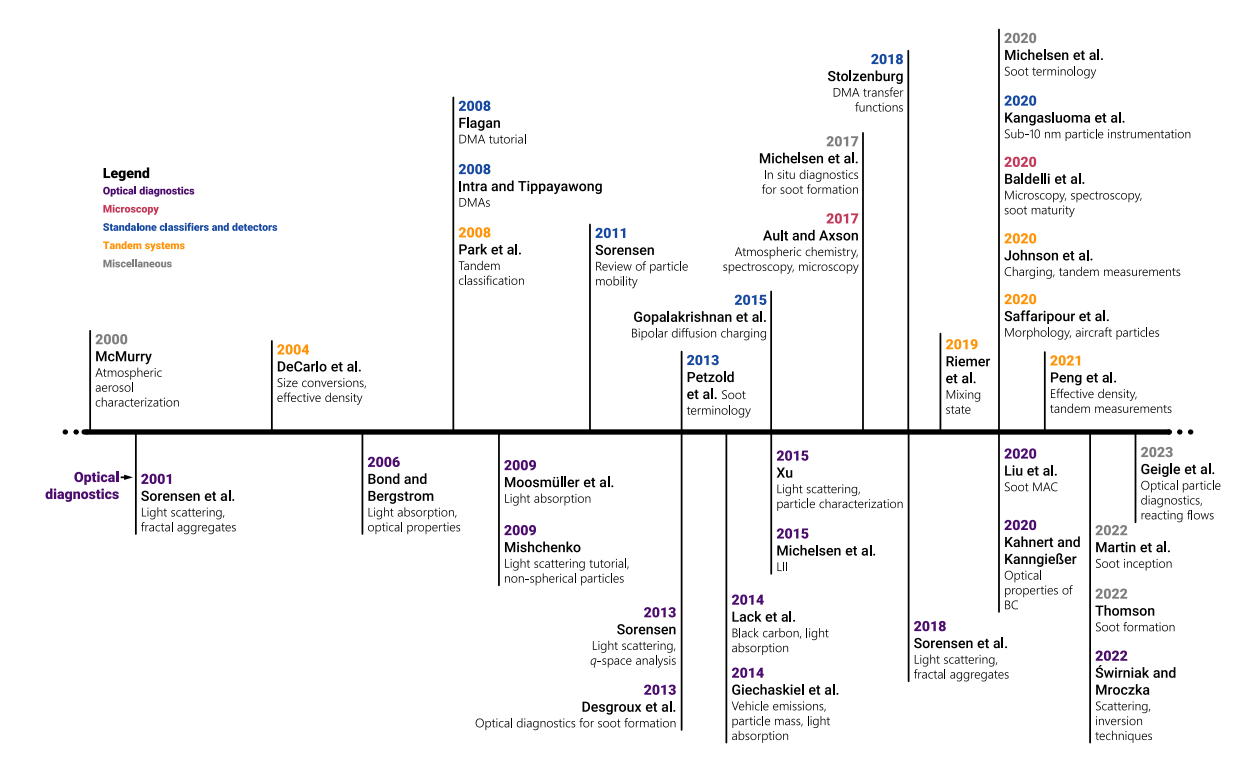


Fig. 1. Timeline of reviews related to characterization of carbonaceous, combustion-generated particles since 2000 (Ault & Axson, 2017; Baldelli, Trivanovic, Sipkens, & Rogak, 2020; Bond & Bergstrom, 2006; DeCarlo, Slowik, Worsnop, Davidovits, & Jimenez, 2004; Desgroux, Mercier, & Thomson, 2013; Flagan, 2008; Geigle, Migliorini, Yon, & Smallwood, 2022; Giechaskiel et al., 2014a; Gopalakrishnan, McMurry, & Hogan Jr., 2015; Intra & Tippayawong, 2008; Johnson et al., 2020; Kanngießer, 2020; Kangasluoma et al., 2020; Lack, Moosmüller, McMeeking, Chakrabarty, & Baumgardner, 2014; Liu, Yon, et al., 2020; Martin, Salamanca, & Kraft, 2022; McMurry, 2000; Michelsen, 2017; Michelsen et al., 2020; Michelsen, Schulz, Smallwood, & Will, 2015; Mishchenko, 2009; Moosmüller, Chakrabarty, & Arnott, 2009; Park et al., 2008; Peng et al., 2021; Petzold et al., 2013; Riemer et al., 2019; Saffaripour, Thomson, Smallwood, & Lobo, 2020; Sorensen, 2001, 2011, 2013; Sorensen et al., 2018; Stolzenburg, 2018; Świrniak & Mroczka, 2022; Thomson, 2022; Xu, 2015). Acronyms include differential mobility analyzer (DMA), laser-induced incandescence (LII), mass absorption coefficient (MAC), and black carbon (BC).

aerosols to one another. As measurements and models become more sophisticated, therefore, the notion of *complete* characterization expands. Fig. 2 illustrates some of the aggregates that can be produced by current aggregation simulations, with varying size of primary particles (b and d) and allowances for surface growth that results in primary particles that overlap strongly (c). Fig. 2 adds annotations for several equivalent diameters, discussed at length later. The definition of *primary particles* is a convenient way to understand this particle morphology, even if individual primary particles may be difficult to discern in practice (e.g., see discussion in Section 3 on electron microscopy). Alternative ways to represent this morphology are one way in which *complete* characterization may continue to evolve.

2.1. Fractal nature of an aggregate

We continue under the assumption that the particles under consideration here are aggregates of primary particles reasonably described by diffusion-limited cluster aggregation (DLCA). This process gives rise to mass fractal structures with a fractal dimension around $D_{\rm f}\approx 1.8$. The smallest soot particles in a flame are typically much smaller than their diffusional mean free path, hence the growth process is better described by ballistic cluster-cluster aggregation (Meakin, 1999), which would result in a fractal dimension around $D_{\rm f}\approx 1.9$. However, as aggregates grow to 10-s of nanometers, their diffusional mean free path decreases rapidly and the DLCA model is more appropriate. This has been known for over 40 years (Forrest & Witten, 1979), with some broader review by Sorensen (2011), and is well described through computer simulations of aggregation (Meakin, 1987; Mountain, Mulholland, & Baum, 1986). The fundamental scaling relation for a mass fractal relates the number of primary particles, $N_{\rm p}$, to the radius of gyration, $R_{\rm g}$, and the primary particle diameter, $d_{\rm p}$:

$$N_{\rm p} = k_{\rm f} \left(\frac{2R_{\rm g}}{d_{\rm p}}\right)^{D_{\rm f}}.$$

Clearly, this relation loses meaning as N_p approaches 1, and generally one must be very cautious in applying the fractal model (and indeed many of the relations in this work) to aggregates of only a few primary particles. Fig. 3 compares simulated aggregates with roughly equal N_p but different values of D_f and k_f . The algorithm used to produce Fig. 3 is a geometric model as opposed to a

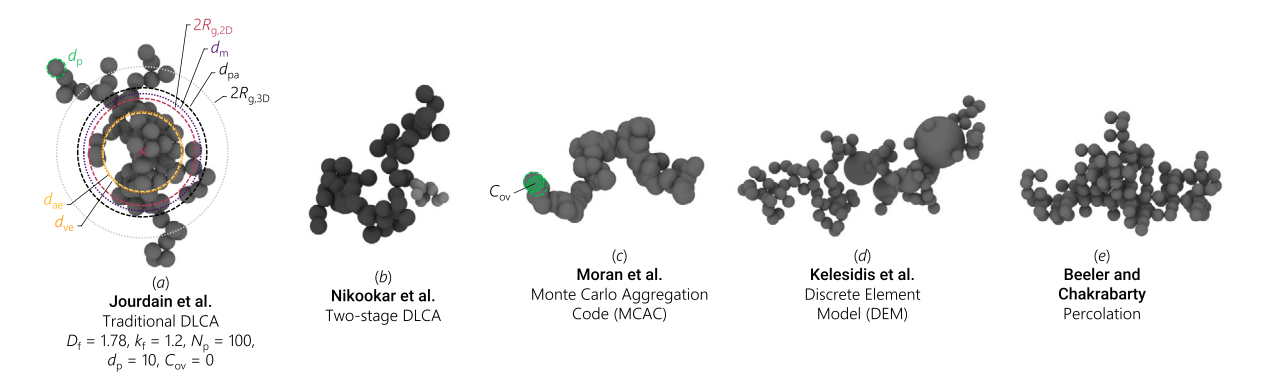


Fig. 2. A range of simulated soot particles exhibiting typical fractal aggregate morphologies. Panels: (a) commonly-used equivalent sphere sizes (Jourdain, Symonds, & Boies, 2023) (b) primary particle sizes highly uniform within subregions of the aggregate; (c) overlapping primary particles (Morán, Yon, Poux et al., 2020; Morán, Yon, Poux, Corbin et al., 2020); (d) effects of preferential surface growth (Kelesidis, Goudeli, & Pratsinis, 2017b) (here, very large spheres represent compact clusters of primary particles); and (e) generated by percolation (Beeler & Chakrabarty, 2022). Coordinate files for these aggregates are included in the supplemental information.

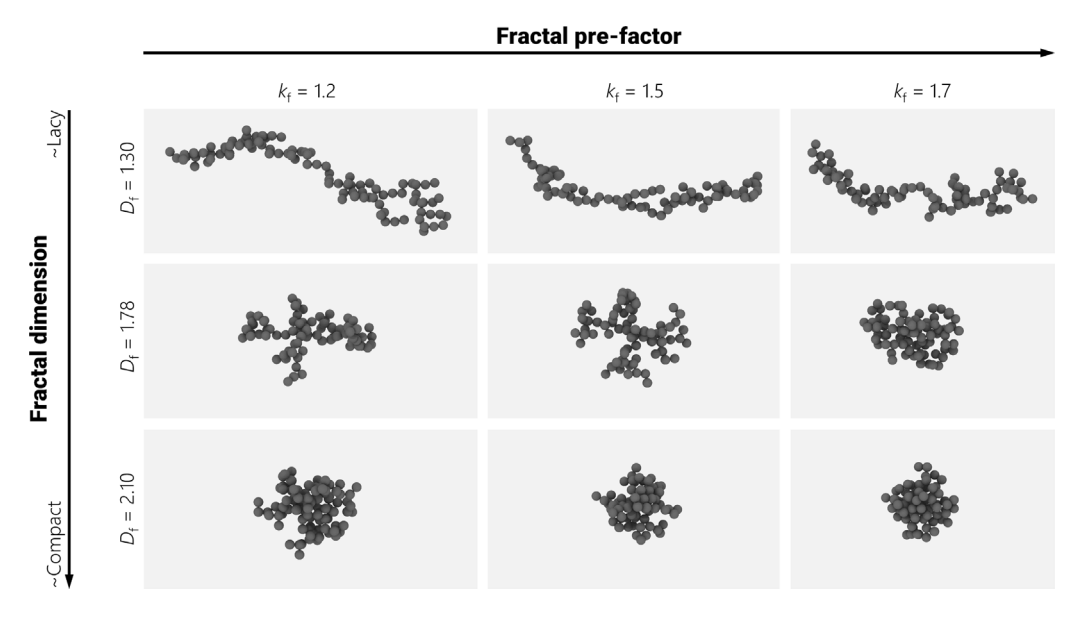


Fig. 3. Demonstration of the impact of the prefactor, k_f , and fractal dimension, D_f , using simulated aggregates generated by a sequential tunable algorithm (Jourdain et al., 2023). Both quantities control the appearance of fractal aggregates, including whether the aggregates are lacy or compact, with k_f acting as a baseline compactness without consideration to particle size. Typically, changes with D_f are more significant for the values relevant to soot aggregates. Coordinate files for these aggregates are included in the supplemental information. See also similar figures in a number of other works (Liao, Selomulya, Bushell, Bickert, & Amal, 2005; Liu, 2019; Moghaddam, Hadwin, & Daun, 2017; Prasanna, Rivière, & Soufiani, 2014).

mechanistic model, and it represents the range of variations that can occur (Jourdain et al., 2023). Higher values $D_{\rm f}$ are associated with the appearance of higher density, while higher values of $k_{\rm f}$ are associated a less stringy appearance and more compact local structure (Heinson, Sorensen, & Chakrabarti, 2010; Melas, Isella, Konstandopoulos, & Drossinos, 2014). Liu and Chakrabarty (2016) established empirical relationships between $k_{\rm f}$ and $D_{\rm f}$ for simulated aggregates in the free molecular and the transition flow regimes. The combined effects of $k_{\rm f}$ and $D_{\rm f}$ on overall density should be acknowledged or else anomalous results for $D_{\rm f}$ may result. For example, some aggregates in a soot population may have a very high aspect ratio, which could be interpreted as low $D_{\rm f}$ (Chakrabarty et al., 2009). However, DLCA simulations do in fact produce some aggregates with this appearance, which scale with $D_{\rm f} \approx 1.8$ but have a low $k_{\rm f}$ (Heinson et al., 2010).

Various physical processes do affect the morphology of aggregates. Coagulation with strong magnetic or electric forces can result in low fractal dimensions. By contrast, very high fractal dimensions often result from the restructuring and collapse of aggregates due to the surface tension of liquids condensed on the aggregate surface (Corbin et al., 2023; Ghazi, Tjong, Soewono, Rogak, & Olfert, 2013; Zangmeister et al., 2014). Surface growth and slow coalescence can be important processes in the early stages of soot formation, and several groups have simulated their effects on structures, e.g., Al Zaitone, Schmid, and Peukert (2009) and Kelesidis et al. (2017b). Experimentally, it has been shown that surface growth can increase the effective density of soot (Wang,

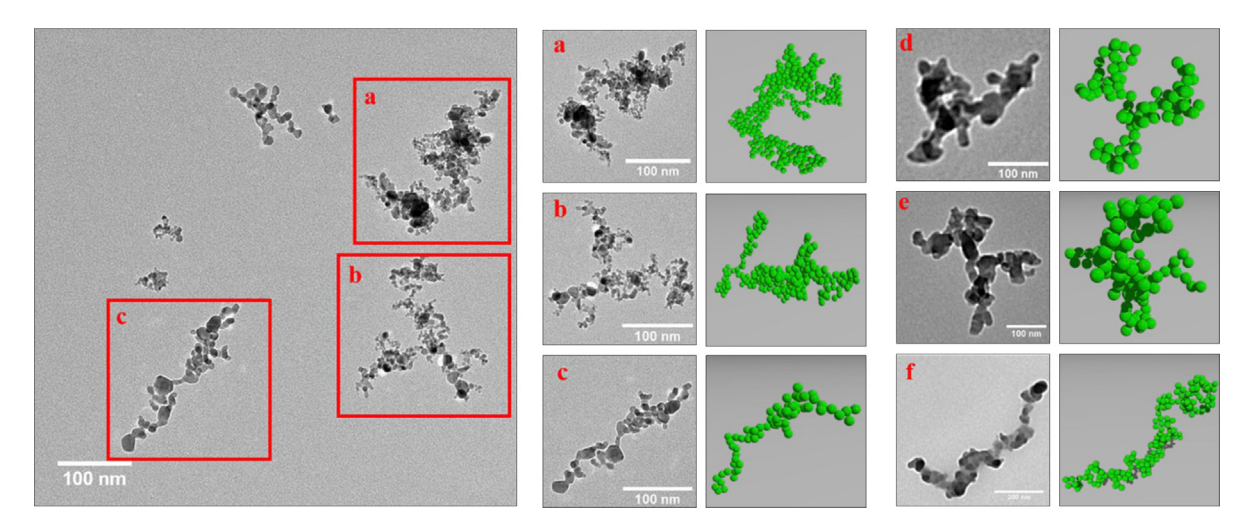


Fig. 4. Soot-like aggregates beside their equivalent simulated results generated via a cluster-cluster aggregation model. Source: Adapted from Qiao et al. (2020).

Tang, Mei, & You, 2018), but it is unclear to what extent this should be attributed to an increase in overlap, fractal dimension, and prefactor, or as a reduction in the number of primary particles. A further limitation of traditional aggregation simulations is that, in typical non-premixed flames, on the order of 99% of the soot that forms is destroyed by oxidation, and relatively few simulations have considered this oxidation processes (and then only in a highly simplified fashion (Qian et al., 2023)). Despite omitting this important process, which must result in both shrinkage of primary particles and fragmentation of aggregates (Ghiassi, Toth, Jaramillo, & Lighty, 2016), DLCA aggregates closely resemble fresh soot (see Fig. 4), which makes them useful models in the interpretation of real measurements.

For length scales between d_p and R_g , DLCA aggregates appear self-similar which implies a certain form for the density–density correlation function C(r),

$$C(r) = \langle \rho(\mathbf{r}_0) \cdot \rho(\mathbf{r}_0 + \mathbf{r}) \rangle, \tag{2}$$

where \mathbf{r} is a radius from the center of mass of the particle, ρ is a density having a value of 1 inside the aggregate material and 0 outside it, and $\langle \cdot \rangle$ denotes averaging over all reference positions \mathbf{r}_0 and all orientations of \mathbf{r} . For a fractal, this function will exhibit power law scaling that depends on the Euclidean dimension $D_{\rm E}$ ($D_{\rm E}=3$ in real space, $D_{\rm E}=2$ for images) as well as the fractal dimension (Meakin, 1987), $D_{\rm f}$, where

$$C(r) \sim r^{D_{\rm f} - D_{\rm E}} \tag{3}$$

This relation only applies to intermediate length scales; for scales larger than R_g , the correlation must fall off faster than this power law; for length scales below the primary particle diameter, $C(r) \sim 1$. The correlation function is the basis for estimating the fractal dimension from the internal structure of an individual aggregate, for example by the box-counting approaches discussed later. Furthermore, the Fourier transform of C(r) results in the structure factor S(q), primarily responsible for determining the angular dependence of light scattering from fractal aggregates (see also Section 6.3).

The scaling of the density correlations determines how much of the structure is visible in a 2D projection. Fractals with $D_{\rm f} < 2$ are "asymptotically transparent", meaning that for large aggregates, a large (and constant) fraction of the primary particles are visible in a 2D projection. Aggregates with $D_{\rm f} > 2$ are asymptotically opaque, meaning that as aggregate size increases, the fraction of visible primary particles decreases to zero. Practically this means that image processing may be used to determine the fractal dimension only if $D_{\rm f} < 2$; for higher fractal dimensions (e.g., collapsed soot) we are limited to qualitative descriptions. This divide at $D_{\rm f} = 2$ applies to the transport properties of aggregates, which, in the kinetic (free-molecule) limit, depends on the projected area. Namely, for $D_{\rm f} < 2$, the projected area will scale with particle mass, but, for $D_{\rm f} > 2$, it will scale with $m_{\rm p}^{2/D_{\rm f}}$. In practice, near $D_{\rm f} = 2$, finite size effects have a huge influence on the scaling behavior of aggregate properties. Even for DLCA aggregates (which should be asymptotically transparent), as aggregate size increases, an increasing number of primaries are obscured by other primaries, so $N_{\rm p}$ is inevitably underestimated unless a correction factor is applied. A widely-used correction is given as

$$N_{\rm p} = k_{\alpha} \left(\frac{d_{\rm A}}{d_{\rm p}}\right)^{2D_{\alpha}},\tag{4}$$

where d_A is the projected area-equivalent diameter. Interestingly, this type of shielding relation was applied to carbon black (Medalia & Heckman, 1971) before the fractal model was developed. The parameters in the shielding correction are commonly taken as $k_\alpha = 1.16$ and $D_\alpha = 1.1$, however D_α ranges from 1.08 to 1.11 (as the overlap coefficient, C_{ov} , defined below, ranges from 0 to 0.15,

Brasil, Farias, & Carvalho, 1999). This shielding effect has also been expressed as the ratio of the projected area of the aggregate to the projected area of all the constituent primary particles (Meakin, Donn, & Mulholland, 1989). Broadly, the two representations are consistent for aggregates with $N_p > 10$ but it should be noted that the most commonly used corrections were obtained for DLCA aggregates with uniformly-sized primary particles. However, more recent simulations (Al Zaitone et al., 2009; Eggersdorfer, Kadau, Herrmann, & Pratsinis, 2012) suggest that D_a is surprisingly insensitive to sintering, surface growth, and primary particle polydispersity.

This fractal structure is exhibited by soot, submicron fly-ash, and pigments of metal oxides formed in thermal reactors. In all cases, the primary particles are formed in the earlier stages of the process under conditions that lead to the formation of liquid particles, which coalesce during coagulation, or with very high surface growth rates, which also tends to form spherical particles. Given that the processes that form primary particles occur (at least partly) while aggregation occurs, the primary particles in real aggregates are not perfect spheres with point contacts but rather show different degrees of "overlap" or "necking" (Brasil et al., 1999; Oh & Sorensen, 1997). The overlap between two primary particles of diameter $d_{\rm p,1}$ and $d_{\rm p,2}$ is characterized by the overlap coefficient,

$$C_{\text{ov}} = (d_{\text{p,1}} + d_{\text{p,2}} - 2r_{12})/(d_{\text{p,1}} + d_{\text{p,2}}),$$
 (5)

where r_{12} is the distance between the centers of the two primary particles. Because primary particles typically overlap, determining the size and number of primary particles, for example by microscopy, is challenging and even subjective.

Primary particles are also not all the same size because there are (typically) spatial variations in the particle formation conditions and because the coagulation process inevitably produces a polydisperse aerosol. The variation in primary particle size within an aggregate is typically quite small, while the variation from one aggregate to another is typically much larger. There is also often a significant correlation between aggregate size and primary particle size. This had been noted for carbon black long ago (Medalia & Heckman, 1971)¹ but only recently formalized for soot (Dastanpour & Rogak, 2014; Olfert & Rogak, 2019). A best-fit derived from TEM images of soot from non-premixed combustion is (Olfert & Rogak, 2019):

$$d_{\rm p} = d_{\rm p,100} \left(\frac{d_{\rm A}}{100 \text{ nm}}\right)^{D_{\rm TEM}} \tag{6}$$

where $D_{\rm TEM} \approx 0.35$ and $d_{\rm p,100} = 17.8$ nm. If the primary particle size varies systematically with aggregate size, then the application of Eq. (1) is not straightforward. This issue is discussed further in Section 3. Soot from premixed combustion would be expected to have $D_{\rm TEM} = 0$, and there is some experimental evidence for this, e.g., Slowik et al. (2007). Recent measurements of soot produced by flame spray pyrolysis with globally fuel-rich conditions did not show a correlation between $d_{\rm p}$ and $d_{\rm A}$ for individual operating conditions, but as equivalence ratio was increased, $d_{\rm p}$, $d_{\rm A}$ and soot maturity increased together (Trivanovic, Kelesidis, & Pratsinis, 2022).

In this review we wish to highlight practical measurement approaches. All of the parameters discussed above can (with some difficulties and approximations) be determined by microscopy as discussed in Section 3. In Section 6, we also discuss optical approaches to measure $D_{\rm f}$, $d_{\rm p}$, and $R_{\rm g}$, albeit with many simplifying assumptions. Fresh soot from a combustion source often has the appearance of the simulated DLCA aggregates produced by coagulation with perfect sticking (i.e., $D_{\rm f} \rightarrow 1.8$, Fig. 3). This facilitates interpretation of mobility measurements. Restructuring to a compact shape ($D_{\rm f} \rightarrow 3$, Fig. 3, bottom row) would conserve the volume-equivalent diameter, decrease the mobility diameter, and increase the aerodynamic diameter. Thus, *sizing*, as discussed below and in Section 4, can be used to infer morphological features of individual aggregates and populations of aggregates.

A common theme throughout the discussion thus far has been the emergence of a wide range of *dimensions* or exponents relating various characteristics of the particles, including D_f , D_a , and D_{TEM} , with additional variants discussed in the sections following and identified in Fig. 5. Most of these dimensions can be related to one another by way of various assumptions, which can be regime-specific. The key parameters, and typical reported ranges, used in this review are summarized in Table 1.

2.2. Sizing of individual aggregates

For non-spherical aggregates, the measurement of particle size is described by *equivalent* diameters. A particle's equivalent diameter is defined as the diameter of a standard-density sphere that would result in an identical measurement. Different measurement techniques correspond to different equivalent diameters. The interplay between these different equivalent diameters gives an indication of the shape of the particles, which has been carefully reviewed by DeCarlo et al. (2004). A range of these equivalent sizes for *typical* soot, as will be discussed in the sections that follow, is shown in Table 2.

¹ This 1971 article was rediscovered by the authors in the process of preparing this review. Interestingly, Medalia and Heckman's Figure 9 summarizes primary particle size distributions as a function of area, and the relation is best fit with $d_{\rm p,100}=19~{\rm nm}$ and $D_{\rm TEM}=0.36$.

Table 1 Values for the properties of *typical*, fresh soot, noting that variations can occur depending on the combustion and sampling conditions. For paired values in power laws – including (k_f, D_f) , $(\rho_{eff,100}, D_m)$, and $(d_{p,100}, D_{TEM})$ – quantities will be correlated. Relevant literature should be consulted for original values, including extended discussion of restrictions. The quantity $D_{m,0}$ differs from D_m based on its use and underlying assumptions about the primary particle size (see also Fig. 5). See also a complementary summary of the values presented by Johnson, Devillers, and Thomson (2013).

Parameter	Symbol	Value	Range	Units	Literature
Material density	$ ho_{ m m}$	1860, 1800 ^a	1620–2200 ^b	kg/m³	Ouf, Bourrous, Fauvel et al. (2019a) and studies therein; Johnson et al. (2013) and studies therein; older sources include: Lide (1992), Mullins and Williams (1987), Park, Kittelson, Zachariah, and McMurry (2004), Wu, Krishnan, and Faeth (1997)
Fractal dimension	$D_{ m f}$	1.78	$1.63-1.90^{\circ}$	-	Johnson et al. (2013), Sorensen (2011)
Fractal prefactor	k_{f}	1.3	1.10-2.5	_	Sorensen (2011), Sutcu et al. (2020)
$N_{\rm p} - A_{\rm pa} - d_{\rm p}$ exponent	D_{α}	1.10	1.08–1.11	-	Brasil et al. (1999), Köylü, Faeth, Farias, and Carvalho (1995)
$N_{\rm p}-A_{\rm pa}-d_{\rm p}$ prefactor	k_{α}	1.16	-	-	Brasil et al. (1999), Köylü et al. (1995)
Coefficient of overlap	$C_{ m ov}$	0.14	0-0.20	-	Brasil et al. (1999), Ouf, Bourrous, Vallières, Yon, and Lintis (2019b)
TEM dimension	D_{TEM}	0.35	0.10-0.55 ^d	-	Dastanpour and Rogak (2014), Olfert and Rogak (2019), Trivanovic et al. (2020)
Primary particle diameter ($d_A = 100 \text{ nm}$)	$d_{\rm p,100}$	17.8	14-30 ^d	nm	Dastanpour and Rogak (2014), Olfert and Rogak (2019), Trivanovic et al. (2020)
Mass-mobility exponent	D_{m}	2.48	2.29-2.78 ^d	-	Olfert and Rogak (2019), Trivanovic et al. (2020)
Effective density ($d_{\rm m} = 100 \text{ nm}$)	$ ho_{ m eff,100}$	510	450-700 ^d	kg/m ³	Olfert and Rogak (2019), Saffaripour et al. (2020)
Single-particle mass ($d_{\rm m} = 100 \text{ nm}$)	m_{100}	0.267	0.236-0.367	fgc	Olfert and Rogak (2019), Trivanovic et al. (2020)
Dynamic shape factor ($d_{\rm m} = 100 \text{ nm}$)	X100	2.15 ^e	1.7-2.3 ^e	_	Olfert and Rogak (2019) ^e
$N_{\rm p} - d_{\rm m} - d_{\rm p}$ exponent	$D_{\mathrm{m.0}}$	2.2	_	_	Sorensen (2011)
$N_{\rm p} - 2R_{\rm g} - d_{\rm m}$ exponent	D_{β}	1/0.107	_	_	Sorensen (2011)
GSD (with respect to $d_{\rm m}$)	$\sigma_{ m g}^{'}$	-	1.5–2.5	_	Harris and Maricq (2001), Kazemimanesh et al. (2019), Moallemi et al. (2019), Saffaripour et al. (2020), Stipe, Higgins, Lucas, Koshland, and Sawyer (2005)
Specific surface area	_	_	10-500	m^2/g	Ouf et al. (2019b)
Refractive index ($\lambda = 550 \text{ nm}$)	m	1.66 + 0.76i	_	-	Liu, Yon, et al. (2020)
Absorption function ($\lambda = 550 \text{ nm}$)	$E(\mathbf{m})$	0.32	0.24-0.42	-	Johnson et al. (2013), Liu, Yon, et al. (2020)
Mass absorption cross-section ($\lambda = 550 \text{ nm}$)	MAC	8.0	6.6–9.4	m^2/g	Chakrabarty and Heinson (2018), Johnson et al. (2013), Liu, Yon, et al. (2020)
Absorption Ångström exponent	AAE	1.0	0.8-1.2	-	Chakrabarty and Heinson (2018), Corbin et al. (2019), Török et al. (2018)

^aFor material density, $\rho_m = 1800 \text{ kg/m}^3$ is a common historical value, but we recommend the more recent consensus value $\rho_m = 1860 \text{ kg/m}^3$.

2.2.1. Particle volume and mass

The volume-equivalent sphere diameter, d_{ve} , is conceptually simple and can be estimated with Eq. (1), provided that we have information on the primary particle size distribution and the particle is well-approximated with the fractal model. As its name implies, d_{ve} is not typically measured directly. It is most often calculated when the particle mass, m_p , is measured for particles of known density, ρ_m , as (Hinds, 1999)

$$d_{\rm ve} = \left(\frac{6m_{\rm p}}{\rho_{\rm m}\pi}\right)^{1/3}.\tag{7}$$

Typical values for the $\rho_{\rm m}$ of soot are given in Table 1. If one adds the assumption of monodisperse, non-overlapping primary particles, one can also infer the number of primary particles by combining $d_{\rm ve}$ with knowledge of the primary particle diameter:

$$N_{\rm p} = \left(\frac{d_{\rm ve}}{d_{\rm p}}\right)^3. \tag{8}$$

^bThis range represents the larger, historical range of values observed across the literature. Uncertainties in the expected density are generally considered to be much lower (± 100 kg/m³), e.g., as in Liu, Yon, et al. (2020).

^cFractal dimensions above this range are often a sign of more compact or collapsed soot.

dRanges on these quantities are taken as the range observed by Olfert and Rogak (2019), with a minor update in some cases for data from Trivanovic et al. (2020) and/or Saffaripour et al. (2020).

eValue and range of the dynamic shape factor are computed from the effective density values (see also Table 2). Direct reporting of the dynamic shape factor is less common for fresh soot than compact soot and atmospheric studies, where the dynamic shape factor will exhibit smaller values, e.g., Pagels, Khalizov, McMurry, and Zhang (2009).

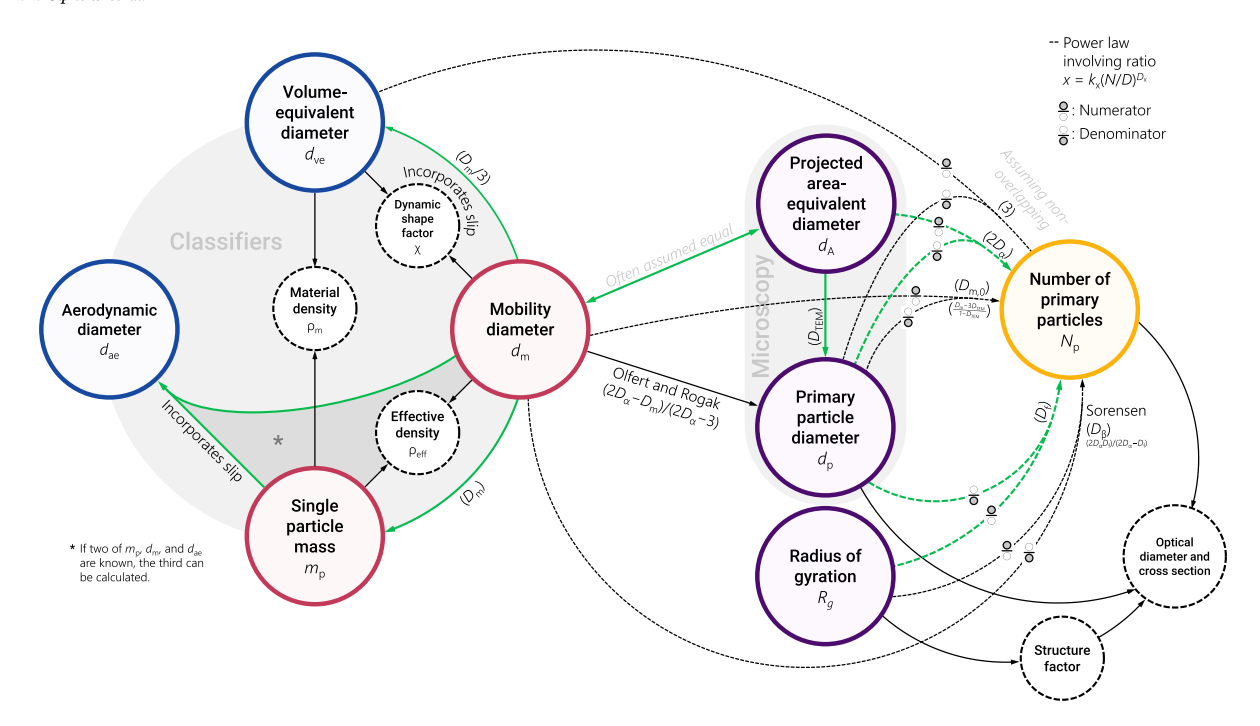


Fig. 5. Map of relationships between different particle sizes. Left portion of the figure contends with quantities targeted by classifiers, while the right portion of the figure is related to TEM characterization and optical diagnostics (e.g., N_p and R_g). Arrow directions show typical calculation directions or representations shown in the literature (e.g., where the corresponding exponent applies, such as $m_p = k d_{\rm m}^{D_{\rm m}}$) but can all be reversed. Green, bolded lines show the pathway used to compute the properties of *typical* soot in Table 2. (For interpretation of the references to color in this figure legend, the reader is referred to the web version of this article.)

Table 2 Equivalent particle sizes for *typical* soot aggregates in air given the mass-mobility and primary particle size correlations as parameterized by Olfert and Rogak (2019), including $D_{\rm m}=2.48$ and $D_{\rm TEM}=0.35$, with the latter used in conjunction with Eq. (6) to compute the primary particle size after assuming $d_{\rm m}=d_{\rm A}$. The number of primary particles, $N_{\rm p}$, is then computed by invoking Eq. (4) with $D_{\rm a}=1.1$ and $k_{\rm a}=1.16$. This results in a difference of 2% in $d_{\rm p}$ if one then invokes Eq. (8), which we attribute to primary particle overlap (Yon, Bescond, & Liu, 2015). The corresponding fractal dimension and prefactor for computing the radius of gyration are taken as $D_{\rm f}=1.78$ and $k_{\rm f}=1.35$. All quantities are stated to three significant figures. Cunningham slip correction is taken from Kim et al. (2005) as implemented in ISO 15900 (ISO, 2020a) for air, a temperature of 20 °C, and pressure of 1 atm.

, ,					· .			
Mobility diameter	Single particle mass	Effective density	Volume- equivalent diameter	Dynamic shape factor	Aerodynamic diameter	Primary particle diameter	Number of primary particles	Radius of gyration
d_{m}	$m_{\rm p}$	$ ho_{ m eff}$	d_{ve}	χ	d_{ae}	d_{p}	$N_{\rm p}$	$R_{\rm g}$
nm	fg	kg/m ³	nm	-	nm	nm	_ `	nm
20	0.00493	1180	17.2	1.35	23.4	10.1	5.18	10.8
30	0.0135	954	24.0	1.54	28.7	11.7	9.24	17.2
50	0.0479	731	36.6	1.80	37.8	14.0	19.2	31.0
75	0.131	592	51.2	2.01	47.8	16.1	34.3	49.5
100	0.267	510	65.0	2.15	57.3	17.8	51.7	69
200	1.49	356	115	2.42	93.7	22.7	139	153
300	4.07	288	161	2.52	129	26.1	249	245
500	14.5	221	246	2.59	198	31.3	516	442
750	39.5	179	344	2.65	276	36.0	922	705
1000	80.6	154	436	2.70	349	39.8	1390	982

When the particles overlap, there will be differences between this value of $N_{\rm p}$ and the one that may be estimated from TEM image analysis (Yon et al., 2015).

2.2.2. Particle mobility

A number of instruments classify particles by their drag for a given velocity, thereby determining the (mechanical) mobility, B (and, by extension, the mobility-equivalent diameter $d_{\rm m}$),

$$B = \frac{C_{\rm c}(d_{\rm m})}{3\pi\mu d_{\rm m}} \tag{9}$$

where μ is the gas viscosity and C_c is the Cunningham slip correction factor, which is a function of the diameter via the Knudsen number.

$$Kn = 2\lambda_v/d,$$
(10)

where λ_g is the mean free path of the gas. The slip correction can be evaluated using a number of parameterizations (Allen & Raabe, 1982, 1985; Davies, 1945; Kim et al., 2005), with the currently-prevailing parameterization given by Kim et al. (2005) and adopted in ISO 15900 (ISO, 2020a):

$$C_{\rm c} = 1 + {\rm Kn} \left[\alpha + \beta \exp\left(-\frac{\gamma}{{\rm Kn}}\right) \right],\tag{11}$$

where $\alpha=1.165$, $\beta=0.483$, and $\gamma=0.997$. This effect can also be quantified, to some extent, using some expressions for the friction factor (Sorensen, 2011; Zhang, Thajudeen, Larriba, Schwartzentruber, & Hogan Jr., 2012). Note that the mobility depends on gas properties which are functions of temperature and pressure, and therefore mobility diameter measurements should be referenced to the temperature, pressure, and background gas composition for the measurements. In the kinetic regime (Kn \gg 1), $d_{\rm m}$ is approximately $d_{\rm A}$, while in the continuum regime (Kn \rightarrow 0), $d_{\rm m}$ is proportional to $R_{\rm g}$. There is no general formula for the mobility of a fractal aggregate, but this has been the subject of extensive reviews (Sorensen, 2011), and work using direct simulation Monte Carlo (DSMC) (Zhang et al., 2012) provide complete estimation methods that are quite accurate — in fact, they are probably more accurate than the $d_{\rm A}$ and $R_{\rm g}$ determined by microscopy.

Electrical mobility is a related property that is of considerable interest given that it is relatively easy to measure. The electrical mobility is proportional to the mechanical mobility and the number of elementary charges carried by the particle, n,

$$Z_{\rm p} = \frac{neC_c(d_{\rm m})}{3\pi\mu d_{\rm m}} = qB. \tag{12}$$

where q = ne is the charge on the particle. The charging of fractal aggregates is influenced by the morphology of the aggregates, the means of charging (field or diffusion), and the properties of the charging ions. It is also closely related to certain methods of measuring effective surface area, discussed further in Section 4.4.

2.2.3. Effective density and shape factor

With the measurable quantities m_p and d_m , it is possible to define two useful measures of particle shape. The effective density is defined using the mass of the particle and the volume of the mobility-equivalent sphere:

$$\rho_{\rm eff} \equiv \frac{6m_{\rm p}}{\pi d^3} = \left(\frac{d_{\rm ve}}{d_{\rm m}}\right)^3 \rho_{\rm m}.\tag{13}$$

Another important descriptor of particle shape, the dynamic shape factor, χ , is defined as the ratio of drag force of a particle relative to an equivalent spherical particle having the same volume and velocity:

$$\chi = \frac{F_{\rm D}}{F_{\rm d,ve}} = \frac{d_{\rm m}/C_{\rm c}(d_{\rm m})}{d_{\rm ve}/C_{\rm c}(d_{\rm ve})}.$$
 (14)

The dynamic shape factor has a value of $\chi=1$ for spheres where $d_{\rm m}=d_{\rm ve}$. For other shapes, the dynamic shape factor incorporates knowledge of the aforementioned slip correction and is necessarily larger than unity. For *typical* soot, the dynamic shape factor will approach unity for very small particles (where the aggregates will be made up of a single primary particle) and will exceed two for particles larger than 100 nm.

Overall, effective density and shape factor are really alternative ways of comparing the mobility of a non-spherical particle with that of the volume-equivalent particle, and can thus be determined with the same set of measurements. Given the definition of the effective density, the dynamic shape factor can be equally phrased as

$$\chi = \left(\frac{\rho_{\rm m}}{\rho_{\rm eff}}\right)^{1/3} \frac{C_{\rm c}(d_{\rm ve})}{C_{\rm c}(d_{\rm m})}.\tag{15}$$

Thus, for large particles, where $C_c \to 1$, $\chi \to (\rho_m/\rho_{eff})^{1/3}$. As a rough approximation, for small particles, $C_c(d) \propto 1/d$ (Lee & Liu, 1980), such that $\chi \to (\rho_m/\rho_{eff})^{2/3}$. In the transition, the dynamic shape factor will take on a value between these two limits.

2.2.4. Aerodynamic diameter

The aerodynamic diameter, $d_{\rm ae}$, is defined as the diameter of a sphere with a density of $\rho_0 = 1000 \ {\rm kg/m^3}$ with the same settling velocity as the actual particle (Hinds, 1999). The relaxation time, τ , is the time required for particle's velocity to adjust to a new condition of forces and is defined as,

$$\tau = mB. \tag{16}$$

It can also be shown that

$$\tau = \frac{\rho_0 d_{\rm ae}^2 C_{\rm c}(d_{\rm ae})}{18\mu}.\tag{17}$$

As such, the aerodynamic diameter can be thought of as an relaxation-time equivalent diameter. Combining the above expressions, it is shown that the aerodynamic diameter is a function of gas properties in addition to the mass (density) of the particle:

$$d_{\rm ae} = \sqrt{\frac{6}{\pi \rho_0} \frac{m_{\rm p}}{d_{\rm m}} \frac{C_{\rm c}(d_{\rm m})}{C_{\rm c}(d_{\rm ae})}}$$
(18)

or, more compactly,

$$d_{\rm ae} = d_{\rm m} \sqrt{\frac{\rho_{\rm eff} C_{\rm c}(d_{\rm m})}{\rho_{\rm 0} C_{\rm c}(d_{\rm ae})}}.$$
 (19)

Further, from these expressions, it becomes clear that if one knows two of m_p , d_m , and d_{ae} , one can compute the third quantity. This is useful given that classifiers are available for all three of these quantities (see Section 4).

2.2.5. Relations between length scales for fractal aggregates

With a few more empirical results for fractal aggregates, all relevant length scales for a particular aggregate can be determined for typical soot of a given mobility. Firstly, particle mass and mobility diameter are directly measurable, and, as a convenience, the relationship is often expressed as an empirical power law, known as the *mass-mobility relation* (Park, Cao, Kittelson, & McMurry, 2003),

$$m_{\rm p} = k d_{\rm m}^{D_{\rm m}} = m_{100} \left(\frac{d_{\rm m}}{100 \,{\rm nm}}\right)^{D_{\rm m}},$$
 (20)

where k is a prefactor, m_{100} is the mass of a particle with $d_{\rm m}=100$ nm, and $D_{\rm m}$ is the mass-mobility exponent. From this one obtains the effective density directly:

$$\rho_{\rm eff} = \frac{6k}{\pi d_{\rm m}^{3-\rm D_m}} \tag{21}$$

At first glance, Eq. (20) resembles Eq. (1), and initially researchers assumed that $D_{\rm m}=D_{\rm f}$. In fact, $D_{\rm m}$ is typically much larger than $D_{\rm f}$ (Sorensen, 2011). Still, the mass-mobility relation has shown to be useful for many soot sources, with typical values of soot from non-premixed combustion provided by Olfert and Rogak (2019); for fresh soot, typical values of $D_{\rm m}$, k, and m_{100} are 2.48, 2.93×10^{-6} fg (assuming $d_{\rm m}$ is in nm), and 0.267 fg, respectively.

The mass-mobility relation is sufficient to constrain the relationship between many of the equivalent particle sizes. For example, one can determine the aerodynamic diameter as,

$$d_{\rm ae} = d_{\rm m}^{\frac{1}{2}(D_{\rm m}-1)} \sqrt{\frac{6kC_{\rm c}(d_{\rm m})}{\pi \rho_0 C_{\rm c}(d_{\rm ae})}}.$$
 (22)

Using the aforementioned relations, one can also compute the mass (Eq. (20)), volume-equivalent diameter, effective density (Eq. (21)), and dynamic shape factor (Eq. (14)). These are also the parameters that are readily accessible using online classifiers and detectors. With a few additional assumptions, one can also compute a range of others quantities. For instance, assume that the primary particles are larger in larger aggregates, based on the empirical Eq. (6), which is applicable to typical soot from non-premixed combustion. Further, assume that $d_A = d_m$ and that the projected area can be related to the number of primaries through Eq. (4) (Brasil et al., 1999). Given the above, it is finally possible to estimate the radius of gyration using Eq. (1). The results of these assumptions are summarized in Table 2. Caution should be used to not extrapolate these functions outside of the range that they were intended, where effective densities can exceed the material density (or $\chi < 1$, Eq. (15)). Certainly, the models linking the length scales in the table all have degrees of uncertainty, as indicated in the original body of literature (Table 1). For instance, Fig. 13, discussed later, provides some indication of the variability of *typical* soot. However, Table 2 provides very reasonable estimates for fresh soot that may be useful for designing experiments or making a first assessment of real experimental data.

2.2.6. Optical-equivalent diameters

The optical diameter may be defined as the diameter of a reference particle which scatters the same amount of light into a defined solid angle as the actual particle (ISO, 2020c; Moosmüller et al., 2009). In other words, optical diameters are defined by the calibration of light-scattering instruments with reference particles of known size, refractive index, and shape (Section 6.3.4). The reference particles used for calibration may be synthetic (for example, polystyrene latex spheres) or natural (for example, Arizona test dust). Fundamentally, this calibration approach is similar to the calibration of mobility or aerodynamic diameter using reference particles. However, it is relatively difficult to combine optical diameters with other diameters, as was done above for $d_{\rm m}$ and $d_{\rm ae}$. In addition to the influence of refractive index and shape on optical diameter, the angular dependence of scattering means that optical diameters are instrument-specific, and any comparison would require relatively detailed instrument modeling. Although possible, this approach is rare, since the refractive index and shape of the measured particles are rarely known. Optical sizing is further discussed in Section 6.

2.3. Describing populations of aggregates

Combustion aerosols are inevitably polydisperse, so complete characterization of the population requires that the (size or mass) distribution of various properties are measured. Within aerosol science, distributions are typically expressed in a differential form,

$$\frac{\partial Y}{\partial \ln d}$$
 (23)

where Y is some measure of the quantity of particles and d is some measure of a particle's physical size (typically a diameter, though a single-particle mass could be substituted). A common example is the number concentration-based mobility distribution, $\partial N/\partial \ln d_{\rm m}$, which can be measured using a scanning mobility particle sizer (SMPS). While number distributions are most common, other distributions (eg., area, mass, light scattering) are also present in the literature. Conversions between different types of distributions is more involved than simply converting between particle sizes in that it can involve an adjustment to both the numerator and denominator. The mathematics are described in several aerosol texts (e.g., Flagan & Seinfeld, 1988), though typically for particles of constant density.

Particle size distributions are often approximately lognormal (Hinds, 1999), such that the distribution is characterized using a geometric mean diameter (GMD, d_g), which corresponds to the first distribution moment in log-space, and geometric standard deviation (GSD, σ_a),

$$\frac{\partial Y}{\partial \ln d} = \frac{1}{\ln \sigma_g \sqrt{2\pi}} \exp\left[-\frac{1}{2} \left(\frac{\ln d - \ln d_g}{\ln \sigma_g}\right)^2\right]. \tag{24}$$

The GMD and GSD are specific to the chosen particle size and measure of the quantity of particles (Hinds, 1999). For example, when Y = N is the number (or count) of particles, the GMD is referred to as the count median diameter (CMD). Conversely, when Y = M is the mass of particles in a given bin, the GMD is referred to as the mass median diameter (MMD). Conversion between these two quantities is accomplished using the Hatch-Choate relation (Hatch & Choate, 1929; Heintzenberg, 1994; Hinds, 1999), which we can generalize for the mass-mobility relation (Sipkens, Corbin, Koukoulas, Oldershaw, Lavoie, Oliaee, Liu, Leroux, Smallwood, Lobo, & Green, 2022),

$$d_{\text{mmd}} = d_{\text{cmd}} \exp \left[D_{\text{m}} \left(\ln \sigma_{\text{g}} \right)^{2} \right]$$
 (25)

Changing the size in the denominator of Eq. (23) will also have an impact on the distribution. In general, if a size distribution is lognormal with respect to some size and that size can be related to another size via a power law, the transformed distribution will also be lognormal. For example, if the distribution with respect to mobility diameter is lognormal, assuming the mass-mobility relation will result in a lognormal distribution with respect to single-particle mass, though with different distribution moments. The new geometric standard deviation (GSD) will be given by

$$\sigma_{g,2} = \exp\left(D \ln \sigma_{g,1}\right) \tag{26}$$

where D is the exponent in the power law (e.g., when converting from mobility diameter to single-particle mass, $D = D_{\rm m}$) and $\sigma_{\rm g,1}$ and $\sigma_{\rm g,2}$ are the original and transformed GSDs, respectively. The new geometric mean diameter (GMD) is given by the standard conversion (via the relevant power law) of the original GMD.

Fig. 6 compares distributions of different types by combining these conversion approaches for typical fresh soot. The top panel shows how count and other measures of aerosol quantity are distributed with respect to mobility diameter. The mass-mobility relation provides a direct relationship between $d_{\rm m}$ with $d_{\rm ae}$ and $m_{\rm p}$, with these alternative size axes shown below the main x-axis. For combustion generated aggregates, $\rho_{\rm eff}$ decreases with aggregate mass, and as a result distributions expressed with respect to aerodynamic diameter are much narrower than if expressed as a function of mobility diameter (see, for example, Fig. 6). Thus, a distribution with a mobility diameter CMD of 145 nm and GSD = 1.82 corresponds to an aerodynamic diameter distribution with a count median aerodynamic diameter (CMAD) of 74.1 nm and GSD_{ae} of 1.56. Conversely, the distribution of single-particle mass is broader than the distribution of mobility diameter.

2.4. Outlook

To the extent that the fractal model holds for the particles, one generally needs to specify the fractal dimension, primary particle size, fractal prefactor, and number of primary particles to constrain the particle morphology. For typical aggregates (as produced by diffusion-limited aggregation), these fractal parameters have been linked to the characteristic sizes that are readily measured by aerosol instruments. However, the decades-old fractal model is evolving, particularly with respect to details at the level of primary particle overlap and size variations. With a better understanding of the fresh (DLCA-like) structure, deviations due to restructuring are more readily detected. Analysis of structure through microscopy, considered next, requires very few assumptions about particle morphology and thus is most useful when we are less confident in the fractal model.

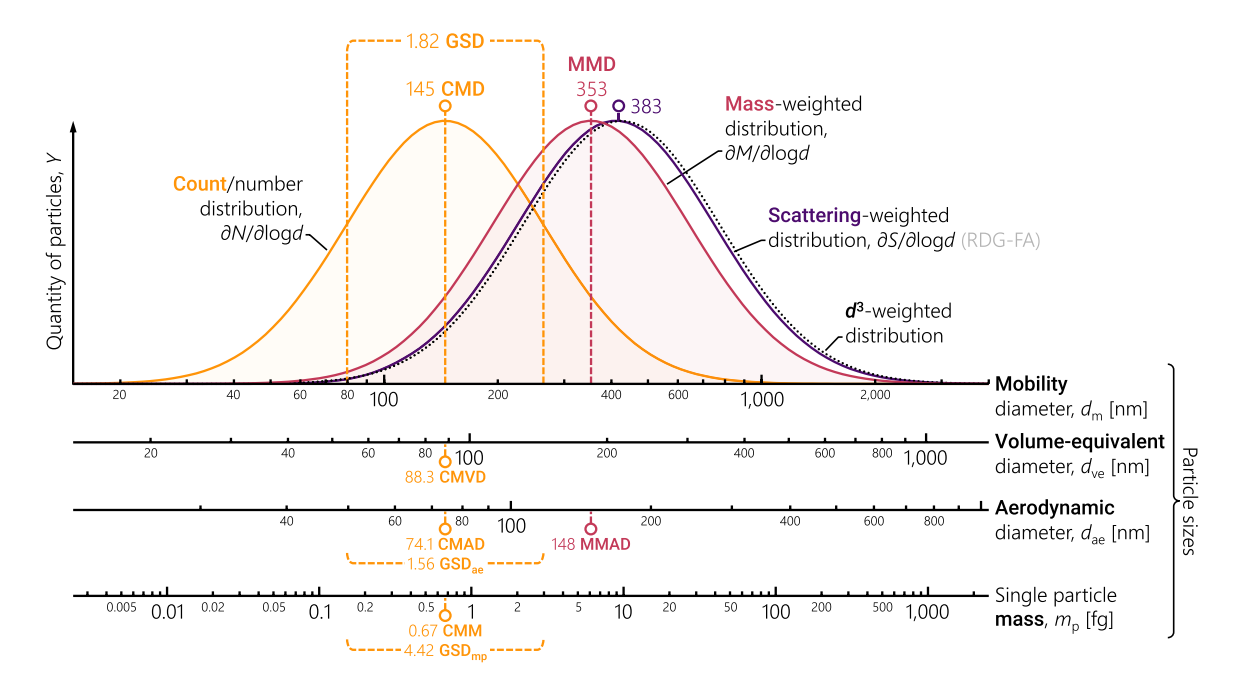


Fig. 6. Schematic demonstrating the equivalent size distributions for lognormally-distributed soot particles. Scattering-weighted distributions are estimated using RDG-FA theory. Case shown is for the universal mass-mobility relation (Olfert & Rogak, 2019), and $D_{\text{TEM}} = 0.35$. This small value of D_{TEM} results in the mass-and scattering-weighted distributions being similar. The dotted, black line corresponds to the cubed-weighted distribution (i.e., the mass-weighted distribution, if the particles were spheres). Abbreviations include count median diameter (CMD), taken by default as with mobility diameter; mass median diameter (MMD), similarly taken for mobility diameter; geometric standard deviation (GSD); count median volume-equivalent diameter (CMVD); count median aerodynamic diameter (CMAD); count median mass (CMM); and mass median aerodynamic diameter (MMAD).

3. Microscopy

Microscopy provides a wealth of information by direct imaging of particle characteristics. Studies are dominated by transmission electron microscopy (TEM), driven by the need to image at scales on the order of 2–1000 nm and the relatively widespread availability of TEM. Since being used to investigate the structure of carbon black in the 1940s (Hess, Ban, & McDonald, 1969; Hess & Herd, 2018; Ladd & Wiegand, 1945), TEM has become a mainstay in characterizing combustion generated particles. Research typically targets collecting representative samples, analyzing images with sufficient speed and accuracy to obtain quantitative information, and the use of advanced techniques to obtain three-dimensional information from images. Scanning TEM (STEM²) is similar to traditional TEM except in that a focused electron beam is scanned across the sample instead of a broad parallel beam and can equally be used in imaging.

A range of other microscopy tools can also be used, with a review of these techniques provided by Baldelli et al. (2020) and Li, Shao, et al. (2016). Briefly, scanning electron microscopy (SEM) is better-suited for the analysis of larger structures, such as deposits on filters (e.g., China, Mazzoleni, Gorkowski, Aiken, & Dubey, 2013; Chu et al., 2019; Liati & Dimopoulos Eggenschwiler, 2010). While the size resolution is helped by using field emission electron sources, imaging of soot particles with SEM remains limited. Helium ion microscopy (HIM; Schenk et al., 2013), which replaces the incident electron beam with helium ions, provides very similar images at slightly better resolution than SEM. To the best of the author's knowledge, HIM has been used to image nascent soot but not yet full aggregates. Atomic force microscopy (AFM) has been applied to image whole aggregates (e.g., Kholghy, Saffaripour, Yip, & Thomson, 2013; Liu, Song, et al., 2018), though typically with similar size resolution limitations as the other techniques noted here alongside limitations in terms of only imaging an envelope around the soot aggregate. Common to these three techniques is that images give a sense of the 3D structure of the particles, which still holds some utility. A comparison of the types of images produced by these different techniques for soot is shown in Fig. 7.

Many of these instruments also provide complementary analytical capabilities to resolve chemical information and structural information about latices, such as via high resolution TEM (HRTEM), e.g., Müller, Su, Wild, and Schlögl (2007), Vander Wal and Choi (1999), Vander Wal, Tomasek, Pamphlet, Taylor, and Thompson (2004), Vander Wal, Yezerets, Currier, Kim, and Wang (2007), and Wentzel, Gorzawski, Naumann, Saathoff, and Weinbruch (2003). Although methods that provide information on the sub-primary particle and subnanometer scale are becoming more powerful and widespread, these techniques are out of the scope of this review. For more information we refer to related reviews, e.g., discussing soot aging (Baldelli et al., 2020; Michelsen, 2017).

² Not to be confused with scanning tunneling electron microscopy, which has the same acronym and can be used in a similar way.

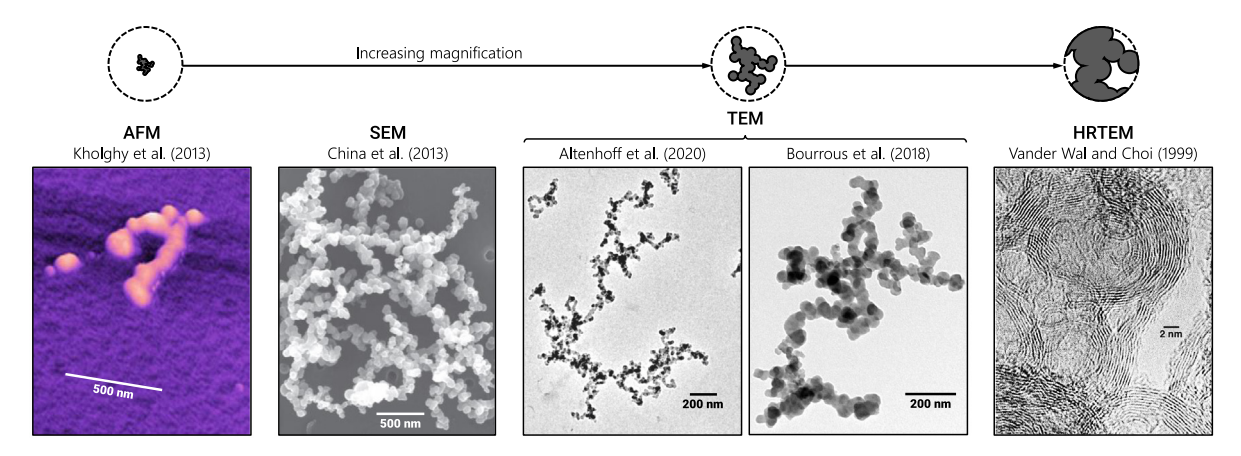


Fig. 7. A series of microscopy images of soot (Altenhoff, Aßmann, Teige, Huber, & Will, 2020; Bourrous et al., 2018; China et al., 2013; Kholghy et al., 2013; Vander Wal & Choi, 1999). Note the changing scales from left to right. AFM and SEM allow for some sense of the 3D structure of the aggregates. Note that AFM is limited to an envelope surrounding the particle with little information on gaps and details.

3.1. Sample collection

Electrostatic forces are most commonly used to collect particles on the substrate used for microscopy (typically a 3 mm diameter grid). Electrostatic samplers either sample from a previously charged aerosol (e.g., downstream of a DMA or CPMA) or use a built-in charger. Stand-alone electrostatic samplers typically use corona around a thin wire to charge particles, which then migrate to the collection substrate which is held at 3–7 kV relative to the ion source. Reported collection efficiencies vary from under 10% (Fierz, Kaegi, & Burtscher, 2007) to 80%–90% (Cardello, Volckens, Tolocka, Wiener, & Buckley, 2002; Miller, Frey, King, & Sunderman, 2010). The corona chargers generate ozone (Cardello et al., 2002), which raises the possibility of affecting organic materials that might be attached to soot. Higher sampling efficiencies appear to result from placing the charger very near the collection plate, and sampling efficiencies are generally lower for particles in the 100–200 nm diameter range. Samplers that collect previously-charged aerosols (e.g., TSI Model 3089) are simpler but use the same collection principles (Dixkens & Fissan, 1999).

Thermophoresis (migration of a particle down a temperature gradient) can also be used to collect particles for microscopy. Normally, thermophoretic velocity is a weak function of particle size, increasing by 25% from the smallest to the largest soot particles in typical samples (Ait Ali Yahia, Gehin, & Sagot, 2017). This facilitates representative sampling. For very high pressure flame sampling, there may be a larger bias towards larger particles (Rosner & Tandon, 2017). Thermophoretic sampling is especially attractive for in situ sampling from hot environments (e.g., flames, engine exhaust), as, in that case, the sampler is simply a mechanism for rapid insertion and removal from the test gas. This was the method used in some the earliest studies of soot morphology (Dobbins & Megaridis, 1987). Botero, Akroyd, Chen, Kraft, and Agudelo (2021) show that for in-flame sampling, exposure time affects both the artifacts of condensation and grid overloading, at which point individual aggregates cannot be distinguished. Thermophoretic sampling of room-temperature aerosols is possible using a heater to create a temperature gradient near a cooled collection substrate. Kasper (1982) reviewed and improved the earliest heated wire precipitator (Green & Watson, 1935). High collection efficiency and uniform deposits can be obtained with careful thermal design and very low sample flows (Gonzalez et al., 2005). Sampling efficiency is much lower at larger flows (above 100 cm³/min), which is a potential problem in collecting samples from ambient air but not in combustion source characterization where particle concentrations are typically > 10⁷ counts/cm³. With too many aggregates collected on a grid, there is a substantial chance that two aggregates will overlap and thus appear to be one larger aggregate, biasing the measured size distribution.

Particles can be collected by filtration using TEM grids with holey films that allow the passage of air. Such samplers are compact and simple, but the collection efficiency is a relatively strong function of size, and minimum for particles in the 50–100 nm size range (R'mili, Bihan, Dutouquet, Aguerre-Charriol, & Frejafon, 2013).

Impaction is rarely used for collecting soot samples because it is a strong function of size and soot has small aerodynamic diameters. However, the high velocities and low pressure in an electrostatic low pressure impactor (ELPI) can make this possible (e.g., Baldelli & Rogak, 2019). Given that the collection of very small particles by impaction requires very high velocities, fragmentation is possible for soot aggregates grown by post-flame coagulation (Rothenbacher, Messerer, & Kasper, 2008). Furthermore, deposits near the impaction zone are typically thick, so that it is often difficult to distinguish individual aggregates.

There have been a few studies of artifacts of sample storage. In a study of soot from the McKenna burner (a premixed flame) (Ouf, Yon, Ausset, Coppalle, & Maillé, 2010), it was reported that particle overlap coefficient and primary particle size changed slightly. The changes were attributed to loss of organic materials from the soot matrix over time. Liquids condensed on the surface of soot aerosols can cause collapse of the low-density fractal structure (Chen, Enekwizu et al., 2018; Colbeck, Appleby, Hardman, & Harrison, 1990; Corbin et al., 2023). It seems likely that condensation on a collection substrate could affect particle morphology, but recent work by Chen, Zakharov, and Khalizov (2023) suggests that adhesion of the aggregate to the substrate can stabilize the morphology against collapse. Botero et al. (2021) show that there are artifacts from imaging (beam damage) but these affect nanostructure more than the morphology.

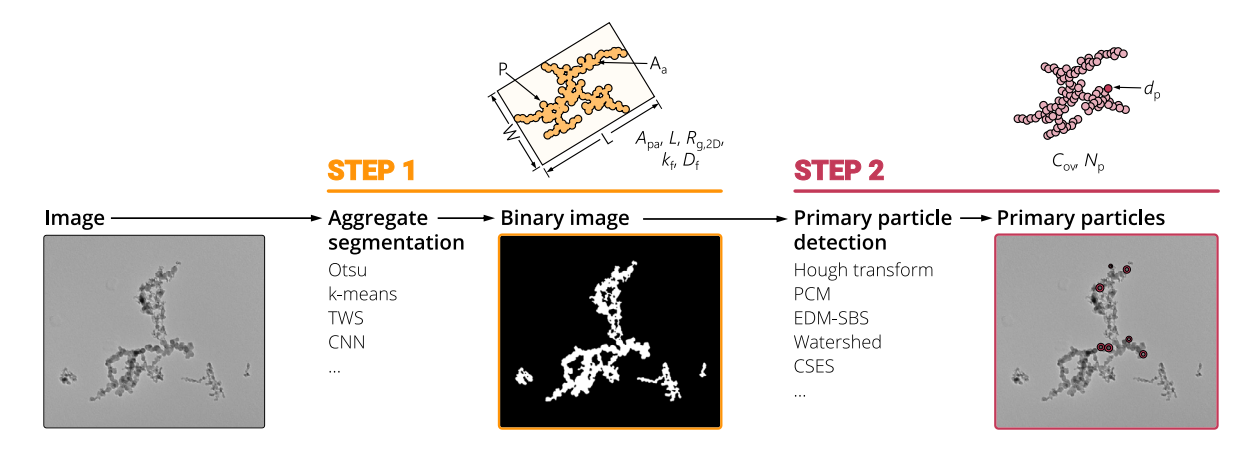


Fig. 8. Typical analysis routine for getting particle characteristics of soot from TEM images. While the primary particle detection step is not always dependent on the aggregate segmentation stag (e.g., when using the Hough transform), the segmentation output can often be used to filter primary particles and associate them with specific aggregates. Other techniques explicitly use the binary image in the primary particle detection step.

Source: Upper graphics are adapted from Brasil et al. (1999).

Table 3
Studies with a focus on TEM image analysis routines, alongside the corresponding methods used for aggregate-level segmentation or binarization and primary particle detection. Method acronyms include: Euclidean distance mapping (EDM); center-selected edge scoring (CSES); surface-based scale analysis (SBS); trainable Weka segmentation (TWS); pair correlation method (PCM); and convolution neural network (CNN).

Study	Year	Aggregate level	Primary particle level
Tian et al.	2006	Not stated	Relative optical depth
Sachdeva and Attri	2008	Not stated ^a	Not specified (GUI)
Coudray, Dieterlen, Roth, and Trouvé	2009	Active contour	N/A
Aizawa et al.	2012	Not specified (GUI)	GUI (cross method)
Grishin, Thomson, Migliorini, and Sloan	2012	Otsu	Hough transform on outline
De Temmerman, Verleysen, Lammertyn, and Mast	2014	iTEM binarise filter	EDM-Watershed
Bescond et al.	2014	Isodata ^b	EDM-SBS
Kook et al.	2016	_	Hough transform
Dastanpour, Boone, and Rogak	2016	Otsu	PCM
Wang et al.	2016	Not specified ^c	Hough transform
Anderson, Guo, and Sunderland	2017	_	CSES, Hough transform, EDM-SBS
Bourrous et al.	2018	Otsu	Hough transform, EDM-SBS
Verma et al.	2019	Not specified ^d	Hough transform
Altenhoff et al.	2020	TWS (ImageJ)	Hough transform
Sipkens and Rogak	2021	k-means	PCM
Sipkens, Frei et al.	2021	CNN	EDM-SBS, PCM, Hough transform
Cabarcos, Paz, Pérez-Orozco, and Vence	2022	Otsu	Hough transform
Paz, Cabarcos, Vence, and Gil	2022	Active contour	_

^aThe authors used the now deprecated UTHSCSA image tool.

3.2. Image analysis

Image analysis is often the rate-limiting step in characterizing particles. Semi-automatic approaches, which still involve some level of user intervention but have a subset of the steps performed in an automated way, have rapidly expanded over the past two decades, spurred on by increases in computing power. Despite this, the transition to fully automated approaches has been challenging, given the impact of relatively small segmentation errors on population-level statistics. For example, aggregates can easily be broken into pieces during image processing (Sipkens, Frei et al., 2021), resulting in a perception of much smaller aggregates than actually exist on the grid.

Image analysis can be broken into two steps (Brasil et al., 1999), identified in Fig. 8: (1) aggregate detection, that is, *segmenting* the image into the aggregates and the background, and (2) primary particle detection. Often these two steps are interdependent, with the primary particle detection first requiring a segmentation. Studies and their corresponding methods are listed in Table 3. In both cases, analysis is more challenging than on engineered nanoparticles, as the carbonaceous particles have relatively low contrast against the carbon films present on typical collection grids. As such, methods developed for other particles (e.g., in conjunction with ImageJ software, Schneider, Rasband, & Eliceiri, 2012), may fail for soot.

^bImplied by the use of ImageJ, though other thresholding techniques were available.

^cGiven the use of standard MATLAB functions, binarization may be by imbinarize, which applies Otsu thresholding.

^dFigures suggest the use of active contour via a MATLAB app.

3.2.1. Aggregate detection

Despite being the first step performed by most processing routines, details of the segmentation step are not always explicitly provided in studies (Aizawa et al., 2012; Tian et al., 2006; Verma et al., 2019; Wang et al., 2016), replaced with more general statements about thresholding or binarization. Coudray et al. (2009) used an active contour method (also known as "snakes") to segment aggregates (El Omary, 1994) in SEM images. This approach still required substantial user intervention, in the form of a loose initial contour around the aggregate that acts as an starting point for energy minimization. Many more automated aggregate detection techniques employ Otsu's method (Otsu, 1979) to separate background pixels from the aggregates (Bourrous et al., 2018; Cabarcos et al., 2022; Dastanpour et al., 2016; Grishin et al., 2012; Park, Huang, Ji, & Ding, 2012). Otsu thresholding is also similar to isodata thresholding, the default used in ImageJ (Schneider et al., 2012) and Fiji (a specialized version of ImageJ), the use of which is implied in multiple studies (Bescond et al., 2014; Rice et al., 2013). The use of Otsu segmentation typically requires some degree of pre- or post-processing to achieve a meaningful segmentation (except for the most ideal of images, e.g., Bourrous et al., 2018), heavily featuring morphological operations. Most notably, multiple studies employ morphological closing or opening to connect nearby aggregate segments (Bourrous et al., 2018; Dastanpour et al., 2016; Wang et al., 2016), which may not be connected following the segmentation step.

Otsu's method, without post-processing, typically results in rather messy segmentation. This has motivated the use of more advanced techniques, including *k*-means segmentation (Sipkens & Rogak, 2021), which can be understood as a generalization of Otsu's method to consider more than just the gray-scale pixel values; trainable WEKA segmentation (Altenhoff et al., 2020) via ImageJ (Arganda-Carreras et al., 2017; Schneider et al., 2012); segmentation using a convolutional neural network (CNN) (Sipkens, Frei et al., 2021), which typically require images of specific aspect ratios; and active contour-based methods (Paz, Cabarcos, Vence et al., 2022). Results are relatively consistent across these newer methods, all showing improvements over Otsu thresholding. Haffner-Staton, Avanzini, La Rocca, Pfau, and Cairns (2022) coupled segmentation in ImageJ with a CNN method to automatically classify soot and non-soot particles, as a route to automate analysis of mixed particle samples.

Following segmentation, images can be used to derive particle characteristics. The earliest studies, still using manual analysis, determined aspects ratios (Cohan & Watson, 1951; Hess & Herd, 2018). Since, studies have computed a range of characteristics, including projected area-equivalent diameters (Jung, Kittelson, & Zachariah, 2004; Köylü et al., 1995; Lee et al., 2002), perimeter, fractal parameters (Wozniak, Onofri, Barbosa, Yon, & Mroczka, 2012), and circularity (Coudray et al., 2009). Often following segmentation, analysis is on a binary image, though it is also possible to work with the grayscale information within the particle boundary, retaining some depth information (Cai, Lu, & Sorensen, 1993; Tian et al., 2006).

3.2.2. Primary particle detection

Primary particle sizing methods, also summarized in Table 3, show more variety. Manual analyses remain the most reliable method for primary particle sizing, even if the labor-intensive nature of the technique forbids a large number of aggregates. Often analyses are aided by the help of GUIs, such as ImageJ/Fiji (Schneider et al., 2012) or a range of custom software, and rely either on drawing circles on the image or using a *cross* method with two lines drawn across the primary particle (Aizawa et al., 2012; Dastanpour et al., 2016). It is worth noting that defining individual primary particles can be challenging, even when performing a manual analysis, as many aggregates do not have well-defined spherules. Instead, aggregates have primary particles that have merged and overlap one another. As such, while image analysis remains a valuable tool for investigating the structure of the particles, results must be considered within this context.

The most common automatic primary particle detection methods are based on the Hough transform (Altenhoff et al., 2020; Cabarcos et al., 2022; Grishin et al., 2012; Kook et al., 2016; Sipkens, Frei et al., 2021; Verma et al., 2019; Wang et al., 2016), which uses a mathematical transform to detect circular objects in the image. An important feature of many of these methods is that they do not require a binary mask prior to analysis, though the mask can be used to filter circles identified in the background. Hough-based methods also identify individual primary particles, which can be used to identify spatial structure in the primary particle characteristics in addition to primary particle overlap, features that make the Hough transform favorable relative to some of the ensemble methods described subsequently. Still, methods using the Hough transform seem to have a high degree of variability, with the lower contrast and complexity of features internal to the aggregates resulting in a splintering into different adaptations of the Hough transform across the literature. These adaptations are often laboratory-specific and may fail outside of a specific context. Applications are typically accompanied by a large number of pre- and post-processing steps, akin to the aggregate detection step. Several studies build up to using a Canny edge detection (CED) (Cabarcos et al., 2022; Kook et al., 2016; Mirzaei & Rafsanjani, 2017; Wang et al., 2016), yielding a binary mask on which the Hough transform is applied. Bourrous et al. (2018) used the binary from the aggregate detection step, limiting primary particle size detection to the outer boundaries of the aggregate. Nevertheless, visually, this seems to produce a reliable gauge of the primary particle size, distribution, and, perhaps, even the degree of overlap. Grishin et al. (2012) supplemented their aggregate-level segmentation with Papert's turtle approach, which was used to form an outline of the aggregate on which the Hough transform was applied. With all these variants of the Hough transform, typically only a fraction of the primary particles in an aggregate are detected.

Another class of methods uses the binary mask of the image directly, commonly computing the Euclidean distance map (EDM), mapping the distance to the closest edge pixel, prior to further analysis steps. Bescond et al. (2014) developed EDM-surface-based scale analysis (EDM-SBS), which involves slowly eroding the particle and determining the rate at which the particle area is diminished. This curve can be scaled to an empirical curve derived by the authors to determine primary particle information. De Temmerman et al. (2014) paired EDM with a watershed method that attempts to define basins in the segmented binary. The particles in that instance were more compacted than usual. For many aggregates, the watershed method is biased towards much larger

sizes (Sipkens, Frei et al., 2021). Dastanpour et al. (2016) developed the pair correlation method (PCM), which uses the binary mask and a single point on the pair correlation function to derive primary particle sizes. These techniques are generally ensemble based, giving an average primary particle size for a single aggregate or for a set of aggregates in a single image and rely on some kind of calibration of sigmoidal shaped curves.

Tian et al. (2006) developed a method that uses the gray-scale values in an attempt to identify regions of overlapping particles. Given that classified particles were not shown in that work, it is difficult to assess the quality of the method relative to other techniques. Anderson et al. (2017) used a center-selected edge scoring (CSES) method, which uses an estimate of a primary particle's center, requiring a fair degree of user intervention. Resonances between morphological operations and the particles sizes leave room for further routes to analysis in similar vanes to these methods. Neural networks, while applied at the aggregate-level stage (Sipkens, Frei et al., 2021) and on engineered nanoparticles (Frei & Kruis, 2018, 2020), have not yet been applied to this application. This is likely due, at least in part, to the lack of a robust data set to train the networks combined with higher noise and low contrast of soot aggregates.

Uncertainties in retrieved particle sizes stem from various sources, including user-to-user differences (Kondo, Aizawa, Kook, & Pickett, 2013; Rice et al., 2013), and depend on the chosen technique (Anderson et al., 2017; Sipkens, Frei et al., 2021). However, there is a limited understanding of the extent of these uncertainties given that studies considering more than one technique or laboratory are rare, in particular within the context of combustion particles. Interlaboratory studies (such as Grulke et al., 2018) are required to investigate this phenomenon for modern analysis techniques. Primary particle sizing techniques can also have complicated relationships to the aggregate segmentation steps, which require further study. For example, Sipkens, Frei et al. (2021), employed EDM-SBS (Bescond et al., 2014), PCM (Dastanpour et al., 2016), a watershed method (De Temmerman et al., 2014), and the variant of the Hough method of Kook et al. (2016). The authors showed sensitivities to the chosen aggregate-level segmentation method. Furthermore, because there is inherent variability in particle size, averages have an uncertainty governed by the usual rules of statistics, decreasing with diminishing returns as the number of samples increases. For example, if the geometric standard deviation of the primary particle size is a GSD of $\sigma_{\rm g}=1.4$, 100 measurements would result a standard deviation of the mean of 3%. Usually, the GSD within an aggregate is less than this, and a sample of 20–50 measurements results in an uncertainty smaller than the imaging and image processing errors.

3.3. Extracting fractal information

Fractal models and methods of extracting fractal dimensions arise in many branches of science and mathematics (Grassberger & Procaccia, 1983; Mandelbrot, 1977). Early work on the extraction of fractal dimension from soot micrographs include Cai et al. (1993), Köylü et al. (1995), and Oh and Sorensen (1997), with some more recent discussion by Lapuerta, Ballesteros, and Martos (2006) and Wozniak et al. (2012). There are two distinct approaches to determining $D_{\rm f}$. In both cases, it is worth noting that correlation between $k_{\rm f}$ and $D_{\rm f}$ is typically very high, that is, if one of the two values is incorrect, the other is also likely to be incorrect.

First, it is possible to determine the structure within individual aggregates using "gauges" (nested circles or squares) of different sizes and examining the scale of perimeter length with decreasing gauge length (Forrest & Witten, 1979). An early comparison of those approaches is described in Cai et al. (1993). Such approaches are appealing in that they provide an estimate of fractal dimension for each aggregate, which is useful in classifying particles in an inhomogeneous population (Pang et al., 2022). However, from earlier studies of simulated aggregates, these approaches have been shown to perform inconsistently as estimators of the true 3D fractal dimension (Chakrabarty et al., 2011a). Another method of analyzing individual images (Lapuerta et al., 2006) starts with a model for the fractal prefactor, then chooses $D_{\rm f}$ to reconcile the number of primaries estimated from Eq. (1) with the number estimated from the projected area. Fundamentally, individual aggregates vary substantially in shape, and one needs to analyze a great many images to infer anything about the populations from which they come.

Second, one can extract the fractal dimension by examining the scaling of size and mass (or area, in images) according to Eq. (1), e.g., Samson, Mulholland, and Gentry (1987). This ensemble method (EM) is currently the most commonly used recipe for inferring $D_{\rm f}$ from 2D images. For each aggregate, one determines the primary particle size, projected area, and 2D radius of gyration. The latter can be determined from pixel coordinates.

$$R_{\rm g} = \sqrt{\sum_{i=1}^{N} \frac{(\mathbf{r_i} - \mathbf{r}_{\rm mean})^2}{N}}$$
 (27)

where \mathbf{r}_{mean} is the mean position of the pixels. The 3D radius of gyration is 10%–25% larger than the estimate from the projection, and mainly a function of the fractal dimension (Chakrabarty et al., 2011b; Köylü et al., 1995; Sorensen & Feke, 1996). Because this correction is essentially independent of aggregate size, it will not affect the fractal dimension obtained from the ensemble analysis, but it will affect the inferred fractal prefactor. The number of monomers is the ratio of the pixelated area and the area of a primary particle. As aggregate size increases, however, an increasing number of primary particles are obscured by other primary particles, so N_p is inevitably underestimated unless a correction factor is applied, such as Eq. (4), which is a refinement of the approach used by Samson et al. (1987). The final step is to fit N_p to $2R_g/d_p$ according to Eq. (1), normally in log-space with simple linear least-squares, to determine D_f and k_f . The degree of shielding is itself a function of the fractal dimension (e.g., Meakin et al., 1989), such that, after D_f is determined, it is essential to check that the shielding corrections are reasonable.

Although the general approach of the ensemble method is straightforward and has been used many times, there does not appear to be consensus on the appropriate average for d_p , how to make shielding corrections for N_p or 2D/3D corrections to R_g , and

how to weight points in the regression. Further, the extracted fractal dimension will be affected by systematic trends in primary particle size with aggregate size, i.e., Eq. (6)). Kheirkhah (2020) found that ignoring these trends resulted in a 5% increase in fractal dimension measured for engine soot. An interim standard approach is proposed here. We suggest that the primary particle size used in the denominator of Eq. (1) be the area-average diameter for each aggregate analyzed. Whether or not the average is computed from the first, second, or third moment of the primary particle diameter distribution is probably not critical here, given that the variation of primary particle size within aggregates is small. Inconsistencies in the approach would lead to variations in the fractal prefactor (which should be left free in the fitting but checked against the expected range of $k_{\rm f} \sim 1.1-1.7$). Consistent with most previous studies, we suggest that $N_{\rm p}$ be corrected by shielding (using a power law correction developed for soot similar to that being studied) and that $R_{\rm g}$ be used without projection corrections.

Recently Paz, Cabarcos, Conde, and Gil (2022) experimentally compared various methods of extracting fractal dimensions from images, including the commonly used approach from Köylü et al. (1995) and the iterative approach of Lapuerta et al. (2006). While this study found these two methods to agree closely, another study (Kholghy et al., 2017) found that the iterative method produced much larger fractal dimensions.

3.4. Outlook

Microscopy remains the only method of obtaining detailed information on particle size and morphology of individual particles. TEM imaging requires that particles must be sampled on to a substrate and are typically analyzed under a vacuum, often restricting analysis to refractory particles (such as, fortunately, mature soot). Some studies have now employed environmental TEM to image more volatile particles or to investigate particle transformations when subjected to the electron beam. This is an area that is likely to grow in the coming years. The separation of the particle sampling from the analysis introduces possibilities of artifacts, but it also allows collection by a wide variety of methods, ranging from flames to small personal samplers.

TEM images of soot and other combustion particles are also typically of low contrast relative to other particle types, likely evading standardization (ISO, 2020b). Identifying features within aggregates (such as primary particle size) is also challenging. Image analysis still largely relies on humans performing manual feature recognition and sizing, which has severely restricted the number of images that can be analyzed and adds subjectivity to the results. While human intervention remains important, automated analysis is getting better (especially for aggregate and average primary particle sizing). Despite this, analysis routines are often developed for images at a specific laboratory and type of image. Subjectivity in what constitutes a primary particle size hampers both the comparison of manually-derived data across laboratories or even individual users and what a given automated technique considers a primary particle, which is often biased by prior manual analyses. At the same time, interlaboratory studies (Grulke et al., 2018) or works comparing multiple of the approaches to automated analysis (Anderson et al., 2017; Sipkens, Frei et al., 2021) are uncommon. As such, it remains challenging to quantifying the uncertainties associated with TEM imaging. Nevertheless, the field is rapidly advancing, and we may expect in the coming few years that a student might use published codes to analyze thousands of images mechanically after performing spot checks on 10–20 images.

TEM images are also inherently projections of 3D structures, and, while work is ongoing to directly characterize these 3D structures, in most cases researchers must think about the range of possible configurations that could yield a given projection. Aggregates simulated for a variety of idealized growth mechanisms have been useful in elucidating the relations between 3D structures and their projections, but it is unclear how accurately these relations may be applied to real soot and real, noisy TEM images. The use of tilt stage TEMs to produce 3D models of soot aggregates by way of tomography is becoming increasingly common (Adachi, Chung, Friedrich, & Buseck, 2007; Baldelli, Trivanovic, & Rogak, 2019; Haffner-Staton, La Rocca, Cairns, & Fay, 2019; Orhan, Haffner-Staton, La Rocca, & Fay, 2016; Zhang et al., 2020) as a way to avoid these uncertainties and identify inherently 3D features such as rings or full light scattering properties.

Manual analysis is still essential for mixed populations of particles (e.g., when soot has metals or salts attached or when two aggregates have clearly been joined) and when spatial information about the primary particles may be useful. Machine learning may eventually automate analysis of these complex cases (e.g., Haffner-Staton et al., 2022), but before this is done, large training databases will be needed. The training sets could be built up through manual analysis by many researchers or possibly by synthetic images of simulated aggregates (e.g., as in Frei & Kruis, 2018). In either case, analyses could benefit from continued collaboration between laboratories.

4. Standalone aerosol classifiers and detectors

Combustion-generated aggregates emitted from sources are typically polydisperse. As such, there is a desire to quantify the population of the aggregates using distributions as a function of different physical properties. Common distribution measurements are count and mass distribution measurements as a function of mobility diameter, aerodynamic diameter, and single-particle mass (as shown in Fig. 6). The instruments described below can typically be used to measure particle distributions quickly (in real-time or in a few minutes) and can complement microscopy.

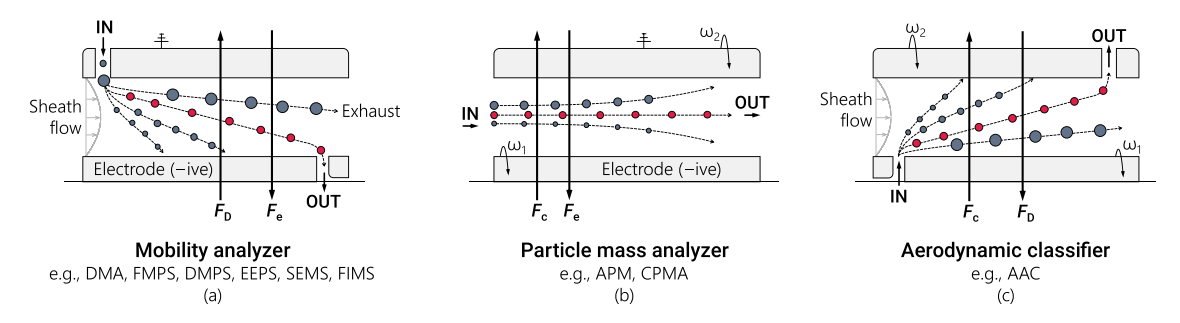


Fig. 9. Schematic demonstrating the operating principles of three common classes of classifiers. Bold arrows indicate the forces on the particles, including drag forces, F_D ; electrostatic forces, F_e ; and centrifugal forces, F_c .

Source: Adapted from a similar figure by Yao, Asa-Awuku, Zangmeister, and Radney (2020), who separated out the APM and CPMA configurations.

4.1. Mobility distributions

The most commonly reported distributions are count mobility-equivalent size distributions: $\partial N/\partial \ln d_{\rm m}$. This is partially due to the fact that mobility instruments can measure in the size range on the order of 1 nm to 1 μ m, which covers the range of most combustion-generated aggregates. Historically, diffusion batteries (Knutson, 1999) have provided measurements of particle mobility. Although these principles may find uses in new low cost instruments (e.g., Fierz, Weimer, & Burtscher, 2009) for nanoparticles (including soot), the size resolution of a diffusion battery is inherently very poor compared to the instruments considered in detail in this review and involve complex designs composed of screens, foams, or channels through which the particles diffuse. Rather, the mobility-equivalent size distribution is almost exclusively measured with the combination of a particle charger, differential mobility analyzer (DMA, Hewitt, 1957; Knutson & Whitby, 1975) and condensation particle counter (CPC, Agarwal & Sem, 1980). The combined system is often called a scanning mobility particle spectrometer (SMPS), though manufacturer-specific variants of the instrument can have other names, e.g., scanning electrical mobility sizer (SEMS) or differential mobility particle sizer (DMPS). The system relies on classifying charged particles by electrical mobility ($Z_p = qB$ where q is the particle charge, Eq. (12)) in the DMA and counting the number of particles with the CPC. The particles are typically charged with a bipolar charger, using radioactive or X-ray ion sources, which brings the particles to a stationary charge state (Wiedensohler, 1988). Although it is routinely assumed that aggregates reach the same charge distribution as their mobility-equivalent spheres, it is known that aggregates become more charged than spheres resulting in lower uncharged and single-charge fractions and higher multiple-charged fractions (Johnson et al., 2020; Rogak & Flagan, 1992; Xiao, Swanson, Pui, & Kittelson, 2012).

The DMA classifies particles by electrical mobility using electrostatic forces. Most DMAs consist of concentric cylinders where an electrically charged aerosol enters near the surface of the outer cylinder and is carried axially through the gap in the cylinders with particle-free sheath air as shown in Fig. 9a. The charged particles of one polarity are forced towards the inner cylinder by the electrostatic force. Near the end of the inner cylinder, there is slot where a fraction of the flow is extracted along with particles of a narrow range of electrical mobility (the *classified particles*). Particles with a higher electrical mobility impact on the inner cylinder before the exit slot, and particles of lower mobility, or particles of the opposite polarity, or uncharged particles either impact the outer cylinder or exit with the remaining flow. Although the majority of DMA classifiers are concentric cylinders, radial designs are also used (Zhang, Akutsu, Russell, Flagan, & Seinfeld, 1995).

Particles classified by the DMA at a given electrical mobility are typically counted with a CPC. The particles in the CPC are exposed to a supersaturated vapor (typically butanol or water) so that the vapor condenses on the particles and grows them to a sufficiently large size that they can be detected optically. Depending on the design of the CPC and the degree of supersaturation, particles as small as a few nanometers can be detected (Hering et al., 2017; Stolzenburg & McMurry, 1991).

The mobility size distribution is measured by scanning the voltage of the DMA through a wide range of voltages and continuously measuring the concentration of particles exiting the DMA with the CPC (Wang & Flagan, 1990). The particles exiting the DMA have a narrow (but finite) range of electrical mobilities. However, since the particles have a distribution of charge states, the particles exiting the DMA are a mix of different mobilities. Thus, data inversion is used to reconstruct the size distribution knowing the charge distribution of the charger (e.g., Wiedensohler, 1988), the transfer function of the DMA (e.g., Knutson & Whitby, 1975), and the detection efficiency of the CPC (eg. Mertes, Schröder, & Wiedensohler, 1995). The uncertainty in the charge distribution of aggregates is a major source of uncertainty in this method. Data inversion techniques are discussed more in Section 4.5.2.

The SMPS has high resolution, good accuracy, and reproducibility (Duelge, Mulholland, Zachariah, & Hackley, 2022; Wiedensohler et al., 2018) but poor time response. It generally takes between 15 s to 2 min to measure one size distribution (with the lower end producing less accurate results), and the data inversion assumes the incoming size distribution does not change during the measurement duration. Much faster mobility spectrometers have been developed using unipolar chargers and classifier columns, which incorporate rings of electrometers to measure the current produced by the charged particles collected on the electrometers (Reavell, Hands, & Collings, 2002). Examples of variants of this system make use of an array of detectors (typically electrometers) along the classifier column include the engine exhaust particle sizer (EEPS), differential mobility spectrometer (DMS), and fast mobility particle sizer (FMPS). The time response of these instruments can be less than a second, as the method does

not require scanning of the DMA voltage, but: (1) require a sufficiently large concentration of aerosol to make reliable current measurements, (2) have a lower size resolution, and (3) acquire data that is more difficult to invert. Another real-time mobility spectrometer is the fast integrated mobility spectrometer (FIMS), which uses a bipolar charger and an integrated classifier and condensation detector system, where mobility-classified particles are immediately grown via condensation at the end of the classifier and their position is measured with a camera (Kulkarni & Wang, 2006). The FIMS can detect low concentrations, has a fast time response (Olfert & Wang, 2009), and an accurate inversion (Olfert, Kulkarni, & Wang, 2008).

Emissions from combustion sources tend to follow lognormal mobility size distributions. The distribution may be a bimodal lognormal distribution with a nucleation mode and accumulation mode, where the accumulation mode contains the aggregates, which is the focus of this work (Kittelson, 1998). The count median diameter (CMD) of particles emitted from diesel and directinjection spark-ignition engines tends to fall in the range of 50–110 nm with geometric standard deviations (GSD) of 1.6–2.0 (Harris & Maricq, 2001). Aircraft aggregates tend to have CMDs of 15–50 nm and GSDs of 1.5–1.8 (see Saffaripour et al. (2020) for a review of the literature). Other burners and soot generators have been designed to give a wide range in CMD: from turbulent flame sprays to get CMDs down to 13 nm to inverse diffusion flames to get CMDs up to 270 nm and GSD ranging from 1.5–2.5 (Kazemimanesh et al., 2019; Moallemi et al., 2019; Stipe et al., 2005). In some instances inverse diffusion flames have been able to create super-aggregates with mobility diameters on the order of several microns (Chakrabarty, Moosmüller, Garro, & Stipe, 2012).

Aggregates in electrical-mobility classifiers are known to align with the electrostatic field (Li, Mulholland, & Zachariah, 2016; Zelenyuk & Imre, 2007). The alignment of the aggregate with the field results in a measured mobility diameter smaller than the orientation-averaged mobility diameter. This is mostly a problem for large aggregates which require high field strengths for classification. Li, Mulholland, and Zachariah (2016) observe a 5% decrease in mobility diameter for soot with a nominal mobility diameter of 200 nm over a range of field strengths). For small aggregates, alignment is negligible and mobility measured is, in essence, the orientation-averaged mobility diameter.

Another potential complication of mobility-based measurement of aggregates is that material condensed on the aggregates will change the mobility of the aggregates. Small amounts of liquid which condense on an aggregate can cause the aggregate to restructure due to the surface tension of the liquid (Schnitzler, Gac, & Jäger, 2017b) and cause the mobility diameter to decrease (Corbin et al., 2023; Pagels et al., 2009; Slowik et al., 2007). The degree of restructuring depends on the amount of condensed material (Ghazi & Olfert, 2013), including the material's phase (Corbin et al., 2023) and surface tension (Schnitzler et al., 2017b); the size of the aggregates; and the size of the primary particles within the aggregate (Leung, Schnitzler, Dastanpour et al., 2017). If sufficiently large amounts of liquid are condensed on the aggregates then the mobility diameter can increase. However, due to the fractal nature of the aggregates a considerable amount of condensed material may be present on the aggregate before the mobility increases substantially. For example, Leung, Schnitzler, Jäger et al. (2017) showed that in the absence of particle restructuring, the mobility diameter of a 250 nm soot particle weighing 3 fg would only increase by 5% when 3 fg of organic carbon was condensed on the particle. This is due to the fact that the condensed material can deposit in the crevices of the particles (Schnitzler, Dutt, Charbonneau, Olfert, & Jaeger, 2014) without changing the particle's mobility.

4.2. Aerodynamic distributions

Aerodynamic-equivalent distribution measurements are possible with impactors, aerodynamic classifiers, and time-of-flight (TOF) devices. Early measurements in the field relied on cascade impactors, where multiple impactor stages are stacked on top of each other to collect particles on to plates, which could be weighed to construct mass distributions as a function of aerodynamic diameter, $\partial M/\partial \ln d_{ae}$ (e.g., Berner, Reischl, & Puxbaum, 1984; Goldfarb & Gentry, 1978). However, such a method was very time consuming as a sufficiently large mass needed to be collected on each stage to make accurate mass measurements. Real-time impactor measurements were made possible by charging the particles with a unipolar charger and connecting an electrometer to each impactor stage (Tropp, Kuhn, & Brock, 1980). The charged particles, classified by aerodynamic diameter, impact their respective impactor stage and the electrometer measures the current produced by the charged particles. The current is proportional to the number of particles impacting the electrometer and the number of charges on each particles. Thus, if the charge distribution is known (by calibration), then the aerodynamic count distribution, $\partial N/\partial \ln d_{ae}$, can be found through data inversion. This technique was popularized by the electrical low pressure impactor (ELPI) (Keskinen, Pietarinen, & Lehtimäki, 1992). The ELPI has a wide size range (6 nm to 10 µm) and fast time response. Like real-time mobility spectrometers a sufficient particle concentration is required to make accurate current measurements and the resolution is limited (14 impactor stages spread over a wide range), which is exacerbated by the fact that the aerodynamic size distribution of soot is narrow (compare the GSD of the aerodynamic and mobility distributions in Fig. 6). Although classification of the particles is not affected by charging, the counting is based on unipolar charging, which is correlated with particle mobility diameter rather than aerodynamic diameter. This means that inversion of ELPI data depends on effective density (Charvet, Bau, Bémer, & Thomas, 2015; Maricq, Xu, & Chase, 2006).

The aerodynamic aerosol classifier (AAC) and be used in conjunction with a CPC to measure aerodynamic size distributions analogous to the SMPS system. The AAC consists of two rotating concentric cylinders where the aerosol enters the gap between the cylinder near the inner cylinder and is carried axial down the classifier with a particle-free sheath flow (Tavakoli & Olfert, 2013; Tavakoli, Symonds, & Olfert, 2014), as shown in Fig. 9c. Due to the rotational speed of the cylinders, particles of a narrow range of relaxation time or aerodynamic diameter are extracted from the classifier with a fraction of the flow in the narrow slot near the outer cylinder. Similar to an SMPS, the AAC can be stepped or scanned through a range of setpoints, and the number concentration can be measured with a CPC to determine the size distribution (Johnson, Irwin, Symonds, Olfert, & Boies, 2018; Johnson, Symonds et al., 2021). Unlike the DMA, particle classification does not rely on particle charge thus the transmission efficiency is much higher

(the DMA only classifies particles of one polarity); the data inversion is also simpler, as there are no multiple-charge artifacts; and it can measure large particles ($> 5 \mu m$ in aerodynamic diameter).

Time-of-flight methods can be used to measure the aerodynamic diameter on a single-particle basis in real-time. In this method the aerosol is accelerated in a nozzle and the velocity of the particle is determined by the time it takes to pass through two laser beams as it accelerates ('relaxes') to the new gas velocity at near-ambient pressure conditions (Wilson & Liu, 1980). Calibration is used to relate particle velocities to the aerodynamic diameter of the particle. The aerodynamic particle sizer (APS) is the most commonly used instrument of this class, but it is not used for soot particles because the lower detection limit is 500 nm (Volckens & Peters, 2005).

Time-of-flight (TOF) methods for aerodynamic sizing are also often used on the inlet of aerosol mass spectrometers. In this application, an aerodynamic lens is used to focus the aerosol into a narrow beam (Liu, Ziemann, Kittelson, & McMurry, 1995a, 1995b) and the particles accelerate under near-vacuum pressures. As the aerodynamic diameter is a function of the mean free path of the gas, the aerodynamic diameter of soot measured at low pressures is usually very different from that measured at near-atmospheric pressures. Since this method measures in the free-molecular regime, the measured value is often called the *vacuum aerodynamic diameter* (DeCarlo et al., 2004). In this regime, for fresh fractal soot, both the mass and drag are proportional to $N_{\rm p}$, which then cancels in calculation of the aerodynamic diameter, leaving $d_{\rm ae}$ proportional to $d_{\rm p}$ (Slowik et al., 2007). Partly because the vacuum aerodynamic diameter is difficult to interpret without knowing the particle density and shape, vacuum aerodynamic measurements are often coupled with a mobility or mass classifier to gain further information on the particle (e.g., Zelenyuk, Cai, & Imre, 2006).

Aerodynamic diameter distribution measurements are less common in the literature for soot compared to mobility measurements. Therefore, the reader is referred to the typical mobility distribution properties in Section 4.1 for common soot sources which can be converted to aerodynamic diameter using the relations given in Section 2.

4.3. Single-particle mass, mass distributions, and mass concentrations

It is important to realize that mobility and aerodynamic properties of aggregates are a function not only of the particle but also of the gas. However, the mass of the particle is intrinsic to the particle, making it a primary property of interest. The mass of soot particles is commonly measured with particle mass classifiers or with laser-induced incandescence.

Particle mass analyzers (PMAs) are useful instruments for population-based analysis, operating by classifying particles by mass-to-charge ratio using a balance of centrifugal and electrostatic forces (see Fig. 9b). The first PMA was developed by Ehara, Hagwood, and Coakley (1996) is called the aerosol particle mass analyzer (APM). The APM consists of two rotating concentric cylinders with a voltage potential between them. The electrically-charged aerosol flow is introduced into the gap between the cylinders and travels axially. Particles balanced by the centrifugal and electrostatic forces travel through the classifier, while particles with a higher or lower mass-to-charge ratio impact the outer or inner cylinders, respectively. The classified particles can then be measured by another instrument, such as an electrometer or CPC.

With the APM, both cylinders rotate at the same rotational speed. In this configuration, the centrifugal force increases with radial distance in the gap, while the electrostatic force decreases. This causes particles of the desired mass-to-charge ratio to experience a force system that causes those not at the force balance point to move towards and impact the cylinders, resulting in a loss of transmission efficiency, especially at high resolution. This problem is solved by rotating the inner cylinder slightly faster than the outer cylinder, which results in a centrifugal force which decreases with radius, and a force system that moves the desired particles towards the force balance point. This phenomena was first demonstrated by Olfert and Collings (2005) and commercialized as the centrifugal particle mass analyzer (CPMA).

Although PMAs classify particles by mass, they are not typically used with a CPC to determine count or mass distributions as a function of particle mass (i.e., $\partial N/\partial \ln m_p$ or $\partial M/\partial \ln m_p$), given that small uncharged particles can pass through the instrument when rotational speeds are low, which makes accurate inversion very difficult. Two solutions exist. First, one can heavily charge the particles (e.g., using a unipolar charger, as in Corbin, Johnson et al., 2022; Dickau, Johnson, Thomson, Smallwood, & Olfert, 2015; Symonds, Reavell, & Olfert, 2013) in an attempt to avoid the presence of neutral particles, before applying an appropriate correction to account for the increase in multiply-charged particles. Second, PMAs can be used in tandem with other classifiers (DMA or AAC) or detectors to determine the mass-mobility relationship and mass distribution of the population as discussed in Section 5.2. In the tandem configuration, it is much easier to distinguish and exclude the small uncharged particles. PMAs are also used to calibrate instruments that measure soot mass concentrations (Corbin et al., 2020; Dickau et al., 2015; Symonds et al., 2013) or the mass of an individual soot particle (Irwin, Kondo, Moteki, & Miyakawa, 2013).

The mass of individual soot particles can also be measured using a single-particle soot photometer (SP2), which can be used to build $\partial N/\partial \ln m_p$ or $\partial M/\partial \ln m_p$ distributions. We discuss this further in Section 6.4.3.

Naturally, particle mass distributions can be integrated to obtain total mass concentrations, which are more traditionally measured by gravimetric analysis of filters. The mass concentration of the elemental carbon and organic carbon in a population can be measured using thermal-optical analysis (Birch & Cary, 1996); however, it should be noted that soot also contains small amounts of hydrogen, oxygen, and other elements which are not detected with this method (Corbin et al., 2020; Matuschek, Karg, Schröppel, Schulz, & Schmid, 2007; Michelsen, 2017). Total mass concentrations may also be estimated from several optical techniques. However, mass concentrations provide no information on particle size or morphology unless combined with other integral measures. For example, with knowledge of total mass, material density, overlap coefficient, and total surface area (see the section that follows), one can estimate an average primary particle diameter.

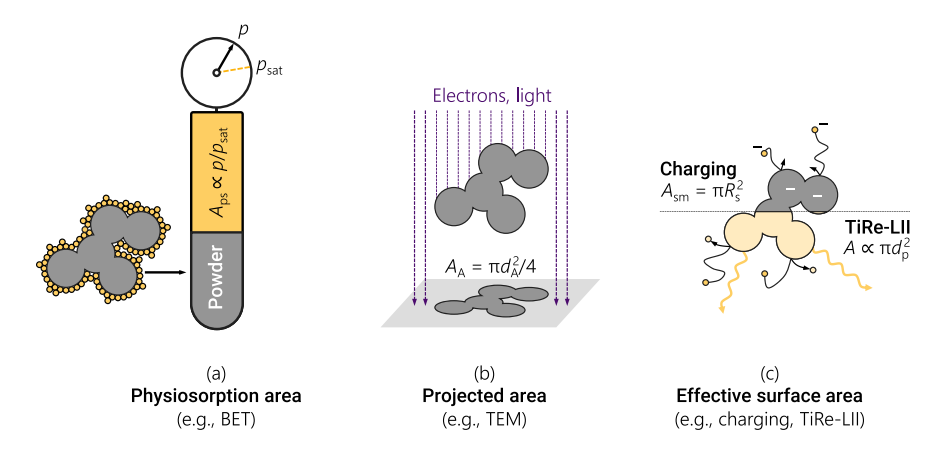


Fig. 10. Schematic depicting measures of aerosol area by means of (a) physical gas adsorption, i.e. physisorption, as in Brunauer–Emmett–Teller (BET); (b) particle projected area, A_{pa} , as in eletronc microscopy; and (c) effective surface areas as determined by molecular, photon, or ion interactions, as in charging devices and time-resolved laser-induced incandescence (TiRe-LII).

4.4. Effective surface area measurements

Surface areas are measured indirectly by means of *effective areas* for molecular adsorption, light–particle interaction, ionic and molecular diffusion, or energy exchange as depicted in Fig. 10. No formal standard exists for measurement of surface area and efforts are ongoing to compare relative measures of surface area to draw comparisons. Surface area measurements are a scale-dependent property and thus inherently dependent on the length scale of *probe* used to measure the particle area, akin to the *coastline paradox*. Thus, differences in molecular or ionic probe size or wavelength of light will probe different length-scales of particle surfaces, from sub-atomic structure and atomic areas ($\sim 10^{-2}$ nm²) to bulk-scale resolution (~ 1 nm²).

The most common technique for bulk scale powder surface area measurements is based on physical gas adsorption (physisorption) onto solid materials. Gas adsorption measures surface area using a probe molecule, e.g., N₂, and is typically described using theory from Brunauer-Emmett-Teller (BET) that extends Langmuir monolayer adsorption to multiple layers (Brunauer, Emmett, & Teller, 1938). Physisorption surface area is typically measured via the relative vapor pressures of N₂ for a chamber with and without (saturation vapor pressure) the sample particles. BET theory is applied to interpret the surface area of the sample, which is commonly normalized by the mass to provide mass specific surface area. BET surface area measurement is a common, commercially-available technique with well-established reviews (Bardestani, Patience, & Kaliaguine, 2019), dedicated textbooks (Masel, 1996), and ISO standards (ISO, 2010). While the technique is the standard of measure for surface areas of activated carbons, catalysts, zeolites, and molecular sieves (Thommes et al., 2015), the minimum required sample mass is large (> 1 mg), which means it is not sensitive enough to measure surface areas of single gas-bourne nanoparticles or aggregates. Several studies use BET to examine the surface area of bulk soot powders from laboratory flames, engines, and fires with a majority of measured mass specific surface areas ranging from 1-100 m²/g (Ouf et al., 2019b; Rockne, Taghon, & Kosson, 2000). Comparison of primary particle surface areas, neglecting porosity, show agreement with geometric surface area estimations using TEM for dry aggregates (OC/EC <20%, Ouf et al., 2019b). For porous particles and aggregates with large organic fractions, there is a larger discrepancy between BET and microscopy measures of surface area. A recent study combining BET measurements with microscopy, tandem classifiers, and X-ray diffraction is described by Trivanovic et al. (2022).

In-situ measurement of aerosols do not rely on vapor pressure measurement but instead employ other physical principles. Real-time measurements of aerosol surface areas commonly exploit surface area transport or light interaction, such as diffusion charging or photoelectric emission with subsequent current measurement. The measured effective surface areas are defined in terms of a measured moment M_{ν} of the size distribution,

$$M_{v} = \int_{0}^{\infty} d^{v} N(d) dd$$
 (28)

where the total surface area of spherical particles is given by $A_{\rm s}=\pi M_2$. For non-spherical aggregates, the mobility diameter in the free molecular regime is equivalent to the projected area diameter, and a strong relationship between mobility and projected area equivalent diameter continues through the transition regime (Rogak, Flagan, & Nguyen, 1993). The projected area can be determined by electron microscopy.

Diffusion-based surface areas are based on the Smoluchowski radius, $A_{\rm sm}=\pi R_{\rm s}^2$, and relate the interaction of particles with diffusing ions to determine charge-based measures of surface area. Diffusion charging imparts charge to particles via ion-particle collisions, which is dependent upon the particle surface area. Often this mass transfer process is characterized in terms of the *Fuchs surface area*, which can be thought of as the surface area of particles in the free molecular regime having the same total mass transfer rate. This will be proportional to the projected area of particles in the kinetic regime but will be smaller than this in the continuum regime where concentration gradients reduce mass transport. There is a strong correlation between mass and momentum transfer,

such that the functional dependencies of particle drag are also relevant to mass transfer. For spherical particles, Fuchs area varies as d^2 in the kinetic regime and d in the continuum regime, similar to momentum transfer (e.g., Eq. (9)). Because the diffusion process depends on the mean free path of the species being transported, the definition of the Fuchs area is not straightforward, as reviewed by Jung and Kittelson (2005). For spheres with diameters of 50–150 nm, the Fuchs area varies approximately as $d^{1.39}$ (Asbach, Fissan, Stahlmecke, Kuhlbusch, & Pui, 2009). For non-spherical particles, diffusion measurements can be used to define equivalent sizes but these sizes are not as straightforward to interpret as the equivalent sphere sizes introduced earlier in this review.

Bipolar charging involves ions of both polarities at nominally equivalent concentrations and achieves a steady-state distribution of charges on particles in accordance with their size and morphology. The detailed kinetics based on Fuchs' theory of particle-ion interactions (Fuchs, 1963) can be solved with known concentrations of particles and ions in addition to particle and ion properties, e.g. mobility, mass, structure, etc. Commonly used relations based on kinetic solutions for bipolar charging include an analytic expression from (Gunn & Woessner, 1956) for larger particles ($d_p > 50$ nm), an empirical expression by Wiedensohler (1988), and modeling by Hoppel and Frick (1986), which have proven robust for typical radioactive bipolar ion sources. These relations agree with recent measurements of aggregate charging up to ± 8 charges within 7%, and the use of equivalent charging diameters can reduce the error to < 3% (Johnson, Symonds et al., 2021). Brownian dynamics models of non-spherical particle bipolar charging confirm that aggregates charge similarly to spheres with the same mobility diameters, so long as the aggregate ratio of projected area to diffusion area is near unity, i.e., $A_{pa}/(\pi R_s^2) \sim 1$ (Gopalakrishnan, Meredith, Larriba-Andaluz, & Hogan, 2013). Differences in the positive and negative ion mobilities during bipolar charging result in a net charge to the aerosol at steady state. The measured current using radioactive chargers has been shown to be proportional to the product of number concentration and mean mobility diameter ($i \sim N d_{pa}$, Nishida et al., 2020).

More commonly, electrometer measurement of current resulting from single-polarity charged particles are used to infer surface areas. Unipolar ions are commonly produced from corona or photoelectric discharge. The unipolar ion and particle interactions achieve high intrinsic charge efficiencies and result in highly charged particles. As unipolar charging of particles does not achieve a steady-state charge distribution, the kinetic processes leading to charging must be carefully controlled to provide interpretable results. Devices that measure current from unipolar diffusion charging are linearly dependent on concentration, N, and have varying dependence on particle mobility diameter, $d_{\rm m}$, where $i \sim N d_{\rm m}^v$, where v ranges from 1.0–1.2 for the NanoTracer (Marra, Voetz, & Kiesling, 2010), NSAM (Jung & Kittelson, 2007), AeroTrak 9000 (Leavey, Fang, Sahu, & Biswas, 2013), Naneos Partector and DiSCmini (Bau, Zimmermann, Payet, & Witschger, 2015; Fierz, Houle, Steigmeier, & Burtscher, 2011; Todea, Beckmann, Kaminski, & Asbach, 2015). Photoionization of particles induced by ultraviolet (UV) light has been employed as an alternative to corona diffusion charging. Photoionization devices that remove electrons result in a positively-charged aerosols where the measured current is proportional to aerosol area, $i \sim N d_{\rm m}^2$ (Nishida, Johnson, Boies, & Hochgreb, 2019a).

Ultraviolet (UV) photoionization sensors rely on the photoelectric effect to charge particles (Nishida, Johnson, Boies, & Hochgreb, 2019b, and references therein). The resulting charge is a function of the material properties of the particle, as well as its surface area. Therefore, this diagnostic can be combined with other techniques to quantify soot surface area. Alternatively, this diagnostic can be used to infer particulate mass and number concentration when variability in size and primary particle diameter is low. The latter approach has been used in commercial devices, including both laboratory-grade and low-cost sensors. UV photoionization sensors have been compared to unipolar-charge sensors (Nishida et al., 2019b), because both techniques provide useful information which can constrain soot concentrations, given specific assumptions, and both show promise for use in low-cost sensors. Due to the complexities of the implicit assumptions, care must be taken when extrapolating both techniques to new systems.

Time-resolved laser-induced incandescence (TiRe-LII, see Section 6.4.3) also provides a measure of area by way of the surface area available for heat transfer.

4.5. Data interpretation

All aerosol measurements benefit from a mathematically sound interpretation of instrument signals that considers true instrument characteristics. However, in studies of aerosol aggregates, it is often useful to make use of subtle changes in response due to morphology that could be lost in a simplistic data inversion approach or that require customized instrument transfer functions. Here we review the fundamentals of instrument transfer functions and data inversion.

4.5.1. The transfer function

Classifiers are inherently imperfect in that they do not precisely measure particles of a single size, instead collecting a range of particles sharing or almost sharing some characteristic. For example, a DMA will transmit particles with some finite range of electrical mobilities, characterized by an instrument resolution, $R_{\rm m}$, in addition to particles that share an electrical mobility but have different mobility diameters due to multiple charging. The former effect is enhanced for small particles, where a larger range of particles can exit, due to diffusion, and some of the particles with the desired characteristic may not. Functions describing the range of particles that can exit a classifier are called *transfer functions* and typically peak about the desired particle size with roughly Gaussian or triangular shapes. Widths of these transfer functions are often characterized with a resolution, $R_{\rm m}$, first stated for the DMA, but since applied to other instruments. Fig. 11 provides examples of transfer functions for 3 instruments.

Knutson and Whitby (1975) solved differential equations marking out particle stream functions through a classifier, using the method to derive transfer functions for the DMA. This method formed the basis of many transfer function calculations. The most popular example is work by Stolzenburg and coworkers (Stolzenburg, 1988, 2018; Stolzenburg & McMurry, 2008) who derived widely-accepted, theoretical transfer functions for the DMA that include particle diffusion. Variants exist to account for the smearing

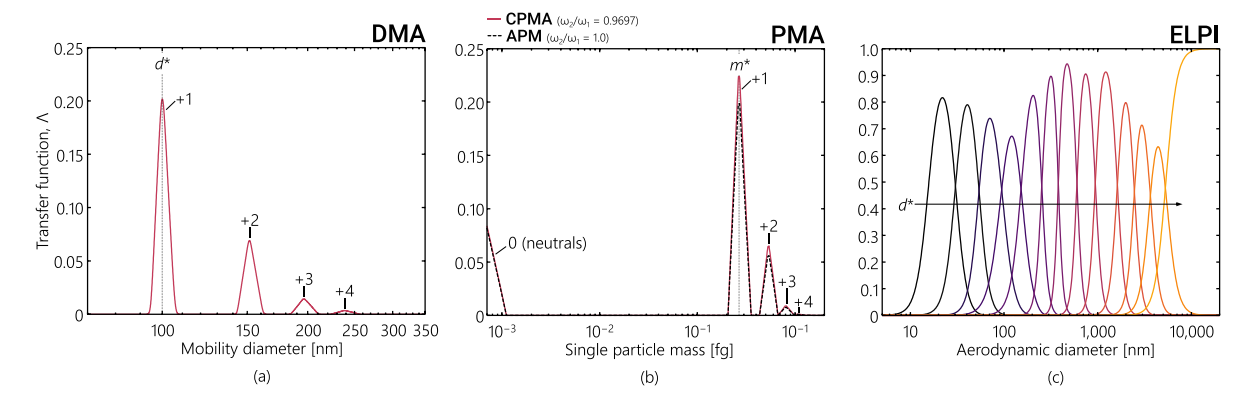


Fig. 11. Realizations of the theoretical transfer functions for (a) a DMA using the diffusing transfer functions of Stolzenburg (2018); (b) a PMA (including realizations for an APM and CPMA) using the functions of Sipkens, Olfert, and Rogak (2020c); and (c) multiple stages of an ELPI. For (a) and (b), multiple charging peaks are clearly visible. Heights of the peaks correspond to charge fractions as evaluated using the models of Wiedensohler (1988) for integer charges of z > 3 and Gopalakrishnan et al. (2013) for integer charges of $z \ge 3$. For (b), a peak is also present for the transmission of neutral particles, which continues to expand to the left of the shown domain. For (c), transfer functions correspond to the difference between the particles collected on each of the stages, with the final stage capturing all particles above $d_{ac} = 10,000$ nm. Experimental transfer functions can differ from these theoretical representations. For (a), see also Figure 2 in Petters (2018), which is similar but also presents the transfer function in terms of the mobility diameter-to-charge ratio (i.e., apparent +1 mobility diameter).

that occurs when scanning DMA classifiers (Kanaparthi, Cevaer, & Dhaniyala, 2018; Mai & Flagan, 2018; Wang & Flagan, 1990) and radial DMAs (Zhang & Flagan, 1996). Ehara et al. (1996) used a similar method to first derive transfer functions for a PMA with electrodes spinning at identical speeds and later incorporated diffusion using stochastic modeling (Hagwood, Coakley, Negiz, & Ehara, 1995). Olfert and Collings (2005) later generalized the transfer function for electrodes spinning at different speeds, supplementing calculations with finite difference simulations of particle concentrations. Sipkens et al. (2020c) used a similar method to derive theoretical transfer functions that allowed for diffusion, allowed modeling of neutrals, and remained computationally-efficient at most conditions. Analytical transfer functions for PMAs have yet to be fully validated experimentally, with real losses through the instruments larger than those predicted theoretically. Tavakoli and Olfert (2013) similarly derived theoretical diffusive and non-diffusive transfer functions for the AAC. Johnson et al. (2018) determined the AAC transfer function empirically to better account for particle losses and flow non-idealities and later derived a scanning AAC transfer function (Johnson, Symonds et al., 2021).

Impactor transfer functions are built by considering how many particles are captured by the current stage (which results in a sigmoidal shape), reduced by all of the particles captured by previous stages, (Marple & Liu, 1974). Transfer functions are naturally quite broad, given the limited size resolution and nature of particle classification. The transfer functions of diffusion batteries are similarly broad Cheng, Keating, and Kanapilly (e.g., 1980).

System transfer functions can envelope a longer train of instruments, for instance also incorporating charge fractions and the response of particle counters (e.g., the CPC in an SMPS) or building transfer functions for tandem systems (see Section 5).

4.5.2. Data inversion for classifiers

The response of a classifier (i.e., the number of particles that make it to a detector) is formed by taking the product of the transfer function, which describes how many particles of a specific size exit the classifier, and the particles size distribution, which describes the size of particles in an aerosol that are available to pass through the classifier. The response at a given setpoint is then the sum of this product across all of the sizes, resulting in a *convolution*. Mathematically, this results in a common form:

$$R_i(s_i^*) = \int_{-\infty}^{\infty} \Lambda(s; s_i^*, c) \left[\frac{\partial Y}{\partial \ln s} \Big|_{s} \right] d\ln s, \tag{29}$$

where $\Lambda(s; s_i^*, c)$ is the aforementioned instrument transfer function (also called the *kernel* in the inverse problems field); s^* defines the setpoint of the instrument, often expressed in the same units as s, and c is some set of supplemental parameters. The resultant expression is a *Fredholm integral equation* and is common in the aerosol literature. The variant without logarithmic spacing is similar, with the integral bounds extending from 0 to ∞ . The process of determining a particle distribution from a set of responses is called *data inversion*, a reference to techniques that use indirect measurements to determine the underlying size distribution that caused those measurements. Reviews from the last 3 decades include Carfora, Esposito, and Serio (1998), Kandlikar and Ramachandran (1999), Voutilainen, Kolehmainen, and Kaipio (2001), Wolfenbarger and Seinfeld (1990), and Świrniak and Mroczka (2022). For many common instruments, most modern data inversion methods will result in similar distributions. However, it is important that practitioners have a general understanding of the process and the kinds of errors or artifacts that can be introduced when processing data, including noise amplification, multiple charging artifacts, and diffusive broadening or asymmetries in the transfer functions. Depending on the instrument, deriving morphology information may also involve a less direct measurement model (e.g., deriving

particle size information from scattering data). Data inversion can overcome these issues, provided that the transfer function is well-enough characterized and with limitations depending on the quality of the measurement. With the development of new instruments, data inversion should be considered as a critical part of the development process.

Schemes for data inversion vary substantially and include least-squares (Haaf, 1980), which performs poorly for real data; the iterative charge correction scheme of Hoppel (1978); the Hagen and Alofs method (Cai et al., 2018; Hagen & Alofs, 1983); Twomey (Collins, Flagan, & Seinfeld, 2002; Twomey, 1965, 1975), which is based on the method of Chahine (1968), and its variants (Markowski, 1987; Winklmayr, Wang, & John, 1990); Tikhonov regularization (Tikhonov & Arseninrs, 1977) (also known as Phillips-Twomey regularization or ridge regression), which often requires heuristic methods to determine a regularization parameter (Hansen & O'Leary, 1993; Talukdar & Swihart, 2003; Wolfenbarger & Seinfeld, 1990); maximum entropy method (Gulak, Jayjock, Muzzio, Bauer, & McGlynn, 2010); expectation–maximization (Cai et al., 2018; Do & Batzoglou, 2008; Dubey & Dhaniyala, 2013); and regularization using other priors via the Bayesian framework (Hogan Jr., Li, Chen, & Biswas, 2009; Ramachandran & Kandlikar, 1996; Voutilainen et al., 2001). This list is by no means exhaustive. Most of these methods reduce the data inversion problem to that of an optimization problem, e.g., least-squares incorporating a penalty term for non-physical results. The problem is typically linear and simple, iterative, linear solvers are best suited to solve the problem. Many such solvers are available in common software packages, which makes the process of solving the system relatively straightforward. An exception is when one infers the GMD and GSD of the distribution, the problem is non-linear and requires non-linear solvers, for which there are also many established solvers such as Levenberg–Marquardt.

Within this context, it is increasingly common to use machine learning and metaheuristic approaches to perform inversion, including, but not limited, the use of to particle-swarm optimization (Nie & Mao, 2022; Yuan, Yi, Shuai, Wang, & Tan, 2010), simulated annealing (Ma, Kranendonk, Cai, Zhao, & Baba, 2009), genetic algorithms (Lienert, Porter, & Sharma, 2003; Mao & Li, 2014; Ye et al., 1999), and ant/bee colony optimization (Wang, Li, & Xing, 2017). Some caution is recommended in this regard. Many of these machine learning approaches amount to optimization schemes that are designed for complex, highly non-linear functions, where the prior information used to stabilize the inference is either non-existent or difficult to ascertain. These approaches may be useful in instances where the optimization function is highly non-linear and multiple local minima may exist (e.g., when the particle size distribution is multimodal or for complex transfer functions). However, in many instances, little is gained when using these algorithms relative to more established solvers at the increased risk of overfitting (when training is involved) or divergence. This is particularly the case for regularized linear problems, which will have a single, global minimum. Further, uncertainty quantification within the context of these approaches can be challenging and is often ignored in the associated studies. By contrast, machine learning tools can be useful in representing the complex physical models required to either model the instrument response or to supplement the data with prior information (for example, the use of physics-informed neural networks or PINNs to encode nonlinear physics into the prior). This is particularly the case for optical instruments, which often have more complex measurement models (e.g., Boiger et al., 2022). In these instances, regularization of the inversion could be embedded into the machine learning approach with improved performance.

4.6. Outlook

The measurement of mobility, aerodynamic, and mass distributions is fairly well-established, and current work is mostly focused on improving range, lowering costs, reducing size, and quantifying uncertainties. In this respect, the number of commercially-available classifiers is continually growing, including the introduction of low-cost sensors that are capable of particle classification. Major challenges still exist for the measurement of surface area, and there is no consensus on how the surface area of soot can be measured as an aerosol. Another major focus of current work is combining measurement techniques to determine morphological properties of aggregate. For example, tandem systems of DMA-PMA, AAC-DMA, or AAC-PMA can all be used to determine particle effective density or dynamic shape factor, if the material density is known (Tavakoli & Olfert, 2014). Early work focused on determining the *average* effective density or shape factor as a function of particle size. However, due to the fractal-like structure of aggregates, a wide distribution of morphologies may be contained in an aerosol population at a given particle size (or mass). Thus, future work will be focused on using tandem instruments to measure the *distribution* of the population using multi-variable distributions, such as count distributions as a function of mobility and mass, $\partial^2 N/\partial \ln d_{\rm m} \partial \ln m_{\rm p}$, as described in the section that follows.

5. Tandem measurements

Single classifiers are designed to target a single particle characteristic, such as mobility or particle mass. Placing multiple classifiers in series, constituting a tandem arrangement, allows practitioners a route to characterize otherwise inaccessible properties of the particles, such as effective density, though typically at the cost of an increase in experimental time and complexity. A review of tandem measurements up to 2008 was provided by Park et al. (2008).

The oldest examples of tandem measurements are tandem DMA (TDMA) systems, typically pairing two DMAs with a CPC, with several variants available in the literature. Most cases place a particle conditioner between the DMAs, which can include: (1) a humidifier, resulting in the humidified TDMA (HTDMA) system (Liu et al., 1978; McMurry & Stolzenburg, 1989; McMurry, Takano, & Anderson, 1983; Rader & McMurry, 1986; Weingartner, Baltensperger, & Burtscher, 1995; Weingartner, Burtscher, & Baltensperger, 1997); (2) a heated section, resulting in the volatility TDMA (VTDMA) system (Covert & Heintzenberg, 1993; Orsini, Wiedensohler, Stratmann, & Covert, 1999; Philippin, Wiedensohler, & Stratmann, 2004; Rader & McMurry, 1986; Rader, McMurry, & Smith, 1987;

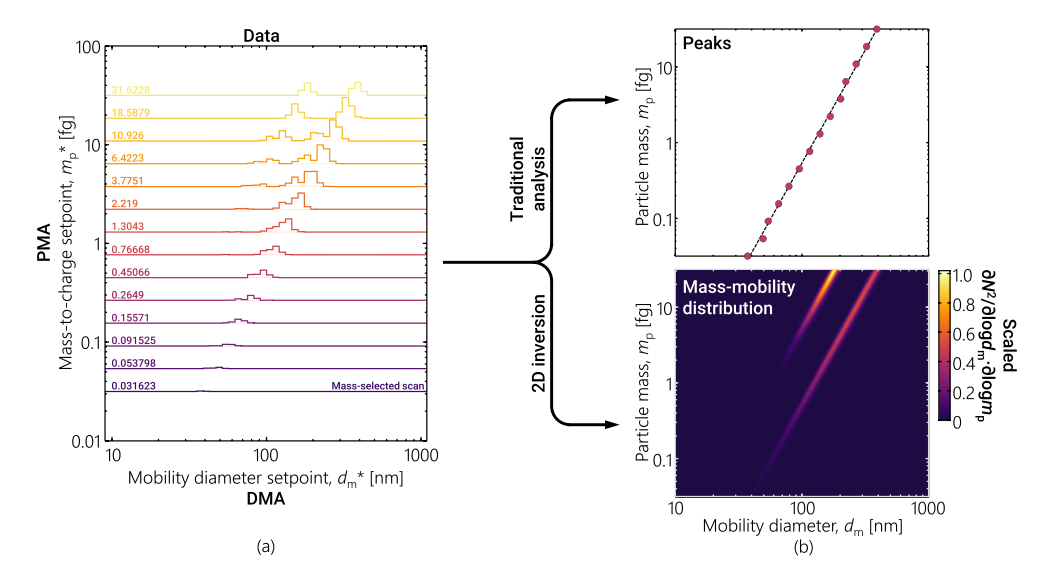


Fig. 12. Demonstration of the two-dimensional nature of tandem measurements, using the multimodal mass-mobility distribution employed by Buckley, Kimoto, Lee, Fukushima, and Hogan Jr. (2017). (a) Simulated measurements, where horizontal lines would correspond to SMPS scans at a single PMA setpoint. (b) Traditional routes to analysis can involve choosing the peak in the measurements, and plotting these as a series of points (top panel). This can introduce discretization errors and either abrupt shifts or missed modes (as is the case here) in the presence of mixed particle populations. Alternatively, the data can be inverted to give the two-dimensional mass-mobility distribution (bottom panel).

Schmidt-Ott, 1988); and (3) a mixing chamber with some kind of reactant, resulting in the reaction TDMA (RTDMA) system (Cruz & Pandis, 1998; Fenidel, Matter, Burtscher, & Schmidt-Ott, 1995; Gupta, Tang, & McMurry, 1995). For example, Liu et al. (1978) first used a TDMA system to examine the deliquescent and hygroscopic properties of mobility-classified particles. McMurry et al. (1983) added a third DMA in conjunction with a humidifier, where the first two DMAs were used to reduce multiple charging artifacts (by re-neutralizing), followed by a humidifier and the third DMA. Rader and McMurry (1986) provided a general overview of the TDMA approach, which acts as a landmark study, including the different variants. The use of TDMA expanded into a standard technique throughout the 1990s (Fenidel et al., 1995; McMurry et al., 1996; Weingartner et al., 1995, 1997).

Fundamentally, tandem measurements map out the quantity of particles on a grid with respect to two particle properties. Fig. 12 shows an example of this procedure for particle mass and mobility diameter. Each cell in the lower panel of Fig. 12b denotes the number of particles that have a mass between m_p and $m_p + \Delta m_p$ and mobility diameter between $d_m + \Delta d_m$. Within this framework, measurements made using a single classifier correspond to the sum of elements in a single direction. For example, within Fig. 12, an SMPS would measure the sum in the vertical direction, i.e., all of the particles with a given mobility diameter, regardless of their mass. By contrast, a PMA would measure the sum in the horizontal direction, i.e., all of the particles with a given particle mass, regardless of their mobility diameter. What is gained from using the tandem measurements is the relationship between the two particle sizes, which can, in turn, be related to the fractal properties and effective density.

5.1. Data inversion for tandem measurements

Traditionally, tandem instrument data is treated as a set of 1D measurements (e.g., a set of SMPS scans) that are inverted individually and compiled (the upper stream of Fig. 12). For example, Voutilainen, Stratmann, and Kaipio (1999) employed Tikhonov regularization to invert TDMA data, adding a weighting operator that modifies traditional Tikhonov such that the smoothing becomes smaller in the regions where the size distribution changes rapidly. Similarly, for a combination of a DMA and PMA, the particle mobility and mass can be used to compute effective densities. Pairings of mass and mobility are typically taken from the peak of each scan of the DMA and plotted as a function of particle mass.

An alternative of the problem is to consider that the tandem measurements represent an underlying 2D distribution, with 2D transfer functions (e.g., those shown by Song, Pei, Liu, Zhou, & Wang, 2022). Mathematically, the form is similar to that for a single classifier, Eq. (29), but integrates over the response of both classifiers:

$$Y(s_1^*, s_2^*) = \int_{-\infty}^{\infty} \int_{-\infty}^{\infty} \Lambda(s_1, s_2; s_1^*, s_2^*, c) \left[\frac{\partial^2 Y}{\partial \ln s_1 \partial \ln s_2}(s_1, s_2) \right] d\ln s_1 d\ln s_2, \tag{30}$$

where s_1 and s_2 are the two particle properties. The double convolution characteristic of tandem systems was first described by Rader and McMurry (1986) and Stolzenburg and McMurry (2008), and was expanded upon by several others (Broda et al., 2018; Buckley et al., 2017; Sipkens, Olfert, & Rogak, 2020a). Carsí and Alonso (2022) instead presented a unified transfer function for multiple DMAs. More recently, Petters (2018, 2021) and Oxford, Chakrabarty, and Williams (2022) revisited this data inversion approach, providing an overview to data inversion within this context. Data inversion to explicitly retrieve these 2D distributions, as pioneered

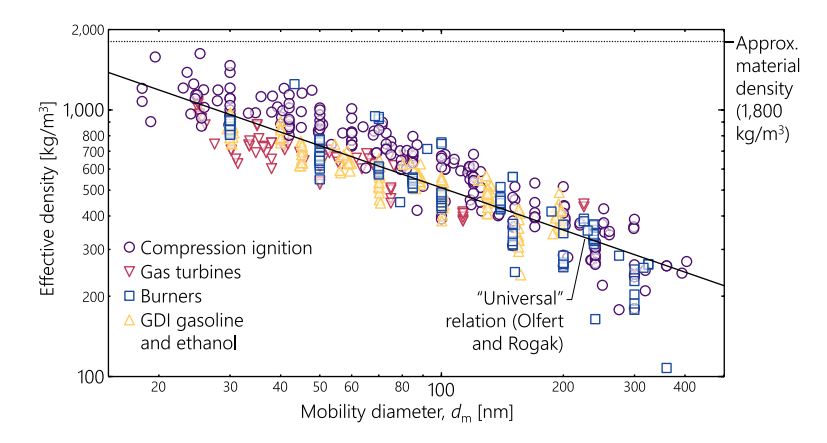


Fig. 13. Data for the effective density-mobility diameter relationship for a range of soot sources. Both axes are logarithmic, such that the mass-mobility relation appears as a linear line. Lacy soot results are adapted from the universal relation of Olfert and Rogak (2019). Data is even distributed about the relation. Collapsed soot can exhibit higher densities (Chen, Enekwizu et al., 2018; Corbin et al., 2023; Ghazi & Olfert, 2013; Leung, Schnitzler, Dastanpour et al., 2017; Pagels et al., 2009; Schnitzler et al., 2017b; Zangmeister et al., 2014).

by Rawat et al. (2016) and Buckley et al. (2017), is an emerging technique. An overview of several of the methods available to perform this inversion is available in Sipkens et al. (2020a) and Sipkens, Olfert, and Rogak (2020b). The technique is particularly useful for teasing out distinct modes of temporally static distributions. This comes at a cost of more computational effort (though this can be helped by truncating the inversion domain Sipkens, Trivanovic et al. (2021)) and complexity.

5.2. Tandem systems targeting particle shape and effective density

The shape and effective density of aggregates are challenging to measure, due to the complex morphology of the particles, with several techniques attempting to measure the quantity (Park et al., 2008; Shapiro et al., 2012). Some have used two parallel classifiers for this task, fitting size distributions to the two sets of measurements before comparing the response, or using only the distribution modes to obtain an average quantity (Brockmann & Rader, 1990; Kerminen, Mäkelä, Hillamo, & Rantanen, 1999; Ristimäki, Virtanen, Marjamäki, Rostedt, & Keskinen, 2002). However, the number of assumptions can be reduced drastically by using tandem measurements. A review of some of these configurations was provided by Peng et al. (2021).

Kelly and McMurry (1992) initially paired a DMA with inertial classifiers (e.g., impactors) to simultaneously classify particles with respect to mobility diameter and aerodynamic diameter. Ahlvik, Ntziachristos, Keskinen, and Virtanen (1998) computed effective densities for diesel particles using a DMA-ELPI system. The DMA-ELPI system has since been used to characterize soot from diesel engines (Maricq, Podsiadlik, & Chase, 2000; Van Gulijk, Marijnissen, Makkee, Moulijn, & Schmidt-Ott, 2004; Virtanen et al., 2002) and gasoline port fuel injected engines (Maricq et al., 2000). More recently, impactors have been supplanted by the APS (Charvet, Bau, Paez Coy, Bémer, & Thomas, 2014; Saarikoski et al., 2005) (though less often for soot due to limitations in the range of sizes that can be measured) and the AAC (Kazemimanesh et al., 2022; Tavakoli et al., 2014).

The advent of the PMAs, when combined with mobility diameters from a DMA, allowed more direct measurement of effective density, via Eq. (13), or the mass-mobility relation parameters, i.e., k and $D_{\rm m}$. Measurements date back to McMurry, Wang, Park, and Ehara (2002) who originally paired an APM with a DMA to compute effective density. Since, the technique has become a mainstay in the literature, having been applied to a range of particles, including sodium chloride (Beranek, Imre, & Zelenyuk, 2012; Kuwata & Kondo, 2009; Park, Kittelson, & McMurry, 2003), metal nanoparticles (Charvet et al., 2014; Shin et al., 2009), and, more relevant to this review, combustion-generated aggregates from diesel engines (Olfert, Symonds, & Collings, 2007; Park, Cao et al., 2003; Quiros et al., 2015), lab burners (Afroughi, Falahati, Kostiuk, & Olfert, 2019; Dickau et al., 2016; Ghazi et al., 2013), gasoline direct injection (GDI) engines (Graves, Koch, & Olfert, 2017; Quiros et al., 2015), aviation turbines (Johnson, Olfert, Symonds et al., 2015; Olfert et al., 2017), and tobacco (Johnson et al., 2014; Johnson, Olfert, Cabot et al., 2015) and cannabis (Graves et al., 2020) smoke. Olfert and Rogak (2019) recently used this ensemble of literature values to define a "universal" (or "typical") mass-mobility relation for soot, shown in Fig. 13, on the premise that most soot particles (in the absence of coatings) are described by similar trends in terms of effective density. The technique has also been used to characterize soot aggregate restructuring, reminiscent of atmospheric processing (Khalizov, Hogan, Qiu, Petersen, & Zhang, 2012; Leung, Schnitzler, Dastanpour et al., 2017; Leung, Schnitzler, Jäger et al., 2017; Pagels et al., 2009; Radney et al., 2014; Rissler et al., 2014; Schnitzler et al., 2017b; Xue, Khalizov, Wang, Zheng, & Zhang, 2009; Zangmeister et al., 2014; Zhang et al., 2008). Radney and Zangmeister (2016) discussed some of the limitations that remain in this technique, with some recommendations for good practice. Kazemimanesh et al. (2022) used a CPMA-DMA-AAC system to assess particle shape, where the added classifier reduces the artifacts due to charging and relies less on assumed relationships between the

A variation using a tandem mass-mobility measurement is the mass and mobility aerosol spectrometer (M2AS), which uses a unipolar charger, CPMA, mobility separator (a mobility classifier with two outlets for high and low mobility particles), and two

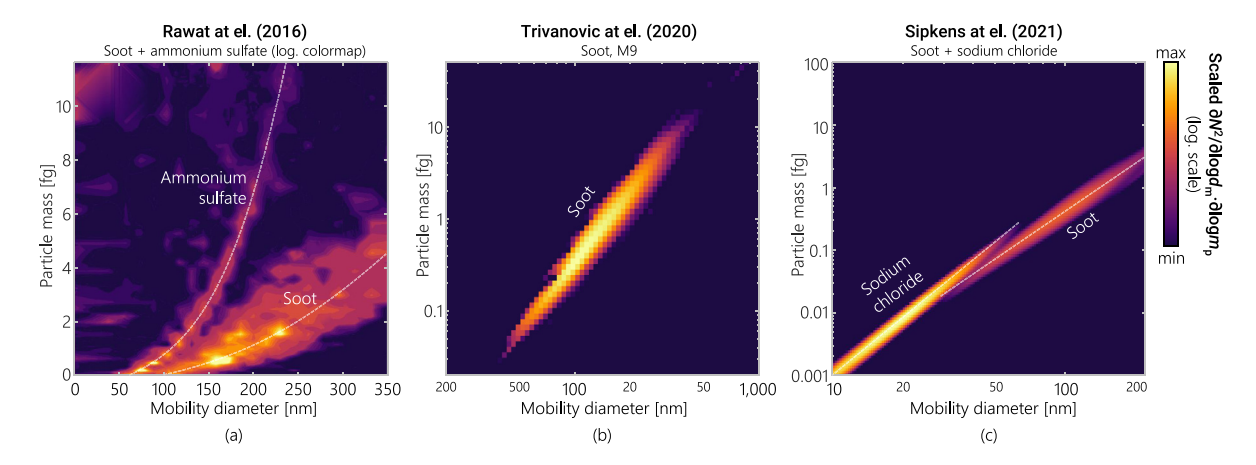


Fig. 14. Two-dimensional mass-mobility distributions containing soot-containing particle populations from (a) Rawat et al. (2016) (Fig. 6a), (b) Trivanovic et al. (2020), and (c) Sipkens, Trivanovic et al. (2021). For (a), figure was adapted to this format, with the *x*-axis converted to fg. Note that the *x*- and *y*-axes are not logarithmic, differing from the other panels. The colormap is on a logarithmic scale in all figures, which required an adaptation of the original figures in (b) and (c).

electrometers. By stepping the CPMA and balancing the current measured by the high- and low-mobility electrometers, the particle mobility distribution, mass distribution, and average effective density is determined (Cambustion, 2022). Measurements may also be sped up by using mobility spectrometers (Johnson, Olfert, Cabot et al., 2015; Johnson, Olfert, Symonds et al., 2015), though at a loss of accuracy.

More recently, similar measurements have been used in conjunction with 2D inversion techniques to map out mass-mobility distributions, which extend beyond trends in the relationship between the classified size and mass, adding distribution widths and enabling analysis in the presence of mixed particle populations. Rawat et al. (2016) and Buckley et al. (2017) first reported mass-mobility distributions, including some for soot. The technique has since been applied experimentally to a variety of aerosols, e.g., (Chen, Ghosh et al., 2018; Li et al., 2020; Sipkens, Trivanovic et al., 2021; Trivanovic et al., 2020). Of note here, Trivanovic et al. (2020) used this method to characterize soot generated by a lab-scale flare, across a range of fuels. Tandem measurements of this kind are particularly useful when multiple particle populations are present, such that the technique has also been used to tease out separate, but overlapping, populations of soot mixed with ammonium sulfate (Rawat et al., 2016) and sodium chloride (Sipkens, Trivanovic et al., 2021). These three cases are shown in Fig. 14. Early results show that soot is associated with broad distributions, especially relative to other particle types, due to the range of structures, primary particle sizes, and orientations that could occur for an aggregate of a given mass.

A number of comparisons of these tandem arrangements for determining particle shape exist in the literature. Schmid, Karg, Hagen, Whitefield, and Ferron (2007) presented an overview of these competing techniques up to that point, including some contrast of the analysis routines. Yao et al. (2020) provided some discussion the equivalencies between classification with a DMA, APM, and AAC, and computing the particle shape from different pairings experimentally. Kazemimanesh et al. (2022) also presented some comparison of different tandem arrangements, including DMA-CPMA, AAC-DMA, and AAC-CPMA. Song et al. (2022) examined the transfer functions of combined DMA-CPMA and DMA-AAC systems, with outlooks towards removing multiple charging artifacts. Overall, more work is needed to understand the uncertainties in these different kinds of measurements.

5.3. Other tandem measurements

Tandem arrangements have been used to assess soot mixing state, which refers to how populations of soot aggregates are mixed, typically with other types of particles (Riemer et al., 2019). *Internally mixed* particles are those that contain two components within the same particle, including those containing volatile or inorganic components, while *externally mixed* particles are aerosol populations that have particles of two types, without those components being combined in single particles. Traditional routes to assessing mixing state largely depend on filter measurements, e.g., thermal optical analysis (see also Section 4.3). Dickau et al. (2016) presents a methodology for quantifying the volatile mixing state of an aerosol using a combination of different tandem arrangements of a DMA, CPMA, CPC, and a denuder; however, the method is time consuming. More recently, a combination of a classifier and a Single-Particle Soot Photometer (SP2) has been used to assess the relative refractory content of carbonaceous particles as a function of size or mass. Within this context, existing studies have only used the incandescence signal of the SP2, which acts as a particle counter while simultaneously quantifying the mass of the refractory content of the particles. Liu et al. (2017) first paired a CPMA with an SP2 to quantify black carbon absorption enhancement as a function of mixing state. Broda et al. (2018) later adopted the same setup but used the aforementioned 2D inversion techniques to map out refractory black carbon mass as a function of particle mass, a technique later optimized by Naseri, Sipkens, Rogak, and Olfert (2021, 2022). A number of other studies have instead placed a DMA in front of the SP2 to various ends (Han, Li, Liu, & Lee, 2018; Hu et al., 2021, 2022; Zhao et al., 2022; Zhao, Zhao,

& Zhao, 2019), e.g., to determine volume-equivalent diameter and, by extension, the dynamic shape factor in addition to mixing state information (Hu et al., 2022). Pan et al. (2019) used a tandem arrangement of an AAC-DMA-SP2 to assess mixing state, an arrangement used experimentally since Wang et al. (2021). Riemer et al. (2019) also provided a list of common abbreviations used within this field.

Johnson and coworkers also used a tandem AAC-DMA arrangement to quantify the charge distribution of spherical (Johnson et al., 2020) and, more relevant to this review, non-spherical (Johnson et al., 2021b) particles. Morán et al. (2023) used tandem DMA and a nano DMA-aerodynamic particle sizer arrangement to compute two-dimensional particle size and charge distributions.

It is also possible to combine a DMA with TEM to derive size information (e.g., Park, Kittelson, McMurry et al., 2004; Rogak et al., 1993). This is more indirect than aerodynamic-mobility measurements and requires significant effort to analyze enough images to achieve sufficient statistics from the TEM images.

Several other tandem systems were reviewed by Park et al. (2008), including those using TOF-AMS and cloud condensation nuclei counters (CCN).

5.4. Outlook

Absolute statements of particle morphology remain challenging, varying depending on the precise pairing of instruments and may depend on the order of the instruments. Theoretically, the particles should see the same set of forces, regardless of the order of the instruments. However, practical aspects of the measurements may cause deviations from this theoretical framework, including non-linearities and flow boundary layer effects carrying over from one instrument to another, and represents an area of future research. Despite these limitations, it is clear that these arrangements can be used to determine changes in particle morphology, e.g., when the soot aggregates have collapsed.

Reconstructions of 2D distributions allows for more information on the range of shapes possible for non-spherical particle populations, including soot. With improved classifiers, it may be possible to extend this treatment to other multimodal distributions, such as those associated with soot evolution in the atmosphere, though with limited temporal resolution associated with longer collection times.

6. Optical techniques

Aerosol particles can scatter, absorb, and emit light, enabling optical diagnostics that provide powerful, potentially real-time, and even *in situ* (e.g., within flames, engines, or reactors) measurements of aerosol physical properties. Optical diagnostics are valued for their direct relationship to the radiative properties of soot, which are relevant to heat transfer in the contexts of climate and combustion science. Given that light scattering and absorption by soot aggregates are controlled by the aggregate's refractive index, size, and shape (Bohren & Huffman, 2008; Sorensen, 2001), optical diagnostics are also useful for characterizing particle morphology.

In this section, we focus our discussion on light scattering and absorption and their use to characterize size and shape rather than number or mass concentration. Studies which discuss extinction (the sum of scattering and absorption) normally do so under conditions where either scattering or absorption dominate the total extinction, which occurs for non-absorbing or very small particles, respectively. Alternatively, studies may use a change in extinction to infer absorption (as in filter photometers) or may combine extinction and scattering measurements to infer absorption. All of these applications of extinction may be understood as applications of absorption and scattering where size information cannot be directly extracted. In addition, we do not discuss those optical diagnostics which only detect particles much larger than the typical size of soot, e.g., particle image velocimetry (PIV) and phase Doppler anemometry (PDA)/phase Doppler interferometry (PDI) (Kulkarni, Baron, & Willeke, 2011).

The relationship between optical and morphological properties is complex, so that a direct interpretation of optical measurements in terms of particle morphology often requires some assumptions. This does not mean that optical methods are not useful and powerful. However, it does preclude a direct, clear, mathematical comparison of optical properties with the physical properties discussed in Section 2. In practice, such comparisons are rarely necessary as researchers often combine optical and physical properties to derive single-particle optical properties.

In the following, we provide a conceptual introduction to the various optical diagnostics that are sensitive to the size and morphology of soot. Given the depth of literature on this topic, we provide an overview to give the practitioner an appreciation of the capabilities of optical diagnostics. As such, we begin with a brief introduction to basic aerosol optics before describing specific diagnostic techniques, relying substantially on existing reviews in the literature for detailed discussion.

6.1. Refractive index

The refractive index of any material is a function of its molecular structure and determines how the material interacts with incident light. It is the refractive index of soot aggregates that makes them so highly absorbing, relative to other aerosol particles. The refractive index of different soot particles may vary (Kahnert & Kanngießer, 2020), since the molecular structure of soot is itself somewhat variable. This variation is often referred to as the degree of graphitization, since the typical endpoint of so-called mature soot is a high degree of graphitization (Liu, Yon, et al., 2020; Michelsen et al., 2020). Particles with a lower degree of graphitization absorb less light per unit mass, and are found at the smallest size range of many soot sources (Corbin, Johnson et al., 2022), in coal

and heavy-oil emissions (Bond, 2001; Corbin et al., 2019), in premixed flames (Wan, Shi, & Wang, 2021), and in quenched flames, such as the commercially available miniCAST soot generator (Malmborg et al., 2019).

Experimentalists must use caution when determining the soot molecular structure, as it may change during analysis, such as under an electron beam during TEM (Botero et al., 2021) or during laser-induced incandescence (Vander Wal & Choi, 1999). The latter scenario has received renewed attention in recent years (e.g., Migliorini, Belmuso, Ciniglia, Dondè, & De Iuliis, 2022; Török, Mannazhi, Bergqvist, Le, & Bengtsson, 2022). Light absorption measurements must also be made with care to avoid artifacts (Bond & Bergstrom, 2006). The conversion of light absorption measurements to refractive index requires a physical model, which requires consideration of aggregate morphology, and therefore introduces some uncertainty (Liu, Yon, et al., 2020). Given the complexity of this conversion, as well as natural variability between soot particles depending on their source and size (Corbin, Johnson et al., 2022), no single refractive index is universally applicable (Geigle et al., 2022) and distributions may prove more useful in describing these properties in the future (e.g., Moteki, Ohata, Yoshida, & Adachi, 2023). However, the following value is a useful reference and is consistent with recent measurements of aerosol light absorption (Liu, Yon, et al., 2020):

$$\mathbf{m} = 1.66 + 0.76i,\tag{31}$$

which is defined for a wavelength of $\lambda = 550$ nm. We apply this value in this work. Relevant to subsequent discussion, this corresponds to $|\mathbf{m}| = 1.83$ and $|\mathbf{m} - 1| = 1.01$.

It is generally accepted that the refractive index of soot is weakly dependent on wavelength through the visible and near infrared (Bond & Bergstrom, 2006; Kahnert & Kanngießer, 2020; Liu, Chung, Yin, & Schnaiter, 2018; Moosmüller, Chakrabarty, Ehlers, & Arnott, 2011) (this results in an Angstrom exponent of AAE = 1 for a Rayleigh absorber), with sharper spectral features in the ultraviolet spectrum (Chang & Charalampopoulos, 1990). However, uncertainties in spectral trends remain, driven in part by the fact that, while the refractive index is the fundamental quantity determining optical properties, the refractive index is not measured directly. Rather, the quantity is inferred from absorption and scattering measurements using combined morphological and optical models of the particles (Liu, Yon, et al., 2020). Thus, a range of models can result in differing trends for the same measurements. Further, uncertainties stemming from variations in the refractive index with soot maturity and composition seem to significantly overshadow spectral trends in most applications. Brown carbon with its higher organic content, for instance, is expected to result in a much stronger wavelength dependence, hence the name.

6.2. Size regimes and modeling basics

Light scattering and absorption regimes are largely prescribed by the ratio of particle size to the wavelength of light, that is, the size parameter:

$$x = \pi d/\lambda. \tag{32}$$

For aggregates like soot, the size parameter may be calculated relative to the primary particles, $x_p = \pi d_p/\lambda$, or to the overall aggregate, $x_a = 2\pi R_g/\lambda$. When $x \ll 1$, the wavelength of light is much larger than the particle size, and the particles see a uniform external electromagnetic field. Light interaction is said to occur in the *Rayleigh regime* when a second condition is also met:

$$x |\mathbf{m}| \ll 1,\tag{33}$$

which corresponds to *optically soft* particles. These two conditions yield an electromagnetic field that is uniform within the particle (Sorensen, 2001). For soot, $|\mathbf{m}|$ is typically small enough that x is sufficient to indicate the regimes³. At the other extreme, $x \gg 1$, light interaction is said to occur in the *geometric optics regime*, where scattered and absorbed light depends on the particles's projected area. For spheres, the absorption and scattering from particles is described more generally by Mie theory, which predicts oscillatory patterns in the transition between the aforementioned regimes. However, Mie theory does not accurately predict absorption and scattering for non-spherical particles. For the special case of fractal aggregate particles like soot, Rayleigh–Debye–Gans Fractal Aggregate theory (RDG-FA) (Farias, Carvalho, Köylü, & Faeth, 1995; Köylü & Faeth, 1994) is often used (Kahnert & Kanngießer, 2020; Liu & Mishchenko, 2005; Mishchenko, 2009). The theory is an application of the RDG approximation (Bohren & Huffman, 2008), which breaks the volume of an arbitrarily-shaped particle into a collection of sub-volumes that do not scatter light between one another. In RDG-FA theory, the sub-volumes are taken as the primary particles of the soot aggregate and the size parameter is taken as x_p^4 . For visible and infrared light, $x_p \ll 1$ is generally satisfied for soot aggregates. The RDG-FA-predicted scattering and absorption cross sections are presented in Fig. 15 for the refractive index provided in Section 6.1. Absorption is larger than scattering over most of the size range relevant to soot.

The assumptions behind RDG-FA can lead to biases due to particle size, primary particle overlap, and polydispersity, among other factors (Kahnert & Kanngießer, 2020). Advanced methods for use in these cases include the discrete dipole approximation (DDA), T-matrix methods (e.g., multisphere T-matrix; MSTM; Mishchenko, 2009; Mishchenko, Travis, & Mackowski, 1996), and generalized multiparticle Mie-solution (GMM) (Liu, Wong, Snelling, & Smallwood, 2013b). These methods are computationally expensive, requiring a range of realistic aggregate morphologies (e.g., aggregates generated via DLCA) and averaging over many

³ The same is not true for other materials, such as metallic particles, which requires one to check both conditions.

⁴ Strictly speaking, the formal conditions for RDG are not met for soot (Kahnert & Kanngießer, 2020; Sorensen et al., 2018), given that $|\mathbf{m}| \approx 1$. However, applying the Rayleigh approximation to the primary particles seems to implicitly satisfy the constraints for RDG.

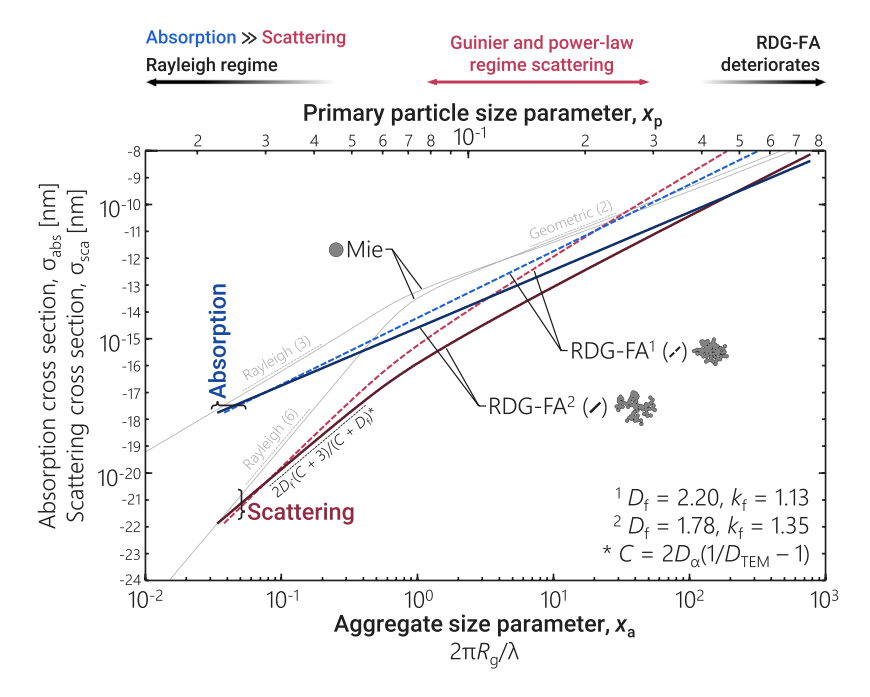


Fig. 15. Absorption and scattering cross sections as a function of the particle size parameter at $\lambda = 532$ nm. Note that, unlike Mie theory, the RDG-FA absorption results do not show an inflection about where $x_a = 1$ as validity is instead determined solely by x_p . RDG-FA results begin to become inadequate at the right edge of the plot where $x_p \to 1$. Slopes for the scattering and absorption of sphere are -6 and -3, respectively, in the Rayleigh regime where $x_a < 1$. Slopes in the RDG-FA-predicted scattering in the same regime exhibit slopes less than -6 (very roughly, $2D_f$) given that the product of the primary particle size and mumber of primary particles do not scale linearly with the primary particle diameter and number of primary particles is computed from the radius of gyration assuming *typical* soot (see also Table 2), specifically using the stated value of D_a , k_a , D_{TEM} , and $d_{p,100}$. Trends here are used to compute particle size in optical particle counters. Equivalent experimental data for soot is not widely available.

particle orientations. Studies relaxing the assumptions of RDG-FA and comparing more complete models to RDG-FA have become commonplace in the literature (e.g., Kelesidis et al., 2020; Liu et al., 2013b; Liu, Yon, & Bescond, 2016; Ma, 2011; Moghaddam et al., 2017; Talebi-Moghaddam, Bauer, Huber, Will, & Daun, 2020; Yon et al., 2015, 2014). Experimental data to support such detailed modeling are rare. However, current evidence suggests that the impacts of these properties leads to less variability than the intrinsic variability in refractive index between sources, at least for light absorption (Corbin, Johnson et al., 2022).

6.3. Light scattering

Formally, light-scattering diagnostics include both elastic scattering and Raman (inelastic) scattering. Nanoparticle light scattering is normally elastic, which is more useful for probing soot particle morphology and size⁵. Elastic light scattering (ELS) from a single-particle is generally described by the Mueller matrix (Bohren & Huffman, 2008), which considers the state of polarization of the incoming and scattered radiation. Here, we consider only the most basic elements of the theory that can be used to relate aggregate structures to common measurement techniques. We refer the reader to previous work (Bohren & Huffman, 2008; Mishchenko, 2009; Moosmüller et al., 2009; Sorensen, 2001; Sorensen et al., 2018) for additional discussion of the underlying physics.

6.3.1. Fundamentals

For RDG-FA, the forward scattering of primary particles adds in-phase and yields a scattering intensity proportional to N_p^2 . This anchors the magnitude of the scattering and is combined with a structure factor for the aggregate to yield the angular scattering of the particle or the scattering *phase function* (the angular scattering normalized over the unit sphere). The forward Rayleigh scattering from a small (relative to λ), isolated primary particle is given by

$$I_{\text{agg},0} = \frac{\partial \sigma_{\text{sca,p}}}{\partial \Omega} = \frac{\pi^4}{9} \frac{d_p^6}{\lambda^4} F(\mathbf{m}),\tag{34}$$

where Ω is the solid angle and $F(\mathbf{m})$ is the square of the Lorenz-Lorenz factor (Sorensen et al., 2018),

$$F(\mathbf{m}) = \left| \frac{\mathbf{m}^2 - 1}{\mathbf{m}^2 + 2} \right|^2. \tag{35}$$

⁵ Raman scattering can be used to determine the structure of the soot on smaller scales, internal to the primary particles (Michelsen, 2017).

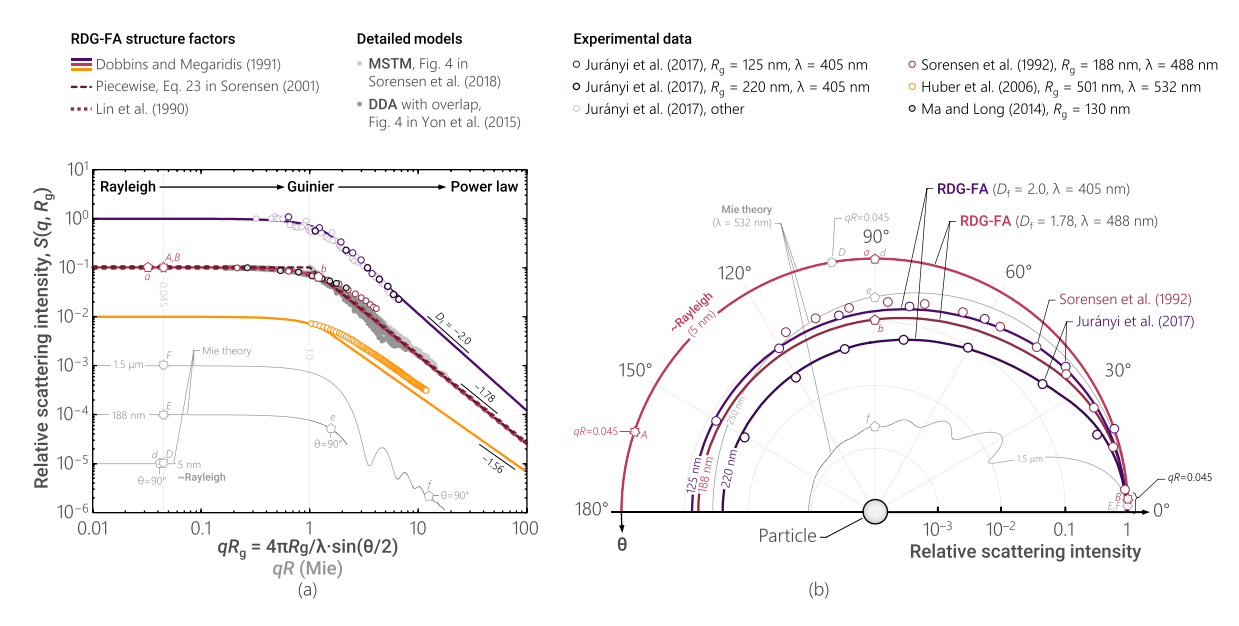


Fig. 16. Relative scattering intensity or structure factor as a function of (a) qR (for Mie) or qR_g (for RDG-FA), offsetting curves by factors of 10 for display purposes, and (b) the scattering angle across different models for incident light polarized perpendicular to the scattering plane. In all cases, quantities are scaled by the forward scattering (or approximately so for experimental data). Complex index of refraction is constant throughout at m = 1.75 + 0.63i. Experimental data is from a number of sources (Huber, Altenhoff, & Will, 2016; Juranyi, Loepfe, Nenkov, & Burtscher, 2017; Ma & Long, 2014; Sorensen, Cai, & Lu, 1992b). Note that the data from Ma and Long (2014) do not extend sufficiently into the power law regime to easily compute a fractal dimension. In (a), Mie results are truncated in q-space for the range of angles from 0 to 180°. A similar principle applies to the RDG-FA curve, but will involve truncation of the single curve shown. RDG-FA curves differ in terms of the fractal dimension. For (b), RDG-FA curves are realized for the conditions from (Juranyi et al., 2017) and Sorensen et al. (1992b). Seven pointed stars correspond to the scattering for qR = 0.045 on each curve, while pentagons correspond to scattering angles of $\theta = 90^{\circ}$ on each curve, which act as reference points in comparing the panels. Filled dots correspond to (light gray) multiple sphere T-matrix (MSTM) results from Fig. 4 in Sorensen et al. (2018) and (darker gray) discrete dipole approximation (DDA) results incorporating some level of necking and overlap from Fig. 4 in Yone tal. (2015). These data largely collapse in qR_g space but will not in terms of angular scattering. Trends here are used to compute particle size when measuring multiangle light scattering (MALS).

Note that the scattering in this limit increases with d_n^6 . Then, the scattering from the aggregate is

$$I_{\text{agg}} = \frac{\partial \sigma_{\text{sca}}}{\partial \Omega} = N_{\text{p}}^2 \cdot S(q, R_{\text{g}}) \cdot I_{\text{agg},0}$$
(36)

where the structure factor, $S(q, R_{o})$, is defined with respect to the scattering angle, θ , via q,

$$q = \frac{4\pi}{\lambda} \sin\left(\frac{\theta}{2}\right). \tag{37}$$

The utility of q is that it can be used to describe different regimes of nanoparticle light-scattering, referred to as Q-space analysis (Sorensen, 2013). In Q-space analysis, it is convenient to combine q with the particle radius R_g , to define the dimensionless quantity qR_g , which is proportional to x_a at a given scattering angle.

When plotted against $qR_{\rm g}$ and normalized to the Rayleigh limit of an equivalent sphere, angular-resolved scattering measurements collapse onto similar curves (Fig. 16a). Fig. 16b complements the q-resolved curves with polar plots indicating the scattering as a function of scattering angle, with common points indicated on both plots. Just as the forward-scattering lobes at the right side of Fig. 16b follow circular arcs in polar coordinates, the curves in Fig. 16a are constant (independent of q) at small $qR_{\rm g}$. This regime represents the *Rayleigh regime* in q-space (the analogous Rayleigh regime in $x_{\rm a}$ -space in Fig. 15 is realized when the range of angles is constrained to small q). For fractal aggregates, some of the same features emerge as for spheres, including the q-independent Rayleigh regime and a power law regime (or generalized Porod regime), in this case with a power corresponding to the fractal dimension of the particles. For fractal aggregates more broadly, a range of structure factors have been used to capture the structure of the aggregate, depending on the regime, and are typically presented in a rotational-averaged form. Compiling the two limiting expressions for small and large $qR_{\rm g}$ yields a rough approximation (Sorensen, 2001):

$$S(q, R_{\rm g}) = \begin{cases} 1 & \text{for } qR_{\rm g} < 1, \\ (qR_{\rm g})^{-D_{\rm f}} & \text{for } qR_{\rm g} > 1. \end{cases}$$
 (38)

where R_g is the radius of gyration, which replaces R for aggregates. This variant is not used in practice in favor of more complex expressions that avoid the discontinuity at $qR_g = 1$ (Dobbins & Megaridis, 1991; Köylü et al., 1995; Lin et al., 1990; Sorensen et al., 1992b; Yang & Koylu, 2005), with a summary of some of the older methods provided by Sorensen and Wang (1999) and a more

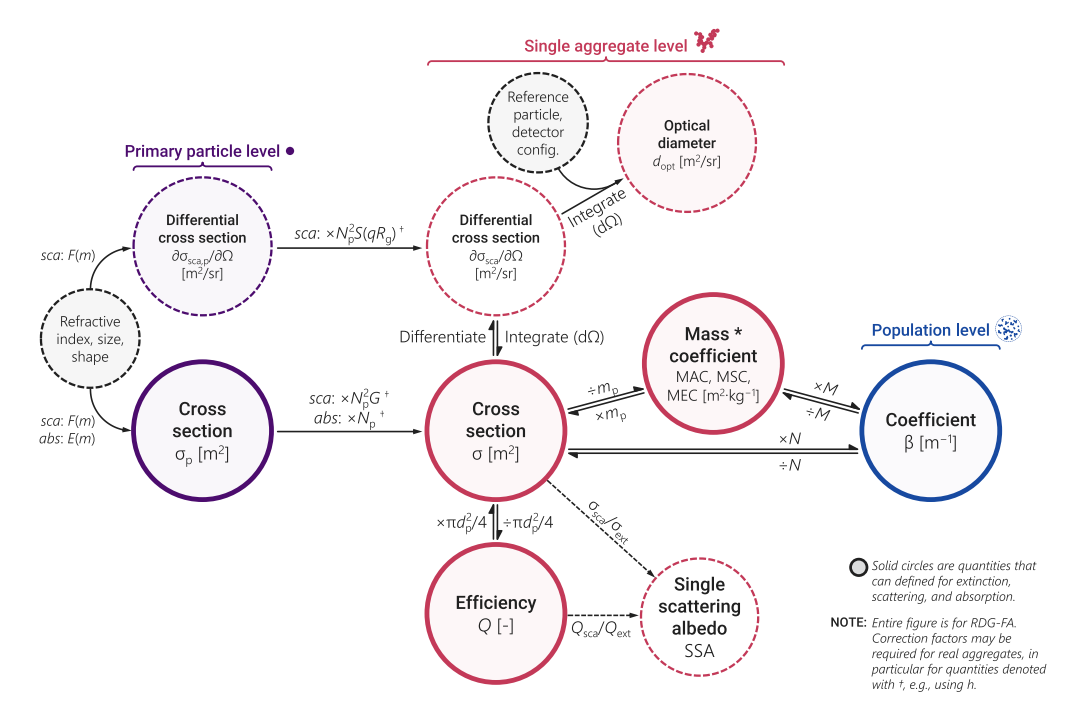


Fig. 17. Summary of the optical characteristics of single particles and particle populations and their relationships within the RDG-FA framework. In general, any of the quantities can be defined for scattering, absorption, or extinction, which are typically denoted by adding "sca", "abs", and "ext", respectively. Mass absorption coefficient (MAC), mass scattering coefficient (MSC), and single scattering albedo (SSA) do not incorporate these subscripts. SSA is unique in that it is the ratio of the scattering-to-extinction cross section. Differential cross sections are only used for scattering. The quantities N and M are the number and mass concentration of aerosol in the probe volume.

recent comparison of structure factors provided by Liu et al. (2013b). A common structure factor is that of Dobbins and Megaridis (1991):

$$S(q, R_{\rm g}) = \begin{cases} \exp\left[-\frac{(qR_{\rm g})^2}{3}\right] & \text{for } qR_{\rm g} < \sqrt{3D_{\rm f}/2} \text{ (Guinier regime),} \\ C\left(qR_{\rm g}\right)^{-D_{\rm f}} & \text{for } qR_{\rm g} > \sqrt{3D_{\rm f}/2} \text{ (Power law regime).} \end{cases}$$
(39)

where $C = \left[3D_{\rm f}/2e\right]^{D_{\rm f}/2}$ and e = 2.718... is Euler's number here. This combines the common expressions for the Guinier and power law regimes by matching their derivatives at the transition point. Figure 7 of Yon, Morán, Ouf, Mazur, and Mitchell (2021) presents theoretical realizations of the scattering phase function as the number of primary particles increases, demonstrating potential trends and providing a comparison to the Dobbins–Megaridis structure factor, Eq. (39), which demonstrates the transition to the traditional Porod regime, which trends as $\left(qR_{\rm g}\right)^{-4}$ and is relevant to small angle X-ray scattering (SAXS) described below. Real detectors will measure the scattering over some finite solid angle and/or over an ensemble of polydisperse particles, effectively averaging out resonances, if present.

When estimating the total scattering, the scattering profile is integrated over the unit sphere to give the scattering cross section, $\sigma_{\rm sca}$ (Sorensen, 2001). For ease of use, the scattering cross section is then often restated relative to the Rayleigh scattering cross section,

$$\sigma_{\text{sca,p}} = 4\pi \left[\frac{\partial \sigma_{\text{sca,p}}}{\partial \Omega} \right],\tag{40}$$

by replacing the structure factor with G,

$$\sigma_{\text{sca}} = N_{\text{p}}^2 \cdot \sigma_{\text{sca,p}} \cdot G\left(\frac{2\pi R_{\text{g}}}{\lambda}\right) = N_{\text{p}}^2 \cdot \left(\frac{\pi^4}{9} \frac{d_{\text{p}}^6}{\lambda^4} F(\mathbf{m})\right) \cdot G\left(\frac{2\pi R_{\text{g}}}{\lambda}\right)$$
(41)

where G is the form factor obtained by integrating the structure factor over a unit sphere (Chakrabarty et al., 2007). The relationship between these different optical characteristics of the particles is summarized in Fig. 17.

So far, we have used the RDG-FA model to represent fractal aggregates, but, as noted previously in Section 6.2, deviations from this model can be substantial for realistic values of primary particle diameter, wavelength, and fractal dimension A recent summary of these effects was provided by Sorensen et al. (2018), including the effects shown in Fig. 20. This highlights the difficulty of extracting information on particle characteristics when there is uncertainty in any of these parameters.

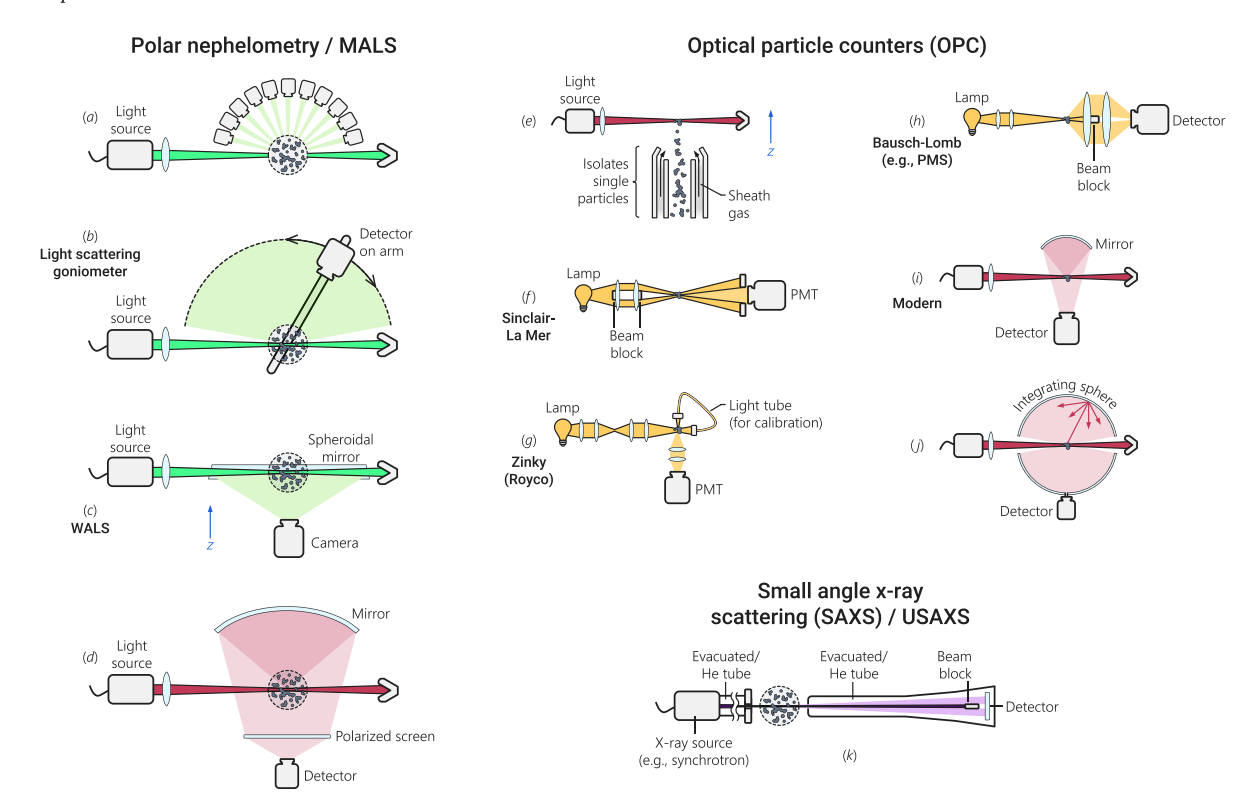


Fig. 18. A sampling of the range of optical configurations used in the measurement of light scattering from soot aggregates. (a–d) Schematics of configurations used in multiangle elastic light scattering (MALS) or polar nephelometry, including (c) the wide angle light scattering (WALS) variant of Oltmann, Reimann, and Will (2010) and (d) the setup of Zeng et al. (2023). For further configurations used for aerosols more broadly, see also Pan et al. (2022). (e–j) Schematics for OPC configurations, where single particles pass through the third axis about an angle of 90° relative to the laser direction, as per (e). Configurations roughly correspond to: (f) Sinclair-La Mer types, which is most closely aligned with Sinclair (1953), Sinclair and La Mer (1949) but represents a range of similar instruments including Gucker and Rose (1954); (g) the original Royco version adapted from Zinky (1962); (h) Bausch-Lomb types (as described in Hodkinson & Greenfield, 1965), as is still available from some manufacturers, such as Particle Measurement Systems (PMS); (i) the basic 90° configuration used in most modern OPCs; and (j) an integrating sphere variant. (k) For SAXS, the X-rays typically transmit through vacuum or helium tubes before and after passing through the sample, to minimize contributions from the background. Colors of light are representative of the typical wavelengths used in a given configuration. Partially adapted from Sipkens (2018).

6.3.2. Scattering diagnostics

Light scattering is a very common method for determining the size of aerosols, even having a set of related standards (ISO, 2020c; Xu, 2015). However, many methods do not apply to the size range relevant to soot (e.g., many covered by Black, McQuay, & Bonin, 1996; Pan et al., 2022; Tayali & Bates, 1990; Xu, 2015), which limits the range of techniques discussed here. Fundamentally, all scattering diagnostics measure the scattering phase function, Eq. (36), as illustrated in Fig. 16, integrated over some range of angles. Despite this similarity, scattering diagnostics vary significantly in terms of collection angle, detection wavelength, geometry, and analysis method. The simplest light-scattering measurement involves placing a detector to collect light over some solid angle, $\Delta\Omega$. Instruments using this technique are referred to as *nephelometers* and sometimes as *photometers*. In this configuration, these instruments cannot be used to extract size information, and a change in the particle size can dramatically affect the measurements. Integrating-sphere nephelometers measure across a large range of angles simultaneously, which is advantageous in terms of noise. These instruments suffer from truncation errors associated with the loss of scattered light in the forward and backward directions (Modini et al., 2021; Varma, Moosmüller, & Arnott, 2003) and have been designed to overlap with other optical techniques, such as cavity attenuation phase-shift (CAPS) devices (e.g., Modini et al., 2021) or cavity ring-down spectroscopy (e.g., Moosmüller et al., 2009). However, these instruments too cannot characterize particle morphology. A range of the relevant configurations for measuring particle size via light scattering are shown in Fig. 18.

6.3.3. Polar nephelometers and multi-angle elastic light scattering

Using an extension of Eq. (36), angular scattering data can theoretically be used to extract size and fractal information, a technique commonly known as multi-angle elastic light scattering (MAELS or MALS). The resulting instrument for measuring MALS is the *polar nephelometer* and can be realized in different configurations. Both early studies (e.g., Chang, Lin, & Biswas, 1995; Puri, Richardson, Santoro, & Dobbins, 1993; Santoro, Semerjian, & Dobbins, 1983; Zhang, Sorensen, Ramer, Olivier, & Merklin, 1988) and a number of more recently works (e.g., Juranyi et al., 2017; Kheirkhah, Baldelli, Kirchen, & Rogak, 2020; Martins, Kronenburg,

& Beyrau, 2021; Shao, Zhang, & Zhou, 2017) use multiple detectors fixed at several angles, which can substantially increase the cost of the instrument (given the cost of detectors) and limits the angular resolution but enables simultaneously measurements of the scattering at multiple angles. Alternatively, the laser or detector can be physically moved to different locations around the sample using a moving arm or rotating stage (e.g., Amin & Roberts, 2019; Burr, Daun, Link, Thomson, & Smallwood, 2011; Gangopadhyay, Elminyawi, & Sorensen, 1991; Köylü & Faeth, 1994; Liu, Zhang, Wang, & Zhang, 2020; Ma & Long, 2014; Sorensen, Cai, & Lu, 1992a; Yon, Morán, Lespinasse et al., 2021), as is depicted Fig. 18b. These instruments are also known as light scattering *goniometers*. This approach has a slower time response (up to minutes) and requires that the aerosol not change over the measurement duration but allows for high angular resolutions. Alternatively, scattering intensity may be imaged onto a camera sensor giving nearly continuous angular resolution (Fig. 18c–d), as in wide-angle light scattering (WALS, Huber, Altenhoff et al., 2016; Huber, Will, & Daun, 2016; Oltmann et al., 2010; Oltmann, Reimann, & Will, 2012; Palazzo, Zigan, Huber, & Will, 2020; Tsutsui, Koya, & Kato, 1998) or the miniaturized instrument of Zeng et al. (2023). Many of these measurements use blue or green light (in the range of 488–532 nm), given that particles scatter more light at these wavelengths. In all cases, the need for more detectors or moving components in polar nephelometers results in a relatively high cost relative to integrating-sphere or standard, single-angle nephelometers, which limits its use in commercial instruments.

Interpreting the measurements follows from assuming the aerosol is optically thin (no scattering between aggregates) and that the primary particles are monodisperse. Then, the total scattering signal is taken as the sum of the contributions from each of the particles, which, when invoking RDG-FA yields:

$$I(q) = NV_{\text{pr}} \cdot I_{\text{age}}$$
 (42)

where N is the number concentration and $V_{\rm pr}$ is the probe volume. Measurements at multiple angles can then be used to extract size information by exploiting trends in S(q). At a minimum, three angles would be required to simultaneously extract N, $D_{\rm f}$, and $R_{\rm g}$ but would still require calibration to account for typical $d_{\rm p}$ and would contain sizable uncertainties (e.g., Link, Snelling, Thomson, & Smallwood, 2011). The quality of the measurements will increase when measurements are made at a higher number of angles. Measurements need to extend into the power law regime, where the slope on a $\log(q)-\log(I)$ will be $-D_{\rm f}$ (Martin, Schaefer, & Hurd, 1986; Schaefer, Martin, Wiltzius, & Cannell, 1984; Sorensen, 2001; Sorensen et al., 1992a).

For polydisperse aerosols, MALS can also be used to derive size distribution information, as in Caumont-Prim, Yon, Coppalle, Ouf, and Ren (2013), Huber, Will (2016), Iyer, Litzinger, Lee, and Santoro (2007), Kheirkhah et al. (2020), Köylü (1997), Sorensen, Lu, and Cai (1995), and Link et al. (2011). Here again, one encounters an inverse problem, similar to other aerosol characterization techniques:

$$I(q) = \int_0^\infty K(q, R_g) p(R_g) dR_g, \tag{43}$$

where K is a kernel that embeds a model of particle scattering and $p(R_g)$ is the distribution of the radius of gyration, which replaces N_p via the fractal law, Eq. (1). Then, as before, the objective is to compute the distribution of the radius of gyration from angular scattering data, I(q). Whereas the inverse problem for classifiers (see Section 4.5.2) largely amounts to smearing of the true distribution, the kernel here involves a change in variable from radius of gyration to scattering intensity that makes data inversion more abstract. The incorporation of aggregate shape can also make computing the kernel challenging in all cases except when assuming RDG-FA is valid (with the limitations noted in Section 6.2). To constrain the problem, early studies assumed a lognormal distribution and inferred the distribution moments (Chang et al., 1995; Iyer et al., 2007; Köylü, 1997; Link et al., 2011; Sorensen et al., 1995), which has remained a feature in the literature (Caumont-Prim et al., 2013; Huber, Will, 2016; Kheirkhah et al., 2020; Zhang, Qi, Wang, Gao, & Ruan, 2019), particularly in cases of limited angular resolution. Burr et al. (2011) and Burr, Daun, Thomson, and Smallwood (2012) demonstrated a data inversion approach to retrieve a more detailed size distribution, adding a priori information promoting a lognormal form, rather than enforcing one.

One could also theoretically use spectrally-resolved data, which acts to similarly change q (Bouvier, Yon, Lefevre, & Grisch, 2019; Juranyi et al., 2017; Szymanski, Nagy, Czitrovszky, & Jani, 2002; Zhang, Qi, Ren, & Ruan, 2018; Zhang et al., 2019). Measurements will be convolved with potential changes in the refractive index of the material across the spectrum, which authors overcome using a hybrid approach combining spectral and angular information.

6.3.4. Optical particle sizers

The key innovation in an optical particle counter (OPC) (Gucker & Rose, 1954; Sinclair, 1953; Zinky, 1962) is that measurements take place on single particles. Otherwise, instruments share features with other nephelometers. As the particles pass through the laser beam, they cause pulses in the measured signal. This allows for the counting of particles, as it is employed in a CPC. However, the intensity of scattered light also depends very significantly on particle size, as in Eq. (34) and shown explicitly in Fig. 15. As such, larger particles will cause larger pulses, such that pulse height analyzers can be used to provide coarse size information. Detection and collection angles vary between OPCs (see also Gebhart, 1991; Hodkinson & Greenfield, 1965; Sorensen, Gebhart, O'Hern, & Rader, 2011; Szymanski, Nagy, & Czitrovszky, 2009) but often feature much wider collection angles than polar nephelometers, for signal-to-noise and angular averaging reasons (over multiple intensity lobes for spherical particles). Early configurations (Fig. 18e; Gucker & Rose, 1954; Sinclair, 1953; Sinclair & La Mer, 1949) used lamps and applied dark stops on the incident light to carve out a central region in which forward scattering is measured. Comparisons of early OPCs exist in the literature (e.g., Fitch, 1983; Liu, Berglund, & Agarwal, 1974; Whitby & Vomela, 1967), with a range of configurations. Many (if not most) modern OPCs now use red or near infrared lasers (for cost reasons, even if scattering at these wavelengths is less than shorter wavelengths) and measure scattering at

an angle of 90° relative to the laser axis using a mirror collector (see Fig. 18i). This configuration is more sensitive to small particles than other configurations, which helps in extending the lower size limit of the instrument (see Fig. 15, e.g., incorporated into the design of Gao et al., 2016a). Integrating sphere and single-particle, polar nephelometers can also be used as OPCs (e.g., Hu, Qiu, Hong, & Chen, 2021; Nakagawa et al., 2016). These provide additional constraints on the scattering phase function, allowing the retrieval of both size and refractive index for spherical particles (Moallemi et al., 2022) but not for aggregates.

A major weakness of OPCs stems from the fact that small particles scatter very small amounts of light (recall from Eq. (34) and Fig. 15 that $I_{\rm agg} \propto d_p^6$) and thus cannot be detected reliably. This places a limit on the sizes detectable by OPCs. Most OPCs have lower limits between approximately 300–500 nm, which allows them to measure larger particles, such as accumulation-mode atmospheric aerosols. Most soot particles are smaller than this. A method of partially overcoming this limitation is to use the instrument as a standard nephelometer when particles are small while also picking out individual counts of large particles (Wang et al., 2009). Today, the most sensitive OPCs are able to measure individual soot particles down to around 50 nm optical diameter, with a number of instruments extending below 150 nm (Gao et al., 2016a; Mei et al., 2020; Moore, Wiggins, Wiggins, Zimmerman et al., 2021; Tran et al., 2020; Xu, 2015).

When measuring single particles, scattering from the particles is also morphology-dependent, which is particularly complicated as the particle get larger (which is relevant to these instruments for the aforementioned reason) and one exits the Rayleigh regime, which is typical for the size range measured by OPCs. Results are also sensitive to the refractive index. These complexities are often overcome by calibrating OPCs with particles of a known size and composition, such as polystyrene latex spheres (PSL) or reference dust samples (e.g., Arizona test dust). Then, for particles of unknown shape and composition, including soot, the prescribed diameter from an OPC is an apparent optical diameter for a reference particle that scatters the same amount of light to the detector. The light scattered by aggregates is defined in Eq. (36) and can be integrated over the solid angle of the detector,

$$I_{\text{agg}} = \int_{\Omega_1}^{\Omega_2} N_{\text{p}}^2 \cdot S(q, R_{\text{g}}) \cdot \frac{\pi^4}{9} \frac{d_{\text{p}}^6}{\lambda^4} F(\mathbf{m}) \cdot d\Omega. \tag{44}$$

Note that the only angular dependence in this latter equation is the structure factor. This is to be equated to the amount of light scattered by the reference particle for the same range of solid angles. For example, for small particles (in the Rayleigh regime), the light scattered by a reference sphere is

$$I_{\text{ref}} = \left(\frac{\pi^4}{9} \frac{d_{\text{ref}}^6}{\lambda^4} F(\mathbf{m_{ref}})\right) \Delta \Omega, \tag{45}$$

where $\Delta\Omega$ is the collection solid angle of the detector and d_{ref} is the diameter of the reference particle. Equating to the aggregate scattering and solving for the corresponding diameter of reference particle that gives the same scattering:

$$d_{\text{opt}} = d_{\text{p}} N_{\text{p}}^{1/3} \cdot \left(\frac{F(\mathbf{m})}{F(\mathbf{m}_{\text{ref}})} \frac{1}{\Delta \Omega} \int_{\Omega_{1}}^{\Omega_{2}} S(q, R_{\text{g}}) \cdot d\Omega \right)^{1/6}, \tag{46}$$

which depends on aggregate morphology and optical properties. Naturally, any deficiencies in RDG-FA extend to this definition. Larger spheres are described by Mie theory, which does not have a compact form and thus prohibits such a simple representation of the optical diameter.

When comparing the performance of different instruments, it is important to note that the measurement wavelength and particle properties (refractive index and morphology) both influence the optical diameter. For example, a detection limit of 100 nm for sulfuric acid may correspond to a detection limit of 140 nm for soot at $\lambda = 1064$ nm (Howell, Freitag, Dobracki, Smirnow, & Sedlacek Iii, 2021). It is useful to note that OPCs typically measure optical diameters, while MALS targets radius of gyration. This stems from the extra information available in MALS that allows for simultaneous information about the structure of the particle, while the treatment for OPCs cannot assess morphology, instead relying on the equivalent scattering from a sphere to represent size. Assumptions of particle sphericity result in substantial uncertainties (Mishchenko, 2009). These uncertainties reduce with decreasing $x_{\rm p}$, such that that they are smallest for small particles and large λ . At shorter wavelengths, the scattering signal also oscillates as a function of particle size (related to the lobes results from Mie scattering from spheres), causing issues of uniqueness that make it challenging to accurately size particles (Fitch, 1983). Consequently, a single scattering signal may be mapped to multiple different diameters at large sizes (within about 15% of one another at $x_p > 4$, Gao et al., 2016a). To minimize uncertainties related to morphology and resonances, some OPCs use longer wavelengths to minimize x_0 . This is another driver for why many modern OPCs use visible, red lasers (e.g., He-Ne lasers at $\lambda = 655$ nm). However, high λ also require a corresponding high intensity to account for the lower scattering efficiency of all particles at lower x_p (as per Fig. 15). This can lead to undesired phenomena, including that the laser intensity required to detect soot aggregates with $d_{\rm m} \approx 100\,$ nm at $\lambda = 1064\,$ nm is sufficiently high as to cause their evaporation (Howell et al., 2021) in the same way as in single-particle laser-induced incandescence instruments (Section 6.4.3).

For more general information on OPCs, we refer the reader to Sorensen et al. (2011).

6.3.5. X-ray and neutron scattering

X-ray scattering allows for optical-like⁶ diagnostics that have been used for soot (Braun et al., 2005; Di Stasio, 2017; Di Stasio, Mitchell, LeGarrec, Biennier, & Wulff, 2006; England, 1986; Ferraro, Fratini, Rausa, Fiaschi, & Baglioni, 2016; Gardner et al., 2005;

⁶ Optical is typically reserved for the electromagnetic spectrum from the ultraviolet through the visible to the infrared.

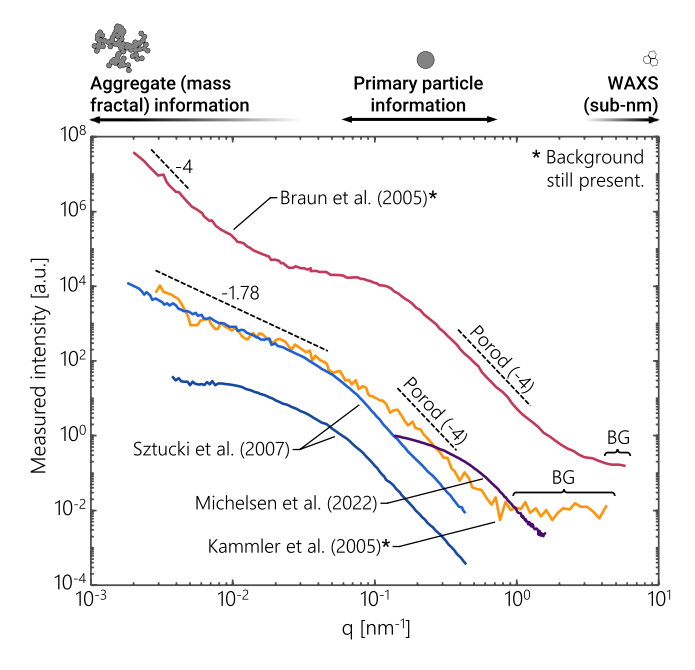


Fig. 19. A series of SAXS data digitized from a number of sources (Braun et al., 2005; Kammler et al., 2005; Michelsen, Campbell, Johansson, et al., 2022; Sztucki et al., 2007) to demonstrate the range of features observed in the scattering intensity as a function of q. Note that data from Braun et al. (2005) and Kammler et al. (2005) are shown prior to background subtraction, thus containing contributions from gases at large q. Braun et al. (2005) performs an analysis on background subtracted signals, not shown. Data from Michelsen, Campbell, Johansson, et al. (2022) corresponds to a height-above-burner of 4 mm and are truncated for high q, where the signal-to-noise ratio was poor. BG: background due to gases.

Härk & Ballauff, 2020; Hessler, Seifert, & Winans, 2002; Kammler, Beaucage, Kohls, Agashe, & Ilavsky, 2005; Loh et al., 2012; Michelsen, Campbell, Johansson, et al., 2022; Michelsen, Campbell, Tran, et al., 2022; Mitchell et al., 2009; Mitchell, Le Garrec, Florescu-Mitchell, & Di Stasio, 2006; Mitchell, LeGarrec, Saidani, Lefeuvre, & Di Stasio, 2013; Ossler, Canton, & Larsson, 2009; Ossler et al., 2013; Simmler et al., 2022; Sztucki, Narayanan, & Beaucage, 2007; Tang et al., 2019; Yon et al., 2018; Zhang et al., 2021). Many of these studies consider in-flame particles, often tracking the particles as they grow as a function of height-above-burner. The use of short wavelengths results in three significant changes. First, unlike for traditional optical scattering, the size parameter is such that measurements occur far from Rayleigh conditions, where surface scattering is dominant. Second, this causes a shift towards large q, which is countered by using small (SAXS or SAS) or ultra small angles (USAXS). Even then, most scattering measurements easily extend well into the power law regime. Finally, the refractive index is substantially different, around unity (Sorensen, 2001), given the way in which X-rays interact with matter. Otherwise, analysis is similar to MALS: looking at trends in the scattered intensity as a function of q.

SAXS is characterized by scattering intensities as a function of angles from the probing particle structure (Beaucage et al., 2004). The scattered intensity at small forward scattering angles, where $q \rightarrow 0$, remains constant and is attributed to the Rayleigh regime. The envelope of the normalized intensity curve remains constant (unity) in this regime. Small q are associated with larger features, such as aggregate-level features, overlapping in terms of the available information to traditional optical scattering. With increasing q, one can obtain primary particle information, before bridging into sub-nm features in wide angle X-ray scattering (WAXS), as is discussed later in this section. Given the presence of multiple length scales, analyses typically only plot scattering intensity as a function of q, rather than qR_g , as more than one R_g may be relevant. Each of these length scales can exhibit a corresponding Guinier (Guinier, 1939; Guinier, Fournet, & Yudowitch, 1955) knee in the scattering intensity as a function of q and a power law regime (Boldon, Laliberte, & Liu, 2015). This can include different knees for aggregates and agglomerates, if they both exist in the same population (e.g., Sztucki et al., 2007). In power law contributions, scattering is dominated by local surface geometry. The slope of this regime can indicate different geometric features (Tang et al., 2019). When locally smooth (as is common for primary particles), the scattering intensity exhibits a slope of -4 in a $\log(I)-\log(q)$ plot, a finding attributed to Porod (1951). Multi-level Beaucage functions or unified fits (Bauer, Amenitsch et al., 2019; Beaucage, 1995, 1996; Hyeon-Lee, Beaucage, Pratsinis, & Vemury, 1998) combine multiple Guinier and power law fits to simultaneously infer the fractal dimensions (from the power law regime) and primary particle size from the scattering intensity. Sample measurements are shown in Fig. 19.

Scattering from gases can limit signal-to-background at large q, often providing an upper limit to the measurements (see Fig. 19). Background subtraction can be used to extend this range and has been a significant component of many recent works (e.g., Michelsen, Campbell, Tran, et al., 2022) but is particularly challenging in flames that exhibit variations in the temperature and gaseous species over the X-ray path.

Wide-angle X-ray scattering (WAXS) simply extends the angles at which measurements are made and has also been applied to soot, often alongside SAXS (e.g., Braun et al., 2005; Ossler et al., 2009, 2013). WAXS is equivalent to X-ray diffraction (XRD) and is

only sensitive to sub-nanometer features, which are not of interest here, and requires a crystalline material. The diffraction patterns resulting from small-angle X-ray scattering (SAXS) have been analyzed in combination with in-situ, single-particle mass spectrometry (SPMS) to simultaneously image the fractal morphology and measure the composition and shape of individual soot particles (Loh et al., 2012).

While powerful, the generation of X-rays for these diagnostics requires complex facilities, such that X-ray-based techniques are practical only when the combustion source can be transported to those facilities (Kohse-Höinghaus, Barlow, Aldén, & Wolfrum, 2005). This has limited broader application in the literature.

Neutrons can be used in a similar way to probe primary particle information (Mitchell et al., 2006; Wang, Zhao, Wyslouzil, & Streletzky, 2002; Zhao, Uchikawa, & Wang, 2007), yielding small-angle neutron scattering (SANS). SANS involves longer wavelengths (0.4–3 nm) than SAXS (Michelsen, 2017), which results in a reduced spatial resolution, but features a better signal-to-background ratio, among other benefits. SANS and (ultra)SANS techniques provide a structure probing range of over four orders of magnitude in length scales from few microns down to ~1 nm, corresponding to a q-range from approximately 5×10^3 cm⁻¹ to 1×10^7 cm⁻¹. Unlike light scattering systems, the use of neutron beams eliminates the problems associated with multiple scattering (Dhaubhadel, Rieker, Chakrabarti, & Sorensen, 2012). Here too very specialized facilities are needed, limiting application of the technique.

6.3.6. Dynamic light scattering

Up to this point, the scattering has been considered static in time. Dynamics light scattering (DLS) – also known as photon (or X-ray) correlation spectroscopy (PCS), quasi-elastic light scattering (QELS), and diffusion broadening spectroscopy (DBS) – is an alternative scattering technique that has been used on soot since the 1970s (Driscoll, M. Mann, & McGregor, 1979; Penner, Bernard, & Jerskey, 1976a, 1976b). The technique is more common for particles in colloids, including soot suspensions, which are out of the scope of this work. Rather, Hinds and Reist (1972) first showed the feasibility of the technique for aerosols. Unlike static light scattering, DLS involves monitoring fluctuations in light intensity (specifically, the autocorrelation function), which is related to the motion (thus *dynamic*) of the particles and can, in turn, be related to their size. The technique is less sensitive to the optical properties of the particles, but analysis requires models relating diffusion coefficient to the particle morphology. We refer the reader to Charalampopoulos (1992) for a more detailed description of the mathematical treatment.

Arrangements are similar to those used for static light scattering but add a digital correlator to enable temporal analysis. DLS has since been used on soot to measure the evolution of size distributions and diffusion coefficients in combustion systems (Chang & Charalampopoulos, 1990; Charalampopoulos & Chang, 1988; Charalampopoulos & Felske, 1987; Dobbins & Megaridis, 1991; Flower, 1983; King, Sorensen, Lester, & Merklin, 1982, 1983; Kroner, Fuchs, Tatschl, & Glatter, 2003; Lamprecht, Eimer, & Kohse-Höinghaus, 1999; Scrivner, Taylor, Sorensen, & Merklin, 1986; Shu & Charalampopoulos, 2017; Ueyama, Ono, Matsukata, & Osima, 1993), often in-flame. Of note, Charalampopoulos and Felske (1987) and Charalampopoulos and Chang (1988) used DLS to derive optical property-independent size information, which they coupled with static light scattering to estimate the optical properties of soot. The technique has not seen much use in the last decade, likely in part because DLS cannot compete with laser-induced incandescence (see Section 6.4.3) in terms of volume fraction and particle size measurement (Lamprecht et al., 1999).

6.4. Absorption diagnostics

6.4.1. Fundamentals

To a first approximation, the total light absorbed by a collection of soot particles is equal to the sum of absorption by the primary particles comprising each aggregate. Thus, light absorption is often used as a proxy measurement of particulate mass (or volume fraction). This proxy is predicted by RDG-FA theory, but remains generally valid even when relaxing the assumptions of RDG-FA, and does not require detailed *a priori* knowledge of the aggregate properties (Chakrabarty et al., 2007; Radney et al., 2014).

The light absorption of each primary particle is volumetric and may be described in terms of its absorption cross-section,

$$\sigma_{\text{abs,p}} = \frac{\pi^2 d_{\text{p}}^3}{\lambda} E(\mathbf{m}),\tag{47}$$

where

$$E(\mathbf{m}) = \operatorname{Im}\left(\frac{\mathbf{m}^2 - 1}{\mathbf{m}^2 + 2}\right) \tag{48}$$

is the absorption function, which incorporates the refractive index. The absorption cross-section of an entire aggregate (assuming identical primary particles) is then

$$\sigma_{\rm abs} = N_{\rm p} \cdot \sigma_{\rm abs,p},\tag{49}$$

and the absorption measured for an entire population of aggregates, the absorption coefficient, is

$$\beta_{\rm abs} = N_{\rm a} \cdot \sigma_{\rm abs},$$
(50)

where N_a is the number density of aggregates, rather than the number density of primary particles (N_p). Fig. 15 illustrates the variations in absorption of particles across size regimes, considering both fractal soot (by RDG-FA) and spheres (by Mie theory).

The absorption cross-section and coefficient are the basic intensive and extensive measures of nanoparticle absorption. Depending on the context, or for convenience, other properties are also defined and used, as identified in Fig. 17. Two of the essential properties

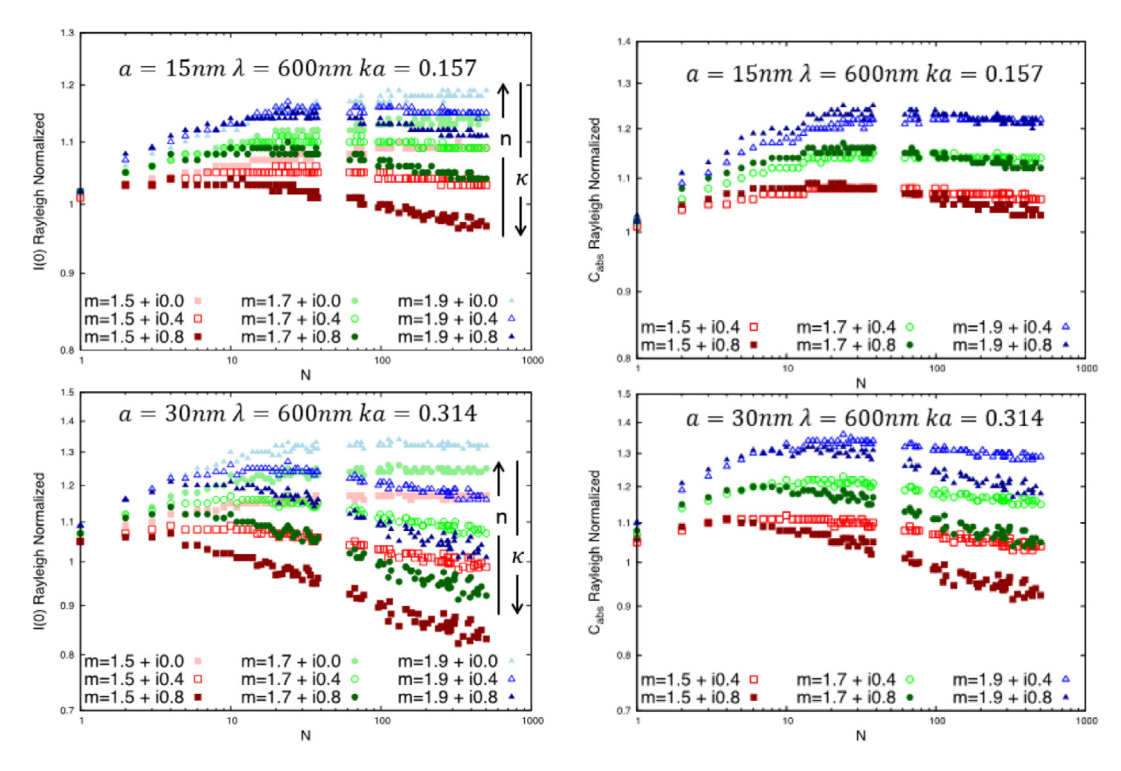


Fig. 20. Ratios of the forward scattering (left panels) and absorptive properties (right panels) of soot aggregates (predicted by detailed DLCA modeling) to their respective Rayleigh-normalized properties (which for absorption is representative of RDG-FA theory). Figure adapted from Sorensen et al. (2018), with eventual permission.

for absorption are the absorption Ångström exponent (AAE) and the mass absorption cross section (MAC). The AAE quantifies the wavelength-dependence of absorption (a dimension that is not shown in Fig. 17 for simplicity). The AAE is the slope of a plot of σ_{abs} (or a related quantity, such as the absorption coefficient, β_{abs}) against λ , multiplied by -1, such that

$$\frac{\sigma_{\text{abs}}(\lambda_1)}{\sigma_{\text{abs}}(\lambda_2)} = \left(\frac{\lambda_1}{\lambda_2}\right)^{-\text{AAE}} \tag{51}$$

The MAC is the ratio of absorption cross section to the particle mass,

$$MAC = \frac{\sigma_{abs}}{m_{p}} = \frac{\beta_{abs}}{M},$$
(52)

More often this is computed using two measurable quantities: the mass concentration, M, and absorption coefficient of a population of particles, β_{abs} . It is useful to observe that the MAC may also be defined on a single-particle basis (σ_{abs}/m_p), although current measurement techniques are not sensitive enough to measure σ_{abs} directly. As both the particle mass and σ_{abs} vary with d_p^3 , MAC becomes independent of particle size, to the extent that RDG-FA holds. It is important to clarify that the MAC is fundamentally a measured quantity. In terms of particle morphology, these measurements can then be used to inform on the optical properties of the particles. The accuracy of theoretical RDG-FA predictions of MAC has often been evaluated in the literature in terms of a correction factor, h,

$$h = \frac{\text{MAC}}{\text{MAC}_{\text{RDG}}} = \frac{6\pi E(m)}{\lambda \rho_m \text{MAC}_{\text{RDG}}}$$
 (53)

where MAC is a measured MAC and MAC_{RDG} is the theoretical equivalent predicted by RDG-FA. The correction is normally less than 50%, typically 0.9 < h < 1.3 for reasonable estimates of the soot refractive index (see Fig. 20 and Sorensen et al., 2018). The precise value depends on aggregate size, $N_{\rm p}$, and $d_{\rm p}$, in addition to $D_{\rm f}$, $k_{\rm f}$, λ , and m (Sorensen et al., 2018). Farias, Köylü, and Carvalho (1996) provide convenient maps of h for various $x_{\rm p}$ and m. Some recent studies have proposed avoiding the use of h by representing the abovementioned complex complete models with computationally-efficient, machine-learning-based models (Luo, Zhang, Wang, Wang, & Zhang, 2018; Talebi-Moghaddam et al., 2020; Xu, He, Zhao, Mao, & Fu, 2021), though these models are yet to see wider adoption.

6.4.2. Absorption diagnostics

A number of techniques capable of measuring soot-aggregate light absorption have been reviewed in detail previously (Giechaskiel et al., 2014a; Lack et al., 2014; Moosmüller et al., 2009). Most of these techniques focus on measuring the light absorption of

an ensemble of aerosol particles, as current technology can only detect light absorption for single particles of at least a micron in diameter (Cremer, Covert, Parmentier, & Signorell, 2017; Diveky, Roy, David, Cremer, & Signorell, 2020), which is an order of magnitude larger than typical soot aggregates. Most direct techniques for measuring ensemble light absorption target particle volume or mass fractions in an aerosol stream. Examples include (Lack et al., 2014): the extinction-minus-scattering technique (EMS), which suffers from very high uncertainties when an aerosol contains more non-absorbing than absorbing particles (Modini et al., 2021); photoacoustic spectroscopy (PAS); and photothermal interferometry (PTI). Both the EMS technique and PAS have been used as reference absorption measurements (Sheridan et al., 2005) and can be miniaturized (Breitegger, Schriefl, Nishida, Hochgreb, & Bergmann, 2019). While PTI has recently been proposed as superior (Drinovec et al., 2022), due to its lack of a photoacoustic resonator, the technique is cross-sensitive to gas turbulence (Lack et al., 2014). These techniques are supplemented by filter-based instruments, which load soot particles onto non-absorbing fiber filters and measure the resulting change in either transmission (filter photometers including aethalometers; Lack et al. 2014, Moosmüller et al. 2009) or reflectance (in devices known as smoke meters, spot meters, or reflectometers). Reflectance measurements using smoke meters are a well-established method for estimating soot concentrations in hot, undiluted engine emissions, (Giechaskiel et al., 2014a; ISO, 2000) and are used to estimate soot mass concentrations based on empirical correlation functions (ISO, 2000, Annex C) down to about 25 µg m³ (Giechaskiel et al., 2014a). When this high limit of detection is not an issue, smoke meters are valuable for the robustness afforded by their simplicity of construction.

Similarly, filter photometers provide practical sensing of atmospheric levels of BC, with sensitivity down to the ng/m³ level achieved for commercial devices. These devices estimate light absorption from a measurement of light attenuation (i.e., reduction in light intensity due to transmission through the filter) based on empirical calibration. Although they are highly sensitive, these instruments are best deployed in contexts where the soot mixing state does not vary: the empirical calibration may vary by up to 50% for samples where soot is internally or externally mixed with non-absorbing materials (Collaud Coen et al., 2010). This uncertainty is largely driven by the fact that scattering also influences attenuation of light by the filter, which can be reduced by measuring this light scattering either using a co-located nephelometer (Collaud Coen et al., 2010) or dedicated scattering detectors within the instrument (Petzold & Schönlinner, 2004). The latter approach has been developed into both real-time and offline (Massabò et al., 2013) diagnostics. Although less accurate than more sophisticated techniques, filter photometers perform well for certain samples (Corbin, Schripp et al., 2022). The simplicity of filter photometers has allowed their use in global atmospheric monitoring stations (Laj et al., 2020) as well as portable low-cost sensors (Kousis, Manni, & Pisello, 2022).

While these examples constitute the dominant use of absorption diagnostics, such instruments are of less interest in this work, given that they cannot assess particle morphology. Rather, absorption-based diagnostics for particle morphology rely on secondary phenomena, which occur after light absorption.

6.4.3. Laser-induced incandescence (LII)

First observed for alumina particles (Weeks & Duley, 1974), LII has been shown to be a powerful diagnostic that is indirectly related to the optical theory discussed above (Geigle et al., 2022; Michelsen et al., 2015; Schulz et al., 2006; Sipkens, Menser et al., 2022). Particles are irradiated with light, absorbing a sufficient amount to be heated to incandescent temperatures, on the order of 3000 K. The refractive index of soot means that the particles readily absorb incident light and emit incandescence. Particles emit roughly volumetrically (under the RDG-FA approximation), such that the measured incandescence is proportional to the particle volume fraction, providing yet another route to measure this quantity. There are two general categories of LII.

Pulsed and time-resolved lii. Pulsed LII involves heating the particles using a short (typically around 5 ns), high fluence (relative to the other diagnostics presented here) laser pulse. Following the laser pulse, the particles can be monitored as they cool. The incandescence is measured at multiple wavelengths, which allows the practitioner to monitor the particle temperature during cooling using pyrometry, yielding time-resolved laser-induced incandescence (TiRe-LII). Implementations range from two wavelengths, that is two-color or, equivalently, auto-compensating LII (De Iuliis, Cignoli, & Zizak, 2005; Smallwood et al., 2002; Snelling, Smallwood, Liu, Gülder, & Bachalo, 2005) to full spectra using a streak camera (Block, Oppermann, & Budack, 2000; Charwath, Suntz, & Bockhorn, 2006; Ikezawa, Wakamatsu, Zimin, Pawlat, & Ueda, 2011; Menser, Daun, Dreier, & Schulz, 2016; Michelsen, 2006). Heat transfer models are used to compute particle size from the incandescence decay. Cooling is roughly proportional to the surface area of the particles (Michelsen et al., 2007), though, the heat transfer is more often connected to the primary particle diameter (i.e., via $\pi d_p^2/4$). Shielding can interrupt this direct relationship (Bladh et al., 2011; Daun, 2010; Filippov, Zurita, & Rosner, 2000; Johnsson, Bladh, Olofsson, & Bengtsson, 2013; Liu, Yang, Hill, Snelling, & Smallwood, 2006). Given that pulsed LII is typically applied to an ensemble of particles, the derived primary particle size is an averaged value, roughly aligned with the Sauter mean diameter due to the nature of the heat transfer processes (Liu et al., 2006; Sipkens et al., 2014). Pulsed LII instruments are often custom-built, though a commercial instrument is available (LII 300, Artium).

Interpretation of signals requires knowledge of both the optical and thermal properties of the particles (Michelsen et al., 2007, 2015), in addition to the properties of the surrounding gas (given conduction from the particle to the gas phase). Collectively, uncertainties in these quantities (including which heat transfer modes are relevant) limit precision (Bauer, Daun et al., 2019). Sophisticated models may improve fits to the temperature decay but introduce more uncertainties via an expanding number of poorly-characterized parameters (e.g., annealing rates of soot). In fact, uncertainties associated with the range of model parameters can be an order-of-magnitude larger than other uncertainties (Sipkens, Menser et al., 2022; Sipkens, Singh, & Daun, 2017), expanding from around 1.5% to around 30%. This can be partially resolved by combining TiRe-LII with MALS (Bauer, Daun et al., 2019). Work continues on better understanding, quantifying, and reducing these uncertainties for soot.

Single-particle, continuous wave lii. By contrast, single-particle, continuous wave LII (CW-LII) involves isolating single particles to provide information on refractory mass of each particle. The technique employs a lower fluence (relative to the pulsed case) CW laser, which is used to fully vaporize the particles over longer periods. Since its development by Stephens, Turner, and Sandberg (2003), single-particle LII has generally been accomplished with a commercial instrument, the Single-Particle Soot Photometer (SP2). In the SP2, soot particles are passed through an Nd:YAG intra-cavity laser where they incandesce. The incandescence is measured by avalanche photomultiplier tubes. The peak signal height is linearly proportional to the mass of the particle, and the incandescence signal can be calibrated by measuring soot particles of known mass. For instance, an SP2 can be calibrated with a PMA or similar using particles of known chemical composition (ideally, thermally denuded soot from the same source to be measured) to determine the relationship between incandescent signal and particle mass (Gysel, Laborde, Olfert, Subramanian, & Gröhn, 2011; Irwin et al., 2013). PMAs can also be combined with the SP2 to assess the mixing state of soot (see Section 5.3). One limitation of the SP2 is that the lower detection limit is near 0.1 fg, and often a large number of particles from combustion sources have particle masses lower than the limit (Liggio et al., 2012, see also see Fig. 6). Nevertheless, the SP2 can normally resolve the median mass of most soot populations (Pileci et al., 2021).

The SP2 also contains scattering detectors, which, given that measurements are made on single particles, means that it is both an LII instrument and an OPC. For particles which do not significantly absorb 1064 nm light, this OPC measures sizes down to approximately 150 nm. However, particles containing material that does absorb 1064 nm light (including soot, iron, and tarballs, Corbin & Gysel-Beer, 2019; Moteki et al., 2017; Schwarz et al., 2006; Sedlacek et al., 2018; Stephens et al., 2003) will change in size during transit through the SP2 intracavity laser beam, complicating their scattering-based sizing. In most samples, this size change reflects the evaporation of any internally mixed, volatile material (e.g. Gao et al., 2007), but it may also represent the evaporation of part of a homogeneous tarball (Corbin & Gysel-Beer, 2019) or the initial swelling of soot aggregates prior to their vaporization (Bambha & Michelsen, 2015). We note that the same company which produces the SP2 produces a commercial OPC, the ultra-high sensitivity aerosol spectrometer (UHSAS), which is similar to the SP2 OPC. Studies on the UHSAS may provide some insights into particle behavior in the SP2 OPC (Howell et al., 2021; Kupc, Williamson, Wagner, Richardson, & Brock, 2018; Moore, Wiggins, Wiggins, Ahern et al., 2021), although light-scattering signals in the SP2 are typically analyzed in a time-resolved manner to account for evaporation (e.g. Gao et al., 2007; Laborde et al., 2012; Moteki & Kondo, 2007; Taylor et al., 2015). This approach does not change the fact that only larger soot aggregates scatter enough light to be detected by an OPC.

6.5. Outlook

The simultaneous use of multiple optical diagnostics is becoming increasingly prevalent and important to soot characterization. For LII, the addition of a photometric detector allows simultaneous optical sizing (Stephens et al., 2003), which has led to complex data analysis procedures (e.g., Gao et al., 2007). Extinction measurements are also combined with LII to reduce the uncertainties associated with the optical properties of soot. LII has been combined with simple single angle scattering to compute a crude volume-equivalent diameter (Will, Schraml, & Leipert, 1996). LII has also been combined with MALS to assess volume fractions (e.g., Geitlinger, Streibel, Suntz, & Bockhorn, 1999; Ochoterena, Andersson, & Andersson, 2020; Palazzo et al., 2019), changes to maturity (Olofsson, Johnsson, Bladh, & Bengtsson, 2013; Olofsson, Simonsson, Török, Bladh, & Bengtsson, 2015), mass loss during laser heating (Török et al., 2022), and, more important to this work, simultaneous estimates of both primary particle and aggregate size (Bauer, Daun et al., 2019; Crosland, Thomson, & Johnson, 2013; Huber, Altenhoff et al., 2016; Reimann, Kuhlmann, & Will, 2009; Snelling, Link, Thomson, & Smallwood, 2011; Will et al., 1996). Indeed, given the minimal increase in necessary equipment, this latter use-case could continue see growth in the coming years, thereby reducing uncertainties overall, e.g., using data fusion. You et al. (2018) also performed SAXS in addition to LII and MALS, which provided overlapping information in terms of aggregate and primary particle size. The commercial SP2 instrument does measure both LII and scattering, though with a CW laser rather than a pulsed one, limiting primary particle information, typically requiring a classifier to add size information. Recent work has also aimed to use scattering profiles to characterize particles of different types, including using such a technique to distinguish soot from other types of particles (Geisler, Larsen, Dirscherl, & Jensen, 2022).

Across these different instances, optical diagnostics for morphology are more often applied *is situ*, rather than downstream of instruments. Overall, despite the power of these diagnostics, the complicated relationships between optical measurements and particle morphology results in relatively high uncertainties. Even so, with increases in computing power and declining hardware costs and more powerful light sources (e.g., improvements to LEDs), the use of these diagnostics will become more accessible and powerful and, thereby, better supplement other particle diagnostics.

Optical diagnostics are also increasingly used to obtain high dimensional information about particle size in flames, including 2D MALS (Altenhoff, Aßmann, Perlitz, Huber, & Will, 2019; Ma & Long, 2014; Martins et al., 2021) and 3D LII (Bauer, Yu, Cai, Huber, & Will, 2021; Halls et al., 2017; Meyer et al., 2016). The number of wavelengths used in LII has increased, in attempts to avoid artifacts in signals.

Optical diagnostics also form the basis for many low-cost sensors. Currently, relatively few devices are capable of measuring ultrafine particles, the category relevant to these particles. However, this is starting to change, and we are likely to see substantial growth in using optical diagnostics to construct low-cost sensors for relevant sizes.

7. Conclusions

The characterization of combustion-generated aggregates has evolved steadily over the last 40 years, with important advances in instrumentation as well as the models used to interpret measurements. Although the fractal model remains useful, it is important to recognize that primary particles overlap, vary in size, and vary significantly from one aggregate to another, even from the same combustion source. Increases in computing power make it possible to simulate the processes that control these details. However, the effects of oxidation, fragmentation, and the spatial non-uniformity of conditions on soot morphology are not well understood, and are potential areas for future research. Capturing a corresponding level of detail using microscopy is becoming easier using current image processing methods (see Section 3). For example, it is now possible to analyze structures of hundreds or thousands of particles from an experiment, yielding patterns in populations not at all apparent from single images. Another new frontier may be in the use of tomographic reconstruction of complete 3D structures. More accurate structural models will allow researchers to make stronger inferences from online aerosol measurements.

Aerosol classifiers are now widely available. These classifiers offer particle separation according to different physical properties for particles the size of soot. Recent work has provided a precise understanding of their instrument transfer functions, making it possible to use two different types of classifiers in tandem to determine upstream concentrations as a function of two independent dimensions, such as mass and mobility. These classifiers have also been combined with novel downstream detectors, such as single-particle laser-induced incandescence instruments. This enables researchers to identify internal and external mixtures of particle types, as well as particles of different morphologies. Increases in computing power have facilitated the use of advanced inversion approaches for multiple classifier experiments. At the same time, decreasing hardware costs and low cost sensors that can provide coarse size information are making these kinds of measurements more widespread and accessible.

Optical measurements allow rapid measurements, sometimes inside flames or engines, or at large distances. However, interpretation of the raw measurements invariably requires sophisticated modeling if information on particle morphology is desired, introducing a range of uncertainties. The models used in data interpretation depend on knowledge of the material complex refractive index and morphology. Fortunately, particle morphology can be more tightly constrained, given the developments mentioned above, and in parallel, uncertainties in complex refractive index for various forms of soot is also lessening. Scattering can inform on the particle morphology either by measuring the amount scattered by single particles (OPCs) or by measuring the scattering at multiple angles (MALS). The former technique has only recently been extended into the size range relevant to soot and work is still required to make the measurements robust for this application. MALS, by contrast, has been demonstrated for determining the radius of gyration and fractal dimension of soot, even if configurations are more complex than in OPCs. For absorption, LII provides size information indirectly, using emission phenomena after particle absorption. TiRe-LII measures a heat transfer surface area, which is often related to the primary particle diameter, though with uncertainties stemming from the optical *and* thermal properties of soot. The complimentary information from MALS and TiRe-LII is a particularly powerful combination, even if uncertainties remain in interpreting both measurements.

With all of these approaches to characterizing morphology, the possibility exists to resolve small changes in mass, size and, morphology, thereby making these techniques powerful. At the same time, subtle differences in instrument setup and processing can introduce substantial biases in the measurements of absolute quantities of, say, fractal dimension or effective density, which make precise interlaboratory comparisons extremely challenging (yet all the more important as a future area of research). None of the broad approaches (microscopy, classifiers with inversion, optical diagnostics) can unambiguously resolve all features of a soot aerosol, but these approaches are complementary and thus most comprehensive studies of soot will use at least two of these approaches. This is the major motivation for presenting these diverse approaches in a single review.

Here we have reviewed developments that are well-known to researchers working on the morphology of soot. We have aimed to provide a consistent framework for the issues that will be useful to research students starting in the field or to established researchers in neighboring fields wishing to delve more deeply into the physical characteristics of solid combustion aerosols and in particular, soot.

As diagnostics for soot continue to expand, the community also continues to adapt towards characterizing carbonaceous particles of more diverse morphologies, e.g., including ash, tarballs, collapsed soot, and brown carbon. This includes overcoming the limits of existing instruments, to further suppress emissions in sectors that remain difficult to electrify (e.g., aviation emissions). Meanwhile, as emissions regulations become more stringent, there is a need to characterize lower concentrations and smaller particles, driving down lower detectability limits of some techniques. Lessons learned on carbonaceous particles continue to see uses in engineered nanoparticle production and characterization as the field continues to grow.

Declaration of competing interest

The authors declare that they have no known competing financial interests or personal relationships that could have appeared to influence the work reported in this paper.

Data availability

Data will be made available on request

Acknowledgments

The authors would like to acknowledge the contributions of Jérôme Yon, José Morán, Georgios Kelesidis, and Hamed Nikookar for contributing simulated aggregates to Fig. 2. We also give special thanks to Cyprien Jourdain for generating the simulated aggregates used in both in Fig. 2 and in other figures that show renderings of simulated aggregates in this work (Jourdain et al., 2023).

We wish to thank Fengshan Liu for comments on the discussion of optical techniques.

- A. M. Boies and S. Rogak acknowledge the support of The Royal Society International Exchanges 2020 Round 1:IESR1201300 to facilitate travel and discussion related to this paper.
- R. K. Chakrabarty acknowledges the generous support of the US National Science Foundation (AGS-1926817), Department of Energy (DE-SC0021011), and NASA, United States (NNH20ZDA001N).
- T. A. Sipkens and J. C. Corbin also acknowledge the support of the Small Teams Initiative of the National Research Council Canada.

References

- Adachi, K., Chung, S. H., Friedrich, H., & Buseck, P. R. (2007). Fractal parameters of individual soot particles determined using electron tomography: Implications for optical properties. *Journal of Geophysical Research: Atmospheres*, 112(D14), http://dx.doi.org/10.1029/2006JD008296.
- Afroughi, M. J., Falahati, F., Kostiuk, L. W., & Olfert, J. S. (2019). Properties of carbon black produced by the thermal decomposition of methane in the products of premixed flames. *Journal of Aerosol Science*, 131, 13–27. http://dx.doi.org/10.1016/j.jaerosci.2019.02.002.
- Agarwal, J. K., & Sem, G. J. (1980). Continuous flow, single-particle-counting condensation nucleus counter. *Journal of Aerosol Science*, 11(4), 343–357. http://dx.doi.org/10.1016/0021-8502(80)90042-7.
- Ahlvik, P., Ntziachristos, L., Keskinen, J., & Virtanen, A. (1998). Real time measurements of diesel particle size distribution with an electrical low pressure impactor. SAE Transactions, 95–113. http://dx.doi.org/10.4271/980410.
- Ait Ali Yahia, L., Gehin, E., & Sagot, B. (2017). Application of the thermophoretic annular precipitator (TRAP) for the study of soot aggregates morphological influence on their thermophoretic behaviour. *Journal of Aerosol Science*, 113, 40–51. http://dx.doi.org/10.1016/j.jaerosci.2017.07.018.
- Aizawa, T., Nishigai, H., Kondo, K., Yamaguchi, T., Nerva, J. G., Genzale, C., et al. (2012). Transmission electron microscopy of soot particles directly sampled in diesel spray flame A comparison between US#2 and biodiesel soot. SAE International Journal of Fuels and Lubricants, 5(2), 665–673. http://dx.doi.org/10.4271/2012-01-0695.
- Al Zaitone, B., Schmid, H. J., & Peukert, W. (2009). Simulation of structure and mobility of aggregates formed by simultaneous coagulation, sintering and surface growth. *Journal of Aerosol Science*, 40(11), 950–964. http://dx.doi.org/10.1016/j.jaerosci.2009.08.007.
- Allen, M., & Raabe, O. (1982). Re-evaluation of millikan's oil drop data for the motion of small particles in air. Journal of Aerosol Science, 13(6), 537–547. http://dx.doi.org/10.1016/0021-8502(82)90019-2.
- Allen, M. D., & Raabe, O. G. (1985). Slip correction measurements of spherical solid aerosol particles in an improved millikan apparatus. Aerosol Science and Technology, 4(3), 269–286. http://dx.doi.org/10.1080/02786828508959055.
- Altenhoff, M., Aßmann, S., Perlitz, J. F., Huber, F. J., & Will, S. (2019). Soot aggregate sizing in an extended premixed flame by high-resolution two-dimensional multi-angle light scattering (2D-MALS). Applied Physics B, 125, 1–15. http://dx.doi.org/10.1007/s00340-019-7282-0.
- Altenhoff, M., Aßmann, S., Teige, C., Huber, F. J., & Will, S. (2020). An optimized evaluation strategy for a comprehensive morphological soot nanoparticle aggregate characterization by electron microscopy. *Journal of Aerosol Science*, 139, Article 105470. http://dx.doi.org/10.1016/j.jaerosci.2019.105470.
- Amin, H. M., & Roberts, W. L. (2019). An experimental apparatus to measure soot morphology at high pressures using multi-angle light scattering. *Measurement Science & Technology*, 30(7), Article 075902. http://dx.doi.org/10.1088/1361-6501/ablc3f.
- Anderson, P. M., Guo, H., & Sunderland, P. B. (2017). Repeatability and reproducibility of TEM soot primary particle size measurements and comparison of automated methods. *Journal of Aerosol Science*, 114, 317–326. http://dx.doi.org/10.1016/j.jaerosci.2017.10.002.
- Appel, J., Bockhorn, H., & Frenklach, M. (2000). Kinetic modeling of soot formation with detailed chemistry and physics: Laminar premixed flames of C2 hydrocarbons. Combustion and Flame, 121(1), 122–136. http://dx.doi.org/10.1016/S0010-2180(99)00135-2.
- Arganda-Carreras, I., Kaynig, V., Rueden, C., Eliceiri, K. W., Schindelin, J., Cardona, A., et al. (2017). Trainable Weka Segmentation: A machine learning tool for microscopy pixel classification. *Bioinformatics*, 33(15), 2424–2426. http://dx.doi.org/10.1093/bioinformatics/btx180.
- Arias, P., Bellouin, N., Coppola, E., Jones, R., Krinner, G., Marotzke, J., et al. (2021). Technical summary. In V. Masson-Delmotte, P. Zhai, A. Pirani, S. Connors, C. Péan, S. Berger, N. Caud, Y. Chen, L. Goldfarb, M. Gomis, M. Huang, K. Leitzell, E. Lonnoy, J. Matthews, T. Maycock, T. Waterfield, O. Yelekçi, R. Yu, B. Zhou (Eds.), Climate change 2021: The physical science basis. Contribution of working group I to the sixth assessment report of the intergovernmental panel on climate change (pp. 33–144). Cambridge, United Kingdom and New York, NY, USA: Cambridge University Press, http://dx.doi.org/10.1017/9781009157896.002.
- Asbach, C., Fissan, H., Stahlmecke, B., Kuhlbusch, T. A., & Pui, D. Y. (2009). Conceptual limitations and extensions of lung-deposited Nanoparticle Surface Area Monitor (NSAM). *Journal of Nanoparticle Research*, 11(1), 101–109. http://dx.doi.org/10.1007/s11051-008-9479-8.
- Ault, A. P., & Axson, J. L. (2017). Atmospheric aerosol chemistry: Spectroscopic and microscopic advances. *Analytical Chemistry*, 89(1), 430–452. http://dx.doi.org/10.1021/acs.analchem.6b04670.
- Baker, T. J., Tyler, C. R., & Galloway, T. S. (2014). Impacts of metal and metal oxide nanoparticles on marine organisms. *Environmental Pollution*, 186, 257–271. http://dx.doi.org/10.1016/j.envpol.2013.11.014.
- Baldelli, A., & Rogak, S. (2019). Morphology and Raman spectra of aerodynamically classified soot samples. Atmospheric Measurement Techniques, 12(8), 4339–4346. http://dx.doi.org/10.5194/amt-12-4339-2019.
- Baldelli, A., Trivanovic, U., & Rogak, S. N. (2019). Electron tomography of soot for validation of 2D image processing and observation of new structural features. Aerosol Science and Technology, 53(5), 575–582. http://dx.doi.org/10.1080/02786826.2019.1578860.
- Baldelli, A., Trivanovic, U., Sipkens, T. A., & Rogak, S. N. (2020). On determining soot maturity: A review of the role of microscopy-and spectroscopy-based techniques. *Chemosphere*, 252, Article 126532. http://dx.doi.org/10.1016/j.chemosphere.2020.126532.
- Bambha, R. P., & Michelsen, H. A. (2015). Effects of aggregate morphology and size on laser-induced incandescence and scattering from black carbon (mature soot). *Journal of Aerosol Science*, 88, 159–181. http://dx.doi.org/10.1016/j.jaerosci.2015.06.006.
- Bardestani, R., Patience, G. S., & Kaliaguine, S. (2019). Experimental methods in chemical engineering: specific surface area and pore size distribution measurements—BET, BJH, and DFT. *The Canadian Journal of Chemical Engineering*, 97(11), 2781–2791. http://dx.doi.org/10.1002/CJCE.23632.
- Bau, S., Zimmermann, B., Payet, R., & Witschger, O. (2015). A laboratory study of the performance of the handheld diffusion size classifier (DiSCmini) for various aerosols in the 15-400 nm range. Environmental Sciences: Processes and Impacts, 17(2), 261–269. http://dx.doi.org/10.1039/c4em00491d.
- Bauer, P. S., Amenitsch, H., Baumgartner, B., Köberl, G., Rentenberger, C., & Winkler, P. (2019). In-situ aerosol nanoparticle characterization by small angle X-ray scattering at ultra-low volume fraction. *Nature Communications*, 10(1), 1122. http://dx.doi.org/10.1038/s41467-019-09066-4.

- Bauer, F. J., Daun, K. J., Huber, F. J., & Will, S. (2019). Can soot primary particle size distributions be determined using laser-induced incandescence? *Applied Physics B*, 125, 1–15. http://dx.doi.org/10.1007/s00340-019-7219-7.
- Bauer, F. J., Yu, T., Cai, W., Huber, F. J., & Will, S. (2021). Three-dimensional particle size determination in a laminar diffusion flame by tomographic laser-induced incandescence. *Applied Physics B*, 127, 1–10. http://dx.doi.org/10.1007/s00340-020-07562-w.
- Beaucage, G. (1995). Approximations leading to a unified exponential/power-law approach to small-angle scattering. *Journal of Applied Crystallography*, 28(6), 717–728. http://dx.doi.org/10.1107/S0021889895005292.
- Beaucage, G. (1996). Small-angle scattering from polymeric mass fractals of arbitrary mass-fractal dimension. *Journal of Applied Crystallography*, 29(2), 134–146. http://dx.doi.org/10.1107/S0021889895011605.
- Beaucage, G., Kammler, H. K., Mueller, R., Strobel, R., Agashe, N., Pratsinis, S. E., et al. (2004). Probing the dynamics of nanoparticle growth in a flame using synchrotron radiation. *Nature Materials*, 3(6), 370–373. http://dx.doi.org/10.1038/nmat1135.
- Beeler, P., & Chakrabarty, R. K. (2022). Constraining the particle-scale diversity of black carbon light absorption using a unified framework. Atmospheric Chemistry and Physics, 22(22), 14825–14836.
- Beranek, J., Imre, D., & Zelenyuk, A. (2012). Real-time shape-based particle separation and detailed in situ particle shape characterization. *Analytical Chemistry*, 84(3), 1459–1465. http://dx.doi.org/10.1021/ac202235z.
- Berner, A., Reischl, G., & Puxbaum, H. (1984). Size distribution of traffic derived aerosols. Science of the Total Environment, 36, 299–303. http://dx.doi.org/10.1016/0048-9697(84)90280-8.
- Bescond, A., Yon, J., Ouf, F., Ferry, D., Delhaye, D., Gaffié, D., et al. (2014). Automated determination of aggregate primary particle size distribution by TEM image analysis: Application to soot. Aerosol Science and Technology, 48(8), 831–841. http://dx.doi.org/10.1080/02786826.2014.932896.
- Birch, M. E., & Cary, R. A. (1996). Elemental carbon-based method for monitoring occupational exposures to particulate diesel exhaust. *Aerosol Science and Technology*, 25(3), 221–241. http://dx.doi.org/10.1080/02786829608965393.
- Black, D. L., McQuay, M. Q., & Bonin, M. P. (1996). Laser-based techniques for particle-size measurement: A review of sizing methods and their industrial applications. *Progress in Energy and Combustion Science*, 22(3), 267–306. http://dx.doi.org/10.1016/S0360-1285(96)00008-1.
- Bladh, H., Johnsson, J., Rissler, J., Abdulhamid, H., Olofsson, N. E., Sanati, M., et al. (2011). Influence of soot particle aggregation on time-resolved laser-induced incandescence signals. *Applied Physics B*, 104, 331–341. http://dx.doi.org/10.1007/s00340-011-4470-y.
- Block, B., Oppermann, W., & Budack, R. (2000). Luminosity and laser-induced incandescence investigations on a DI gasoline engine. SAE Transactions, 2085–2093. http://dx.doi.org/10.4271/2000-01-2903.
- Bohren, C. F., & Huffman, D. R. (2008). Absorption and scattering of light by small particles. John Wiley & Sons, http://dx.doi.org/10.1002/9783527618156.
- Boiger, R., Modini, R. L., Moallemi, A., Degen, D., Adelmann, A., & Gysel-Beer, M. (2022). Retrieval of aerosol properties from in situ, multi-angle light scattering measurements using invertible neural networks. *Journal of Aerosol Science*, 163, Article 105977. http://dx.doi.org/10.1016/j.jaerosci.2022.105977.
- Boldon, L., Laliberte, F., & Liu, L. (2015). Review of the fundamental theories behind small angle X-ray scattering, molecular dynamics simulations, and relevant integrated application. *Nano Reviews*, 6(1), 25661. http://dx.doi.org/10.3402/nano.v6.25661.
- Bond, T. C. (2001). Spectral dependence of visible light absorption by carbonaceous particles emitted from coal combustion. *Geophysical Research Letters*, 28(21), 4075–4078. http://dx.doi.org/10.1029/2001gl013652.
- Bond, T. C., & Bergstrom, R. W. (2006). Light absorption by carbonaceous particles: An investigative review. Aerosol Science and Technology, 40(1), 27–67. http://dx.doi.org/10.1080/02786820500421521.
- Botero, M. L., Akroyd, J., Chen, D., Kraft, M., & Agudelo, J. R. (2021). On the thermophoretic sampling and TEM-based characterisation of soot particles in flames. *Carbon*, 171, 711–722. http://dx.doi.org/10.1016/j.carbon.2020.09.074.
- Bourrous, S., Ribeyre, Q., Lintis, L., Yon, J., Bau, S., Thomas, D., et al. (2018). A semi-automatic analysis tool for the determination of primary particle size, overlap coefficient and specific surface area of nanoparticles aggregates. *Journal of Aerosol Science*, 126, 122–132. http://dx.doi.org/10.1016/j.jaerosci.2018.09.001.
- Bouvier, M., Yon, J., Lefevre, G., & Grisch, F. (2019). A novel approach for in-situ soot size distribution measurement based on spectrally resolved light scattering. Journal of Quantitative Spectroscopy and Radiative Transfer, 225, 58–68. http://dx.doi.org/10.1016/j.jqsrt.2018.12.018.
- Brasil, A. M., Farias, T. L., & Carvalho, M. G. (1999). A recipe for image characterization of fractal-like aggregates. *Journal of Aerosol Science*, 30(10), 1379–1389. Braun, A., Shah, N., Huggins, F. E., Kelly, K., Sarofim, A., Jacobsen, C., et al. (2005). X-ray scattering and spectroscopy studies on diesel soot from oxygenated fuel under various engine load conditions. *Carbon*, 43(12), 2588–2599. http://dx.doi.org/10.1016/j.carbon.2005.05.017.
- Breitegger, P., Schriefl, M. A., Nishida, R. T., Hochgreb, S., & Bergmann, A. (2019). Soot mass concentration sensor using quartz-enhanced photoacoustic spectroscopy. *Aerosol Science and Technology*, 53(9), 971–975. http://dx.doi.org/10.1080/02786826.2019.1635677.
- Brockmann, J., & Rader, D. (1990). APS response to nonspherical particles and experimental determination of dynamic shape factor. *Aerosol Science and Technology*, 13(2), 162–172.
- Broda, K. N., Olfert, J. S., Irwin, M., Schill, G. P., McMeeking, G. R., Schnitzler, E. G., et al. (2018). A novel inversion method to determine the mass distribution of non-refractory coatings on refractory black carbon using a centrifugal particle mass analyzer and single particle soot photometer. *Aerosol Science and Technology*, 52(5), 567–578. http://dx.doi.org/10.1080/02786826.2018.1433812.
- Brunauer, S., Emmett, P., & Teller, E. (1938). Adsorption of gases in multimolecular layers. *Journal of the American Chemical Society*, 60(309), http://dx.doi.org/10.1021/ja01269a023.
- Buckley, D. T., Kimoto, S., Lee, M. H., Fukushima, N., & Hogan Jr., C. J. (2017). A corrected two dimensional data inversion routine for tandem mobility-mass measurements. *Journal of Aerosol Science*, 114, 157–168.
- Burr, D., Daun, K., Link, O., Thomson, K., & Smallwood, G. (2011). Determination of the soot aggregate size distribution from elastic light scattering through Bayesian inference. *Journal of Quantitative Spectroscopy and Radiative Transfer*, 112(6), 1099–1107. http://dx.doi.org/10.1016/j.jqsrt.2010.12.001.
- Burr, D., Daun, K., Thomson, K., & Smallwood, G. (2012). Optimization of measurement angles for soot aggregate sizing by elastic light scattering, through design-of-experiment theory. *Journal of Quantitative Spectroscopy and Radiative Transfer*, 113(5), 355–365.
- Cabarcos, A., Paz, C., Pérez-Orozco, R., & Vence, J. (2022). An image-processing algorithm for morphological characterisation of soot agglomerates from TEM micrographs: Development and functional description. *Powder Technology*, 401, Article 117275.
- Cai, J., Lu, N., & Sorensen, C. (1993). Comparison of size and morphology of soot aggregates as determined by light scattering and electron microscope analysis. *Langmuir*, 9(11), 2861–2867.
- Cai, R., Yang, D., Ahonen, L. R., Shi, L., Korhonen, F., Ma, Y., et al. (2018). Data inversion methods to determine sub-3 nm aerosol size distributions using the particle size magnifier. *Atmospheric Measurement Techniques*, 11(7), 4477–4491.
- Cambustion (2022). Mass & mobility aerosol spectrometer. URL https://www.cambustion.com/products/analytical-instrumentation/m2as-mass-mobility-aerosol-separator.
- Camenzind, A., Caseri, W. R., & Pratsinis, S. E. (2010). Flame-made nanoparticles for nanocomposites. *Nano Today*, 5(1), 48–65. http://dx.doi.org/10.1016/j.nantod.2009.12.007.
- Cardello, N., Volckens, J., Tolocka, M. P., Wiener, R., & Buckley, T. J. (2002). Technical note: Performance of a personal electrostatic precipitator particle sampler. Aerosol Science and Technology, 36(2), 162–165. http://dx.doi.org/10.1080/027868202753504029.
- Carfora, M. F., Esposito, F., & Serio, C. (1998). Numerical methods for retrieving aerosol size distributions from optical measurements of solar radiation. *Journal of Aerosol Science*, 29(10), 1225–1236.

- Carsí, M., & Alonso, M. (2022). A simple correlation to estimate the resolution of concentric cylindrical DMAs for diffusive particles. *Journal of Aerosol Science*, Article 106089.
- Caumont-Prim, C., Yon, J., Coppalle, A., Ouf, F. X., & Ren, K. F. (2013). Measurement of aggregates' size distribution by angular light scattering. *Journal of Quantitative Spectroscopy and Radiative Transfer*, 126, 140–149. http://dx.doi.org/10.1016/j.jqsrt.2012.07.029.
- Chahine, M. T. (1968). Determination of the temperature profile in an atmosphere from its outgoing radiance. *Journal of the Optical Society of America*, 58(12), 1634–1637. http://dx.doi.org/10.1364/JOSA.58.001634.
- Chakrabarty, R. K., Garro, M. A., Garro, B. A., Chancellor, S., Moosmüller, H., & Herald, C. M. (2011a). Simulation of aggregates with point-contacting monomers in the cluster-dilute regime. Part 1: Determining the most reliable technique for obtaining three-dimensional fractal dimension from two-dimensional images. *Aerosol Science and Technology*, 45(1), 75–80. http://dx.doi.org/10.1080/02786826.2010.520363.
- Chakrabarty, R. K., Garro, M. A., Garro, B. A., Chancellor, S., Moosmüller, H., & Herald, C. M. (2011b). Simulation of aggregates with point-contacting monomers in the cluster-dilute regime. Part 2: Comparison of two- and three-dimensional structural properties as a function of fractal dimension. *Aerosol Science and Technology*, 45(8), 903–908. http://dx.doi.org/10.1080/02786826.2011.568022.
- Chakrabarty, R. K., & Heinson, W. R. (2018). Scaling laws for light absorption enhancement due to nonrefractory coating of atmospheric black carbon aerosol. Physical Review Letters, 121(21), Article 218701. http://dx.doi.org/10.1103/PhysRevLett.121.218701.
- Chakrabarty, R. K., Moosmüller, H., Arnott, W. P., Garro, M. A., Slowik, J. G., Cross, E. S., et al. (2007). Light scattering and absorption by fractal-like carbonaceous chain aggregates: Comparison of theories and experiment. *Applied Optics*, 46(28), 6990–7006. http://dx.doi.org/10.1364/ao.46.006990.
- Chakrabarty, R. K., Moosmüller, H., Arnott, W. P., Garro, M. A., Tian, G., Slowik, J. G., et al. (2009). Low fractal dimension cluster-dilute soot aggregates from a premixed flame. *Physical Review Letters*, 102(23), Article 235504.
- Chakrabarty, R. K., Moosmüller, H., Garro, M. A., & Stipe, C. B. (2012). Observation of superaggregates from a reversed gravity low-sooting flame. *Aerosol Science and Technology*, 46(1), i–iii. http://dx.doi.org/10.1080/02786826.2011.608389.
- Chang, H. c., & Charalampopoulos, T. (1990). Determination of the wavelength dependence of refractive indices of flame soot. Proceedings of the Royal Society of London. Series A: Mathematical and Physical Sciences, 430(1880), 577–591. http://dx.doi.org/10.1098/rspa.1990.0107.
- Chang, H., Lin, W. Y., & Biswas, P. (1995). An inversion technique to determine the aerosol size distribution in multicomponent systems from in situ light scattering measurements. Aerosol Science and Technology, 22(1), 24–32.
- Charalampopoulos, T. (1992). Morphology and dynamics of agglomerated particulates in combustion systems using light scattering techniques. *Progress in Energy and Combustion Science*, 18(1), 13–45.
- Charalampopoulos, T., & Chang, H. (1988). In situ optical properties of soot particles in the wavelength range from 340 nm to 600 nm. Combustion Science and Technology, 59(4-6), 401–421. http://dx.doi.org/10.1080/00102208808947108.
- Charalampopoulos, T., & Felske, J. (1987). Refractive indices of soot particles deduced from in-situ laser light scattering measurements. *Combustion and Flame*, 68(3), 283–294. http://dx.doi.org/10.1016/0010-2180(87)90005-8.
- Charvet, A., Bau, S., Bémer, D., & Thomas, D. (2015). On the importance of density in ELPI data post-treatment. Aerosol Science and Technology, 49(12), 1263–1270. http://dx.doi.org/10.1080/02786826.2015.1117568.
- Charvet, A., Bau, S., Paez Coy, N. E., Bémer, D., & Thomas, D. (2014). Characterizing the effective density and primary particle diameter of airborne nanoparticles produced by spark discharge using mobility and mass measurements (tandem DMA/APM). *Journal of Nanoparticle Research*, 16(5), 1–11. http://dx.doi.org/10.1007/s11051-014-2418-y.
- Charwath, M., Suntz, R., & Bockhorn, H. (2006). Influence of the temporal response of the detection system on time-resolved laser-induced incandescence signal evolutions. *Applied Physics B*, 83, 435–442.
- Chen, C., Enekwizu, O. Y., Fan, X., Dobrzanski, C. D., Ivanova, E. V., Ma, Y., et al. (2018). Single parameter for predicting the morphology of atmospheric black carbon. *Environmental Science and Technology*, 52(24), 14169–14179.
- Chen, X., Ghosh, S., Buckley, D. T., Sankaran, R. M., & Hogan, C. J. (2018). Characterization of the state of nanoparticle aggregation in non-equilibrium plasma synthesis systems. *Journal of Physics D: Applied Physics*, 51(33), Article 335203. http://dx.doi.org/10.1088/1361-6463/aad26f.
- Chen, C., Zakharov, D. N., & Khalizov, A. F. (2023). Drastically different restructuring of airborne and surface-anchored soot aggregates. *Journal of Aerosol Science*, 168, Article 106103. http://dx.doi.org/10.1016/j.jaerosci.2022.106103.
- Cheng, Y., Keating, J., & Kanapilly, G. (1980). Theory and calibration of a screen-type diffusion battery. Journal of Aerosol Science, 11(5-6), 549-556.
- China, S., Mazzoleni, C., Gorkowski, K., Aiken, A. C., & Dubey, M. K. (2013). Morphology and mixing state of individual freshly emitted wildfire carbonaceous particles. *Nature Communications*, 4(1), 2122. http://dx.doi.org/10.1038/ncomms3122.
- Chu, H., Han, W., Cao, W., Tao, C., Raza, M., & Chen, L. (2019). Experimental investigation of soot morphology and primary particle size along axial and radial direction of an ethylene diffusion flame via electron microscopy. *Journal of the Energy Institute*, 92(5), 1294–1302. http://dx.doi.org/10.1016/j.joei.2018.10.
- Cohan, L., & Watson, J. (1951). Shape factor and other fundamental properties of carbon black. Rubber Age, 68, 687.
- Colbeck, I., Appleby, L., Hardman, E., & Harrison, R. M. (1990). The optical properties and morphology of cloud-processed carbonaceous smoke. *Journal of Aerosol Science*, 21(4), 527–538. http://dx.doi.org/10.1016/0021-8502(90)90129-L.
- Collaud Coen, M., Weingartner, E., Apituley, A., Ceburnis, D., Fierz-Schmidhauser, R., Flentje, H., et al. (2010). Minimizing light absorption measurement artifacts of the Aethalometer: evaluation of five correction algorithms. *Atmospheric Measurement Techniques*, 3(2), 457–474. http://dx.doi.org/10.5194/amt-3-457-2010.
- Collins, D. R., Flagan, R. C., & Seinfeld, J. H. (2002). Improved inversion of scanning DMA data. Aerosol Science & Technology, 36(1), 1-9.
- Corbin, J. C., Czech, H., Massabò, D., de Mongeot, F. B., Jakobi, G., Liu, F., et al. (2019). Infrared-absorbing carbonaceous tar can dominate light absorption by marine-engine exhaust. *Npj Climate and Atmospheric Science*, 2(1), http://dx.doi.org/10.1038/s41612-019-0069-5.
- Corbin, J. C., & Gysel-Beer, M. (2019). Detection of tar brown carbon with a single particle soot photometer (SP2). Atmospheric Chemistry and Physics, 19(24), 15673–15690. http://dx.doi.org/10.5194/acp-19-15673-2019.
- Corbin, J. C., Johnson, T. J., Liu, F., Sipkens, T. A., Johnson, M. P., Lobo, P., et al. (2022). Size-dependent mass absorption cross-section of soot particles from various sources. *Carbon.* 192, 438–451. http://dx.doi.org/10.1016/j.carbon.2022.02.037.
- Corbin, J. C., Moallemi, A., Liu, F., Gagné, S., Olfert, J. S., Smallwood, G. J., et al. (2020). Closure between particulate matter concentrations measured ex situ by thermal-optical analysis and in situ by the CPMA-electrometer reference mass system. *Aerosol Science and Technology*, 54(11), 1293–1309. http://dx.doi.org/10.1080/02786826.2020.1788710.
- Corbin, J. C., Modini, R. L., & Gysel-Beer, M. (2023). Mechanisms of soot-aggregate restructuring and compaction. Aerosol Science and Technology, 57(2), 89–111. http://dx.doi.org/10.1080/02786826.2022.2137385.
- Corbin, J. C., Schripp, T., Anderson, B. E., Smallwood, G. J., LeClercq, P., Crosbie, E. C., et al. (2022). Aircraft-engine particulate matter emissions from conventional and sustainable aviation fuel combustion: comparison of measurement techniques for mass, number, and size. *Atmospheric Measurement Techniques*, 15(10), 3223–3242. http://dx.doi.org/10.5194/amt-15-3223-2022.
- Coudray, N., Dieterlen, A., Roth, E., & Trouvé, G. (2009). Density measurement of fine aerosol fractions from wood combustion sources using ELPI distributions and image processing techniques. Fuel, 88(5), 947–954.
- Covert, D. S., & Heintzenberg, J. (1993). Size distributions and chemical properties of aerosol at Ny Ålesund, Svalbard. Atmospheric Environment. Part A. General Topics, 27(17–18), 2989–2997. http://dx.doi.org/10.1016/0960-1686(93)90331-R.

- Cremer, J. W., Covert, P. A., Parmentier, E. A., & Signorell, R. (2017). Direct measurement of photoacoustic signal sensitivity to aerosol particle size. *The Journal of Physical Chemistry Letters*, 8(14), 3398–3403. http://dx.doi.org/10.1021/acs.jpclett.7b01288.
- Crosland, B., Thomson, K., & Johnson, M. (2013). Instantaneous in-flame measurement of soot volume fraction, primary particle diameter, and aggregate radius of gyration via auto-compensating laser-induced incandescence and two-angle elastic light scattering. Applied Physics B, 112, 381–393.
- Cruz, C. N., & Pandis, S. N. (1998). The effect of organic coatings on the cloud condensation nuclei activation of inorganic atmospheric aerosol. *Journal of Geophysical Research: Atmospheres*, 103(D11), 13111–13123. http://dx.doi.org/10.1029/98JD00979.
- Dastanpour, R., Boone, J. M., & Rogak, S. N. (2016). Automated primary particle sizing of nanoparticle aggregates by TEM image analysis. *Powder Technology*, 295, 218–224.
- Dastanpour, R., & Rogak, S. N. (2014). Observations of a correlation between primary particle and aggregate size for soot particles. *Aerosol Science and Technology*, 48(10), 1043–1049. http://dx.doi.org/10.1080/02786826.2014.955565.
- Daun, K. (2010). Effect of selective accommodation on soot aggregate shielding in time-resolved laser-induced incandescence experiments. *Journal of Heat Transfer*, 132(9).
- Davies, C. (1945). Definitive equations for the fluid resistance of spheres. Proceedings of the Physical Society, 57(4), 259. http://dx.doi.org/10.1088/0959-5309/57/4/301.
- De Iuliis, S., Cignoli, F., & Zizak, G. (2005). Two-color laser-induced incandescence (2C-LII) technique for absolute soot volume fraction measurements in flames. Applied Optics, 44(34), 7414–7423.
- De Temmerman, P. J., Verleysen, E., Lammertyn, J., & Mast, J. (2014). Semi-automatic size measurement of primary particles in aggregated nanomaterials by transmission electron microscopy. *Powder Technology*, 261, 191–200. http://dx.doi.org/10.1016/j.powtec.2014.04.040.
- DeCarlo, P. F., Slowik, J. G., Worsnop, D. R., Davidovits, P., & Jimenez, J. L. (2004). Particle morphology and density characterization by combined mobility and aerodynamic diameter measurements. Part 1: Theory. Aerosol Science and Technology, 38(12), 1185–1205. http://dx.doi.org/10.1080/027868290903907.
- Desgroux, P., Mercier, X., & Thomson, K. A. (2013). Study of the formation of soot and its precursors in flames using optical diagnostics. *Proceedings of the Combustion Institute*, 34(1), 1713–1738. http://dx.doi.org/10.1016/j.proci.2012.09.004.
- Dhaubhadel, R., Rieker, T., Chakrabarti, A., & Sorensen, C. M. (2012). Synthesis of silica aerosol gels via controlled detonation. Aerosol Science and Technology, 46(5), 596–600.
- Di Stasio, S. (2017). Soot with 1013 cm- 3 high concentration and 25 Åradius of gyration as detected by small-angle X-ray scattering in a premixed ethylene-air flame at sooting threshold. *Journal of Aerosol Science*, 110, 11–24.
- Di Stasio, S., Mitchell, J., LeGarrec, J. L., Biennier, L., & Wulff, M. (2006). Synchrotron SAXS in situ identification of three different size modes for soot nanoparticles in a diffusion flame. *Carbon*, 44(7), 1267–1279. http://dx.doi.org/10.1016/j.carbon.2005.10.042.
- Dickau, M., Johnson, T. J., Thomson, K., Smallwood, G., & Olfert, J. S. (2015). Demonstration of the CPMA-electrometer system for calibrating black carbon particulate mass instruments. *Aerosol Science and Technology*, 49(3), 152–158. http://dx.doi.org/10.1080/02786826.2015.1010033.
- Dickau, M., Olfert, J., Stettler, M., Boies, A., Momenimovahed, A., Thomson, K., et al. (2016). Methodology for quantifying the volatile mixing state of an aerosol. Aerosol Science and Technology, 50(8), 759–772. http://dx.doi.org/10.1080/02786826.2016.1185509.
- Diveky, M. E., Roy, S., David, G., Cremer, J. W., & Signorell, R. (2020). Fundamental investigation of photoacoustic signal generation from single aerosol particles at varying relative humidity. *Photoacoustics*, 18, Article 100170. http://dx.doi.org/10.1016/j.pacs.2020.100170.
- Dixkens, J., & Fissan, H. (1999). Development of an electrostatic precipitator for off-line particle analysis. Aerosol Science and Technology, 30(5), 438–453. http://dx.doi.org/10.1080/027868299304480.
- Do, C. B., & Batzoglou, S. (2008). What is the expectation maximization algorithm? *Nature biotechnology*, 26(8), 897–899. http://dx.doi.org/10.1038/nbt1406. Dobbins, R., & Megaridis, C. (1987). Morphology of flame-generated soot as determined by thermophoretic sampling. *Langmuir*, 3, 254–259. http://dx.doi.org/10.1080/02786820500385569.
- Dobbins, R. A., & Megaridis, C. M. (1991). Absorption and scattering of light by polydisperse aggregates. *Applied Optics*, 30(33), 4747–4754. http://dx.doi.org/10.1364/AO.30.004747.
- Drinovec, L., Jagodič, U., Pirker, L., Škarabot, M., Kurtjak, M., Vidović, K., et al. (2022). A dual-wavelength photothermal aerosol absorption monitor: design, calibration and performance. Atmospheric Measurement Techniques, 15(12), 3805–3825. http://dx.doi.org/10.5194/amt-15-3805-2022.
- Driscoll, J., M. Mann, D., & McGregor, W. K. (1979). Submicron particle size measurements in an acetylene-oxygen flame. Combustion Science and Technology, 20(1–2), 41–47. http://dx.doi.org/10.1080/00102207908946895.
- Dubey, P., & Dhaniyala, S. (2013). Improved inversion of scanning electrical mobility spectrometer data using a new multiscale expectation maximization algorithm. Aerosol Science and Technology, 47(1), 69–80.
- Duelge, K., Mulholland, G., Zachariah, M., & Hackley, V. A. (2022). Accurate nanoparticle size determination using electrical mobility measurements in the step and scan modes. Aerosol Science and Technology, 56(12), 1096–1113.
- Eggersdorfer, M. L., Kadau, D., Herrmann, H. J., & Pratsinis, S. E. (2012). Aggregate morphology evolution by sintering: Number and diameter of primary particles. *Journal of Aerosol Science*, 46, 7–19. http://dx.doi.org/10.1016/j.jaerosci.2011.11.005.
- Eggersdorfer, M. L., & Pratsinis, S. E. (2014). Agglomerates and aggregates of nanoparticles made in the gas phase. Advanced Powder Technology, 25(1), 71–90. http://dx.doi.org/10.1016/j.apt.2013.10.010.
- Ehara, K., Hagwood, C., & Coakley, K. J. (1996). Novel method to classify aerosol particles according to their mass-to-charge ratio aerosol particle mass analyser. *Journal of Aerosol Science*, 27(2), 217–234.
- El Omary, Y. (1994). Modeles deformables et multiresolution pour la detection de contours en traitement d'images (Ph.D. thesis), Université Joseph-Fourier-Grenoble I. Enekwizu, O. Y., Hasani, A., & Khalizov, A. F. (2021). Vapor condensation and coating evaporation are both responsible for soot aggregate restructuring. Environmental Science and Technology, 55(13), 8622–8630. http://dx.doi.org/10.1021/acs.est.1c02391.
- England, W. (1986). An in situ X-ray small angle scattering study of soot morphology in flames. Combustion Science and Technology, 46(1–2), 83–93. http://dx.doi.org/10.1080/00102208608959793.
- Farias, T. L., Carvalho, M. d. G., Köylü, U. O., & Faeth, G. (1995). Computational evaluation of approximate Rayleigh–Debye–Gans/fractal-aggregate theory for the absorption and scattering properties of soot. ournal of Heat Transfer, 117(1), 152–159. http://dx.doi.org/10.1115/1.2822296.
- Farias, T. L., Köylü, Ü. Ö., & Carvalho, M. d. G. (1996). Range of validity of the Rayleigh–Debye–Gans theory for optics of fractal aggregates. *Applied Optics*, 35(33), 6560–6567. http://dx.doi.org/10.1364/AO.35.006560.
- Fenidel, W., Matter, D., Burtscher, H., & Schmidt-Ott, A. (1995). Interaction between carbon or iron aerosol particles and ozone. Atmospheric Environment, 29(9), 967–973.
- Ferraro, G., Fratini, E., Rausa, R., Fiaschi, P., & Baglioni, P. (2016). Multiscale characterization of some commercial carbon blacks and diesel engine soot. *Energy & Fuels*, 30(11), 9859–9866. http://dx.doi.org/10.1021/acs.energyfuels.6b01740.
- Fierz, M., Houle, C., Steigmeier, P., & Burtscher, H. (2011). Design, calibration, and field performance of a miniature diffusion size classifier. *Aerosol Science and Technology*, 45(1), 1–10. http://dx.doi.org/10.1080/02786826.2010.516283.
- Fierz, M., Kaegi, R., & Burtscher, H. (2007). Theoretical and experimental evaluation of a portable electrostatic TEM sampler. Aerosol Science and Technology, 41(5), 520–528. http://dx.doi.org/10.1080/02786820701253327.
- Fierz, M., Weimer, S., & Burtscher, H. (2009). Design and performance of an optimized electrical diffusion battery. Journal of Aerosol Science, 40(2), 152-163.

- Filippov, A., Zurita, M., & Rosner, D. E. (2000). Fractal-like aggregates: relation between morphology and physical properties. *Journal of Colloid and Interface Science*, 229(1), 261–273.
- Fitch, B. W. (1983). Characteristics of aerosol volume distributions measured at Meppen, W. Germany: Technical Report, Scripps Institution OF Oceanography La Jolla CA Visibility Lab. https://apps.dtic.mil/sti/citations/ADA146138.
- Flagan, R. C. (2008). Differential mobility analysis of aerosols: A tutorial. KONA Powder and Particle Journal, 26, 254–268. http://dx.doi.org/10.14356/kona. 2008023.
- Flagan, R. C., & Seinfeld, J. H. (1988). Fundamentals of air pollution engineering. Prentice-Hall, Inc, http://dx.doi.org/10.1016/C2012-0-01172-6.
- Flower, W. (1983). Optical measurements of soot formation in premixed flames. Combustion Science and Technology, 33(1-4), 17-33. http://dx.doi.org/10.1080/00102208308923666.
- Forrest, S. R., & Witten, T. A. (1979). Long-range correlations in smoke-particle aggregates. Journal of Physics A: Mathematical and General, 12(5), L109–L117. http://dx.doi.org/10.1088/0305-4470/12/5/008.
- Frei, M., & Kruis, F. E. (2018). Fully automated primary particle size analysis of agglomerates on transmission electron microscopy images via artificial neural networks. *Powder Technology*, 332, 120–130.
- Frei, M., & Kruis, F. E. (2020). Image-based size analysis of agglomerated and partially sintered particles via convolutional neural networks. *Powder Technology*, 360, 324–336.
- Fuchs, N. A. (1963). On the stationary charge distribution on aerosol particles in a bipolar ionic atmosphere. *Geofisica Pura e Applicata*, 56, 185–193. http://dx.doi.org/10.1007/BF01993343.
- Gangopadhyay, S., Elminyawi, I., & Sorensen, C. M. (1991). Optical structure factor measurements of soot particles in a premixed flame. Applied Optics, 30(33), 4859-4864
- Gao, R. S., Schwarz, J. P., Kelly, K. K., Fahey, D. W., Watts, L. A., Thompson, T. L., et al. (2007). A novel method for estimating light-scattering properties of soot aerosols using a modified single-particle soot photometer. Aerosol Science and Technology, 41(2), 125–135. http://dx.doi.org/10.1080/02786820601118398.
- Gao, R. S., Telg, H., McLaughlin, R. J., Ciciora, S. J., Watts, L. A., Richardson, M. S., et al. (2016a). A light-weight, high-sensitivity particle spectrometer for PM2.5 aerosol measurements. Aerosol Science and Technology, 50(1), 88–99. http://dx.doi.org/10.1080/02786826.2015.1131809.
- Gardner, C., Greaves, G., Hargrave, G., Jarvis, S., Wildman, P., Meneau, F., et al. (2005). In situ measurements of soot formation in simple flames using small angle X-ray scattering. Nuclear Instruments & Methods in Physics Research, Section B (Beam Interactions with Materials and Atoms), 238(1-4), 334-339. http://dx.doi.org/10.1016/j.nimb.2005.06.072.
- Gebhart, J. (1991). Response of single-particle optical counters to particles of irregular shape. Particle & Particle Systems Characterization, 8(1-4), 40-47. http://dx.doi.org/10.1002/ppsc.19910080109.
- Geigle, K., Migliorini, F., Yon, J., & Smallwood, G. (2022). Laser-induced incandescence and other particle diagnostics. In Optical diagnostics for reacting and non-reacting flows: Theory and practice (pp. 633–776). American Institute of Aeronautics and Astronautics, Inc. Reston, VA.
- Geisler, M., Larsen, J., Dirscherl, K., & Jensen, S. A. (2022). Numerical neural network approach to simultaneous material classification and sizing of aerosolized particles. *Journal of Quantitative Spectroscopy and Radiative Transfer*, 277, Article 107982.
- Geitlinger, H., Streibel, T., Suntz, R., & Bockhorn, H. (1999). Statistical analysis of soot volume fractions, particle number densities and particle radii in a turbulent diffusion flame. Combustion Science and Technology, 149(1-6), 115-134. http://dx.doi.org/10.1080/00102209908952102.
- Ghazi, R., & Olfert, J. S. (2013). Coating mass dependence of soot aggregate restructuring due to coatings of oleic acid and dioctyl sebacate. Aerosol Science and Technology, 47(2), 192–200. http://dx.doi.org/10.1080/02786826.2012.741273.
- Ghazi, R., Tjong, H., Soewono, A., Rogak, S. N., & Olfert, J. S. (2013). Mass, mobility, volatility, and morphology of soot particles generated by a McKenna and inverted burner. Aerosol Science and Technology, 47(4), 395–405.
- Ghiassi, H., Toth, P., Jaramillo, I. C., & Lighty, J. S. (2016). Soot oxidation-induced fragmentation: Part 1: The relationship between soot nanostructure and oxidation-induced fragmentation. Combustion and Flame, 163, 179–187. http://dx.doi.org/10.1016/j.combustflame.2015.09.023.
- Giechaskiel, B., Maricq, M., Ntziachristos, L., Dardiotis, C., Wang, X., Axmann, H., et al. (2014a). Review of motor vehicle particulate emissions sampling and measurement: From smoke and filter mass to particle number. *Journal of Aerosol Science*. 67: 48–86.
- Goldfarb, A., & Gentry, J. (1978). The characterization of the particle size distribution from oil-fired burners with a beta distribution. In M. M. Benarie (Ed.), Studies in environmental science: vol. 1, Atmospheric pollution 1978 (pp. 161–165). Elsevier, http://dx.doi.org/10.1016/S0166-1116(08)71566-8.
- Gonzalez, D., Nasibulin, A. G., Baklanov, A. M., Shandakov, S. D., Brown, D. P., Questier, P., et al. (2005). A new thermophoretic precipitator for collection of
- nanometer-sized aerosol particles. Aerosol Science and Technology, 39(11), 1064–1071.

 Gopalakrishnan, R., McMurry, P. H., & Hogan Jr., C. J. (2015). The bipolar diffusion charging of nanoparticles: A review and development of approaches for
- non-spherical particles. *Aerosol Science and Technology*, 49(12), 1181–1194.

 Gopalakrishnan, R., Meredith, M. J., Larriba-Andaluz, C., & Hogan, C. J. (2013). Brownian dynamics determination of the bipolar steady state charge distribution on spheres and non-spheres in the transition regime. *Journal of Aerosol Science*, 63, 126–145. http://dx.doi.org/10.1016/j.jaerosci.2013.04.007.
- Grassberger, P., & Procaccia, I. (1983). Characterization of strange attractors. *Physical Review Letters*, 50(5), 346. http://dx.doi.org/10.1103/PhysRevLett.50.346. Graves, B., Engelke, S., Jo, C., Baldovi, H. G., de la Verpilliere, J., De Volder, M., et al. (2020). Plasma production of nanomaterials for energy storage: continuous
- gas-phase synthesis of metal oxide CNT materials via a microwave plasma. *Nanoscale*, *12*, 5196–5208. http://dx.doi.org/10.1039/C9NR08886E. Graves, B. M., Koch, C. R., & Olfert, J. S. (2017). Morphology and volatility of particulate matter emitted from a gasoline direct injection engine fuelled on gasoline and ethanol blends. *Journal of Aerosol Science*, *105*, 166–178.
- Green, H. L., & Watson, H. H. (1935). Special report series No. 199: Technical Report, Medical Research Council.
- Grishin, I., Thomson, K., Migliorini, F., & Sloan, J. J. (2012). Application of the hough transform for the automatic determination of soot aggregate morphology. *Applied Optics*, 51(5), 610–620.
- Grulke, E. A., Rice, S. B., Xiong, J., Yamamoto, K., Yoon, T. H., Thomson, K., et al. (2018). Size and shape distributions of carbon black aggregates by transmission electron microscopy. *Carbon*, 130, 822–833.
- Gucker, F., & Rose, D. (1954). A photoelectronic instrument for counting and sizing aerosol particles. British Journal of Applied Physics, 5(S3), S138.
- Guinier, A. (1939). La diffraction des rayons x aux très petits angles: application à l'étude de phénomènes ultramicroscopiques. *Annales de Physique Onzieme Serie*, 12, 161–237. http://dx.doi.org/10.1051/anphys/193911120161.
- Guinier, A., Fournet, G., & Yudowitch, K. L. (1955). Small-angle scattering of X-rays. New York: Wiley.
- Gulak, Y., Jayjock, E., Muzzio, F., Bauer, A., & McGlynn, P. (2010). Inversion of andersen cascade impactor data using the maximum entropy method. Aerosol Science and Technology, 44(1), 29–37.
- Gunn, R., & Woessner, R. (1956). Measurements of the systematic electrification of aerosols. *Journal of Colloid Science*, 11(3), 254–259. http://dx.doi.org/10. 1016/0095-8522(56)90050-2.
- Gupta, A., Tang, D., & McMurry, P. (1995). Growth of monodisperse, submicron aerosol particles exposed to SO2, H2o2, and NH3. *Journal of Atmospheric Chemistry*, 20(2), 117–139. http://dx.doi.org/10.1007/BF00696554.
- Gysel, M., Laborde, M., Olfert, J., Subramanian, R., & Gröhn, A. (2011). Effective density of aquadag and fullerene soot black carbon reference materials used for SP2 calibration. Atmospheric Measurement Techniques, 4(12), 2851–2858. http://dx.doi.org/10.5194/amt-4-2851-2011.
- Haaf, W. (1980). Accurate measurements of aerosol size distribution—I. Theory of a plate condenser for bipolar mobility analysis. *Journal of Aerosol Science*, 11(2), 189–200.

- Haffner-Staton, E., Avanzini, L., La Rocca, A., Pfau, S., & Cairns, A. (2022). Automated particle recognition for engine soot nanoparticles. *Journal of Microscopy*, http://dx.doi.org/10.1111/jmi.13140.
- Haffner-Staton, E., La Rocca, A., Cairns, A., & Fay, M. (2019). Morphological characterization of gasoline soot-in-oil: Development of semi-automated 2D-TEM and comparison with novel high-throughput 3D-TEM: Technical Report, SAE Technical Paper, http://dx.doi.org/10.4271/2019-24-0042.
- Hagen, D. E., & Alofs, D. J. (1983). Linear inversion method to obtain aerosol size distributions from measurements with a differential mobility analyzer. *Aerosol Science and Technology*, 2(4), 465–475.
- Hagwood, C., Coakley, K., Negiz, A., & Ehara, K. (1995). Stochastic modeling of a new spectrometer. Aerosol Science and Technology, 23(4), 611–627. http://dx.doi.org/10.1080/02786829508965342.
- Halls, B. R., Jiang, N., Meyer, T. R., Roy, S., Slipchenko, M. N., & Gord, J. R. (2017). 4D spatiotemporal evolution of combustion intermediates in turbulent flames using burst-mode volumetric laser-induced fluorescence. Optics Letters, 42(14), 2830–2833.
- Han, C., Li, S. M., Liu, P., & Lee, P. (2018). Size dependence of the physical characteristics of particles containing refractory black carbon in diesel vehicle exhaust. Environmental Science and Technology, 53(1), 137–145.
- Hansen, P. C., & O'Leary, D. P. (1993). The use of the L-curve in the regularization of discrete ill-posed problems. SIAM Journal on Scientific Computing, 14(6), 1487–1503. http://dx.doi.org/10.1137/091408.
- Härk, E., & Ballauff, M. (2020). Carbonaceous materials investigated by small-angle X-ray and neutron scattering. *Journal of Carbon Research*, 6(4), 82. http://dx.doi.org/10.3390/c6040082.
- Harris, S. J., & Maricq, M. (2001). Signature size distributions for diesel and gasoline engine exhaust particulate matter. *Journal of Aerosol Science*, 32(6), 749–764. http://dx.doi.org/10.1016/S0021-8502(00)00111-7.
- Hatch, T., & Choate, S. P. (1929). Statistical description of the size properties of non uniform particulate substances. *Journal of the Franklin Institute*, 207(3), 369–387
- Heinson, W., Sorensen, C., & Chakrabarti, A. (2010). Does shape anisotropy control the fractal dimension in diffusion-limited cluster-cluster aggregation? *Aerosol Science and Technology*, 44(12), i–iv. http://dx.doi.org/10.1080/02786826.2010.516032.
- Heintzenberg, J. (1994). Properties of the log-normal particle size distribution. Aerosol Science and Technology, 21(1), 46-48.
- Hering, S. V., Lewis, G. S., Spielman, S. R., Eiguren-Fernandez, A., Kreisberg, N. M., Kuang, C., et al. (2017). Detection near 1-nm with a laminar-flow, water-based condensation particle counter. *Aerosol Science and Technology*, 51(3), 354–362. http://dx.doi.org/10.1080/02786826.2016.1262531.
- Hess, W., Ban, L., & McDonald, G. (1969). Carbon black morphology: I. Particle microstructure. II. Automated EM analysis of aggregate size and shape. Rubber Chemistry and Technology, 42(4), 1209–1234. http://dx.doi.org/10.5254/1.3539291.
- Hess, W. M., & Herd, C. R. (2018). Microstructure, morphology and general physical properties. In Carbon black (pp. 89–173). Routledge, http://dx.doi.org/10. 1201/9781315138763-3.
- Hessler, J., Seifert, S., & Winans, R. (2002). Spatially resolved small-angle x-ray scattering studies of soot inception and growth. *Proceedings of the Combustion Institute*, 29(2), 2743–2748. http://dx.doi.org/10.1016/S1540-7489(02)80334-0.
- Hewitt, G. W. (1957). The charging of small particles for electrostatic precipitation. Transactions of the American Institute of Electrical Engineers, Part I: Communication and Electronics, 76(3), 300–306. http://dx.doi.org/10.1109/TCE.1957.6372672.
- Hinds, W. C. (1999). Aerosol technology: Properties, behavior, and measurement of airborne particles. John Wiley & Sons.
- Hinds, W., & Reist, P. (1972). Aerosol measurement by laser doppler spectroscopy—I. Theory and experimental results for aerosols homogeneous. *Journal of Aerosol Science*, 3(6), 501–514.
- Hodkinson, J. R., & Greenfield, J. R. (1965). Response calculations for light-scattering aerosol counters and photometers. *Applied Optics*, 4(11), 1463–1474. http://dx.doi.org/10.1364/AO.4.001463.
- Hogan Jr., C. J., Li, L., Chen, D. r., & Biswas, P. (2009). Estimating aerosol particle charging parameters using a Bayesian inversion technique. *Journal of Aerosol Science*, 40(4), 295–306.
- Hoppel, W. (1978). Determination of the aerosol size distribution from the mobility distribution of the charged fraction of aerosols. *Journal of Aerosol Science*, 9(1), 41–54.
- Hoppel, W. A., & Frick, G. M. (1986). Ion—aerosol attachment coefficients and the steady-state charge distribution on aerosols in a bipolar ion environment. *Aerosol Science and Technology*, 5(1), 1–21. http://dx.doi.org/10.1080/02786828608959073.
- Howell, S. G., Freitag, S., Dobracki, A., Smirnow, N., & Sedlacek Iii, A. J. (2021). Undersizing of aged African biomass burning aerosol by an ultra-high-sensitivity aerosol spectrometer. *Atmospheric Measurement Techniques*, 14(11), 7381–7404. http://dx.doi.org/10.5194/amt-14-7381-2021.
- Hu, K., Liu, D., Tian, P., Wu, Y., Deng, Z., Wu, Y., et al. (2021). Measurements of the diversity of shape and mixing state for ambient black carbon particles. Geophysical Research Letters, 48(17), http://dx.doi.org/10.1029/2021GL094522.
- Hu, K., Liu, D., Tian, P., Wu, Y., Li, S., Zhao, D., et al. (2022). Identifying the fraction of core-shell black carbon particles in a complex mixture to constrain the absorption enhancement by coatings. *Environmental Science & Technology Letters*, 9(4), 272–279. http://dx.doi.org/10.1021/acs.estlett.2c00060.
- Hu, Q., Qiu, Z., Hong, J., & Chen, D. (2021). A polarized scanning nephelometer for measurement of light scattering of an ensemble-averaged matrix of aerosol particles. *Journal of Quantitative Spectroscopy and Radiative Transfer*, 261, Article 107497. http://dx.doi.org/10.1016/j.jqsrt.2020.107497.
- Huber, F. J., Altenhoff, M., & Will, S. (2016). A mobile system for a comprehensive online-characterization of nanoparticle aggregates based on wide-angle light scattering and laser-induced incandescence. Review of Scientific Instruments, 87(5), Article 053102.
- Huber, F. J., Will, S., & Daun, K. J. (2016). Sizing aerosolized fractal nanoparticle aggregates through Bayesian analysis of wide-angle light scattering (WALS) data. *Journal of Quantitative Spectroscopy and Radiative Transfer*, 184, 27–39.
- Hyeon-Lee, J., Beaucage, G., Pratsinis, S. E., & Vemury, S. (1998). Fractal analysis of flame-synthesized nanostructured silica and titania powders using small-angle X-ray scattering. *Langmuir*, 14(20), 5751–5756. http://dx.doi.org/10.1021/la980308s.
- Ikezawa, S., Wakamatsu, M., Zimin, Y. L., Pawlat, J., & Ueda, T. (2011). Development of carbonaceous particle size analyzer using laser-induced incandescence technology. *IEEJ Transactions on Sensors and Micromachines*, 131(5), 171–177. http://dx.doi.org/10.1541/ieejsmas.131.171.
- Intra, P., & Tippayawong, N. (2008). An overview of differential mobility analyzers for size classification of nanometer-sized aerosol particles. Songklanakarin Journal of Science & Technology, 30(2).
- Irwin, M., Kondo, Y., Moteki, N., & Miyakawa, T. (2013). Evaluation of a heated-inlet for calibration of the SP2. Aerosol Science and Technology, 47(8), 895–905. http://dx.doi.org/10.1080/02786826.2013.800187.
- ISO (2000). Reciprocating internal combustion engines Exhaust emission measurement, Vol. 2019: Standard, Geneva, CH: International Organization for Standardization.
- ISO (2010). ISO 9277:2010, Determination of the specific surface area of solids by gas adsorption BET method: Standard, Geneva, CH: International Organization for Standardization.
- ISO (2020a). ISO 15900:2020, Determination of particle size distribution Differential electrical mobility analysis for aerosol particles: Standard, Geneva, CH: International Organization for Standardization.
- ISO (2020b). ISO 21363:2020, Nanotechnologies Measurements of particle size and shape distributions by transmission electron microscopy: Standard, Geneva, CH: International Organization for Standardization.
- ISO (2020c). ISO 21501, Determination of particle size distribution Single particle light interaction methods: Standard, Geneva, CH: International Organization for Standardization.

- Iyer, S. S., Litzinger, T. A., Lee, S.-Y., & Santoro, R. J. (2007). Determination of soot scattering coefficient from extinction and three-angle scattering in a laminar diffusion flame. Combustion and Flame. 149(1-2), 206-216.
- Johnson, M., Devillers, R., & Thomson, K. (2013). A generalized sky-LOSA method to quantify soot/black carbon emission rates in atmospheric plumes of gas flares. Aerosol Science and Technology, 47(9), 1017–1029.
- Johnson, T. J., Irwin, M., Symonds, J. P. R., Olfert, J. S., & Boies, A. M. (2018). Measuring aerosol size distributions with the aerodynamic aerosol classifier. Aerosol Science and Technology, 52(6), 655–665. http://dx.doi.org/10.1080/02786826.2018.1440063.
- Johnson, T. J., Nishida, R. T., Irwin, M., Symonds, J. P., Olfert, J. S., & Boies, A. M. (2020). Measuring the bipolar charge distribution of nanoparticles: Review of methodologies and development using the Aerodynamic Aerosol Classifier. *Journal of Aerosol Science*, 143, Article 105526. http://dx.doi.org/10.1016/j. jaerosci.2020.105526.
- Johnson, T. J., Nishida, R. T., Zhang, X., Symonds, J. P., Olfert, J. S., & Boies, A. M. (2021b). Generating an aerosol of homogeneous, non-spherical particles and measuring their bipolar charge distribution. *Journal of Aerosol Science*, 153, Article 105705. http://dx.doi.org/10.1016/j.jaerosci.2020.105705.
- Johnson, T. J., Olfert, J. S., Cabot, R., Treacy, C., Yurteri, C. U., Dickens, C., et al. (2014). Steady-state measurement of the effective particle density of cigarette smoke. *Journal of Aerosol Science*, 75, 9–16. http://dx.doi.org/10.1016/j.jaerosci.2014.04.006.
- Johnson, T. J., Olfert, J. S., Cabot, R., Treacy, C., Yurteri, C. U., Dickens, C., et al. (2015). Transient measurement of the effective particle density of cigarette smoke. *Journal of Aerosol Science*, 87, 63–74. http://dx.doi.org/10.1016/j.jaerosci.2015.05.006.
- Johnson, T. J., Olfert, J. S., Symonds, J. P., Johnson, M., Rindlisbacher, T., Swanson, J. J., et al. (2015). Effective density and mass-mobility exponent of aircraft turbine particulate matter. *Journal of Propulsion and Power*, 31(2), 573–582. http://dx.doi.org/10.2514/1.B35367.
- Johnson, T. J., Symonds, J. P. R., Olfert, J. S., & Boies, A. M. (2021). Accelerated measurements of aerosol size distributions by continuously scanning the aerodynamic aerosol classifier. *Aerosol Science and Technology*, 55(2), 119–141. http://dx.doi.org/10.1080/02786826.2020.1830941.
- Johnsson, J., Bladh, H., Olofsson, N.-E., & Bengtsson, P.-E. (2013). Influence of soot aggregate structure on particle sizing using laser-induced incandescence: importance of bridging between primary particles. *Applied Physics B*, 112(3), 321–332. http://dx.doi.org/10.1007/s00340-013-5355-z.
- Jourdain, C., Symonds, J., & Boies, A. M. (2023). Compact Aerosol Aggregate Model (CA²M): A fast tool to estimate the aerosol properties of fractal-like aggregates. Aerosol Science and Technology, http://dx.doi.org/10.1080/02786826.2023.2206442.
- Jung, H., & Kittelson, D. B. (2005). Characterization of aerosol surface instruments in transition regime. Aerosol Science and Technology, 39(9), 902–911. http://dx.doi.org/10.1080/02786820500295701.
- Jung, H., & Kittelson, D. B. (2007). Characterization of Aerosol Surface Instruments in Transition Regime. Aerosol Science & Technology, 39(9), 902–911. http://dx.doi.org/10.1080/02786820500295701.
- Jung, H., Kittelson, D. B., & Zachariah, M. R. (2004). Kinetics and visualization of soot oxidation using transmission electron microscopy. *Combustion and Flame*, 136(4), 445–456.
- Juranyi, Z., Loepfe, M., Nenkov, M., & Burtscher, H. (2017). Multi-angle, dual wavelength scattering measurement chamber for the structural measurement of combustion generated particles. *Journal of Aerosol Science*, 103, 83–92.
- Kahnert, M., & Kanngießer, F. (2020). Modelling optical properties of atmospheric black carbon aerosols. *Journal of Quantitative Spectroscopy and Radiative Transfer*, 244, Article 106849.
- Kammler, H. K., Beaucage, G., Kohls, D. J., Agashe, N., & Ilavsky, J. (2005). Monitoring simultaneously the growth of nanoparticles and aggregates by in situ ultra-small-angle x-ray scattering. *Journal of Applied Physics*, 97(5), Article 054309. http://dx.doi.org/10.1063/1.1855391.
- Kanaparthi, M. A., Cevaer, S. D., & Dhaniyala, S. (2018). Towards near real-time SEMS size distribution measurements under up-scan operation. *Journal of Aerosol Science*, 126, 217–230. http://dx.doi.org/10.1016/j.jaerosci.2018.09.007.
- Kandlikar, M., & Ramachandran, G. (1999). Inverse methods for analysing aerosol spectrometer measurements: a critical review. *Journal of Aerosol Science*, 30(4), 413–437. http://dx.doi.org/10.1016/S0021-8502(98)00066-4.
- Kangasluoma, J., Cai, R., Jiang, J., Deng, C., Stolzenburg, D., Ahonen, L. R., et al. (2020). Overview of measurements and current instrumentation for 1–10 nm aerosol particle number size distributions. *Journal of Aerosol Science*, 148, Article 105584.
- Kasper, G. (1982). Hot-wire thermal precipitator with low inlet losses and low size selectivity. Review of Scientific Instruments, 53(1), 79–82. http://dx.doi.org/10.1063/1.1136821.
- Kazemimanesh, M., Moallemi, A., Thomson, K., Smallwood, G., Lobo, P., & Olfert, J. S. (2019). A novel miniature inverted-flame burner for the generation of soot nanoparticles. *Aerosol Science and Technology*, 53(2), 184–195. http://dx.doi.org/10.1080/02786826.2018.1556774.
- Kazemimanesh, M., Rahman, M. M., Duca, D., Johnson, T. J., Addad, A., Giannopoulos, G., et al. (2022). A comparative study on effective density, shape factor, and volatile mixing of non-spherical particles using tandem aerodynamic diameter, mobility diameter, and mass measurements. *Journal of Aerosol Science*, 161. Article 105930.
- Kelesidis, G. A., Goudeli, E., & Pratsinis, S. E. (2017a). Flame synthesis of functional nanostructured materials and devices: Surface growth and aggregation. Proceedings of the Combustion Institute, 36(1), 29–50. http://dx.doi.org/10.1016/j.proci.2016.08.078.
- Kelesidis, G. A., Goudeli, E., & Pratsinis, S. E. (2017b). Morphology and mobility diameter of carbonaceous aerosols during agglomeration and surface growth. *Carbon*, 121, 527–535.
- Kelesidis, G. A., Kholghy, M. R., Zuercher, J., Robertz, J., Allemann, M., Duric, A., et al. (2020). Light scattering from nanoparticle agglomerates. *Powder Technology*, 365, 52–59.
- Kelly, W., & McMurry, P. H. (1992). Measurement of particle density by inertial classification of differential mobility analyzer–generated monodisperse aerosols. Aerosol Science and Technology, 17(3), 199–212.
- Kerminen, V. M., Mäkelä, T., Hillamo, R., & Rantanen, L. (1999). Relation between particle number and mass size distribution in the diesel car exhaust. *Journal of Aerosol Science*, (30), S777–S778.
- Keskinen, J., Pietarinen, K., & Lehtimäki, M. (1992). Electrical low pressure impactor. *Journal of Aerosol Science*, 23(4), 353–360. http://dx.doi.org/10.1016/0021-8502(92)90004-F.
- Khalizov, A. F., Hogan, B., Qiu, C., Petersen, E. L., & Zhang, R. (2012). Characterization of soot aerosol produced from combustion of propane in a shock tube. Aerosol Science and Technology, 46(8), 925–936.
- Kheirkhah, P. (2020). Single-cycle exhaust soot measurement from internal combustion engines (Ph.D. thesis), University of British Columbia, http://dx.doi.org/10. 14288/1.0395397.
- Kheirkhah, P., Baldelli, A., Kirchen, P., & Rogak, S. (2020). Development and validation of a multi-angle light scattering method for fast engine soot mass and size measurements. *Aerosol Science and Technology*, 54(9), 1083–1101.
- Kholghy, M. R., Afarin, Y., Sediako, A. D., Barba, J., Lapuerta, M., Chu, C., et al. (2017). Comparison of multiple diagnostic techniques to study soot formation and morphology in a diffusion flame. *Combustion and Flame*, 176, 567–583. http://dx.doi.org/10.1016/j.combustflame.2016.11.012.
- Kholghy, M., Saffaripour, M., Yip, C., & Thomson, M. J. (2013). The evolution of soot morphology in a laminar coflow diffusion flame of a surrogate for jet A-1. Combustion and Flame, 160(10), 2119–2130.
- Kim, J. H., Mulholland, G. W., Kukuck, S. R., & Pui, D. Y. (2005). Slip correction measurements of certified PSL nanoparticles using a nanometer differential mobility analyzer (nano-DMA) for Knudsen number from 0.5 to 83. Journal of Research of the National Institute of Standards and Technology, 110(1), 31.
- King, G. B., Sorensen, C. M., Lester, T., & Merklin, J. (1982). Photon correlation spectroscopy used as a particle size diagnostic in sooting flames. *Applied Optics*, 21(6), 976–978. http://dx.doi.org/10.1364/AO.21.0976_1.

- King, G., Sorensen, C., Lester, T., & Merklin, J. (1983). Direct measurements of aerosol diffusion constants in the intermediate knudsen regime. *Physical Review Letters*, 50(15), 1125.
- Kittelson, D. B. (1998). Engines and nanoparticles: A review. Journal of Aerosol Science, 29(5), 575-588. http://dx.doi.org/10.1016/S0021-8502(97)10037-4.
- Knutson, E. O. (1999). History of diffusion batteries in aerosol measurements. Aerosol Science & Technology, 31(2-3), 83-128. http://dx.doi.org/10.1080/027868299304192
- Knutson, E., & Whitby, K. (1975). Aerosol classification by electric mobility: Apparatus, theory, and applications. *Journal of Aerosol Science*, 6(6), 443–451. http://dx.doi.org/10.1016/0021-8502(75)90060-9.
- Kohse-Höinghaus, K., Barlow, R. S., Aldén, M., & Wolfrum, J. (2005). Combustion at the focus: Laser diagnostics and control. *Proceedings of the Combustion Institute*, 30(1), 89–123. http://dx.doi.org/10.1016/j.proci.2004.08.274.
- Kondo, K., Aizawa, T., Kook, S., & Pickett, L. (2013). Uncertainty in sampling and TEM analysis of soot particles in diesel spray flame. SAE Technical Paper, 908. http://dx.doi.org/10.4271/2013-01-0908.
- Kook, S., Zhang, R., Chan, Q. N., Aizawa, T., Kondo, K., Pickett, L. M., et al. (2016). Automated detection of primary particles from transmission electron microscope (TEM) images of soot aggregates in diesel engine environments. SAE International Journal of Engines, 9(1), 279–296. http://dx.doi.org/10.4271/2015-01-1991.
- Kousis, I., Manni, M., & Pisello, A. L. (2022). Environmental mobile monitoring of urban microclimates: A review. Renewable and Sustainable Energy Reviews, 169, Article 112847. http://dx.doi.org/10.1016/j.rser.2022.112847.
- Köylü, Ü. Ö. (1997). Quantitative analysis of in situ optical diagnostics for inferring particle/aggregate parameters in flames: Implications for soot surface growth and total emissivity. *Combustion and Flame*, 109(3), 488–500. http://dx.doi.org/10.1016/S0010-2180(96)00179-4.
- Köylü, Ü. Ö., & Faeth, G. M. (1994). Optical properties of overfire soot in buoyant turbulent diffusion flames at long residence times. ournal of Heat Transfer, 116(1), 152–159. http://dx.doi.org/10.1115/1.2910849.
- Köylü, Ü. Ö., Faeth, G. M., Farias, T. L., & Carvalho, M. d. G. (1995). Fractal and projected structure properties of soot aggregates. Combustion and Flame, 100(4), 621-633
- Kroner, G., Fuchs, H., Tatschl, R., & Glatter, O. (2003). Determination of soot particle size in a diffusion flame: A dynamic light scattering study. *Aerosol Science & Technology*, 37(10), 818–827.
- Kulkarni, P., Baron, P. A., & Willeke, K. (2011). Aerosol measurement: Principles, techniques, and applications (3rd Edition). Hoboken, NJ, USA: Wiley.
- Kulkarni, P., & Wang, J. (2006). New fast integrated mobility spectrometer for real-time measurement of aerosol size distribution—I: Concept and theory. *Journal of Aerosol Science*, 37(10), 1303–1325. http://dx.doi.org/10.1016/j.jaerosci.2006.01.005.
- Kupc, A., Williamson, C., Wagner, N. L., Richardson, M., & Brock, C. A. (2018). Modification, calibration, and performance of the Ultra-High Sensitivity Aerosol Spectrometer for particle size distribution and volatility measurements during the Atmospheric Tomography Mission (ATom) airborne campaign. *Atmospheric Measurement Techniques*, 11(1), 369–383. http://dx.doi.org/10.5194/amt-11-369-2018.
- Kuwata, M., & Kondo, Y. (2009). Measurements of particle masses of inorganic salt particles for calibration of cloud condensation nuclei counters. Atmospheric Chemistry and Physics, 9(16), 5921–5932.
- Laborde, M., Mertes, P., Zieger, P., Dommen, J., Baltensperger, U., & Gysel, M. (2012). Sensitivity of the Single Particle Soot Photometer to different black carbon types. Atmospheric Measurement Techniques, 5(5), 1031–1043. http://dx.doi.org/10.5194/amt-5-1031-2012.
- Lack, D. A., Moosmüller, H., McMeeking, G. R., Chakrabarty, R. K., & Baumgardner, D. (2014). Characterizing elemental, equivalent black, and refractory black carbon aerosol particles: A review of techniques, their limitations and uncertainties. *Analytical and Bioanalytical Chemistry*, 406(1), 99–122. http://dx.doi.org/10.1007/s00216-013-7402-3.
- Ladd, W., & Wiegand, W. (1945). Electron microscope studies of colloidal carbon reticulate chain structure. Rubber Age, 57, 299–307.
- Laj, P., Bigi, A., Rose, C., Andrews, E., Lund Myhre, C., Collaud Coen, M., et al. (2020). A global analysis of climate-relevant aerosol properties retrieved from the network of Global Atmosphere Watch (GAW) near-surface observatories. Atmospheric Measurement Techniques, 13(8), 4353–4392. http://dx.doi.org/10. 5194/amt-13-4353-2020.
- Lamprecht, A., Eimer, W., & Kohse-Höinghaus, K. (1999). Dynamic light scattering in sooting premixed atmospheric-pressure methane-, propane-, ethene-, and propene-oxygen flames. *Combustion and Flame*, 118(1-2), 140-150.
- Lapuerta, M., Ballesteros, R., & Martos, F. J. (2006). A method to determine the fractal dimension of diesel soot agglomerates. *Journal of Colloid and Interface Science*, 303(1), 149–158.
- Leavey, A., Fang, J., Sahu, M., & Biswas, P. (2013). Comparison of measured particle lung deposited surface area concentrations by an Aerotrak 9000 using size distribution measurements for a range of combustion aerosols. *Aerosol Science and Technology*, 47(9), 966–978. http://dx.doi.org/10.1080/02786826.2013. 803018.
- Lee, K. O., Cole, R., Sekar, R., Choi, M. Y., Kang, J. S., Bae, C. S., et al. (2002). Morphological investigation of the microstructure, dimensions, and fractal geometry of diesel particulates. *Proceedings of the Combustion Institute*, 29(1), 647–653. http://dx.doi.org/10.1016/S1540-7489(02)80083-9.
- Lee, K., & Liu, B. (1980). On the minimum efficiency and the most penetrating particle size for fibrous filters. *Journal of the Air Pollution Control Association*, 30(4), 377–381.
- Leung, K. K., Schnitzler, E. G., Dastanpour, R., Rogak, S. N., Jäger, W., & Olfert, J. S. (2017). Relationship between coating-induced soot aggregate restructuring and primary particle number. *Environmental Science and Technology*, 51(15), 8376–8383. http://dx.doi.org/10.1021/acs.est.7b01140.
- Leung, K. K., Schnitzler, E. G., Jäger, W., & Olfert, J. S. (2017). Relative humidity dependence of soot aggregate restructuring induced by secondary organic aerosol: Effects of water on coating viscosity and surface tension. *Environmental Science & Technology Letters*, 4(9), 386–390. http://dx.doi.org/10.1021/acs.
- Li, C., Lee, A. L., Chen, X., Pomerantz, W. C., Haynes, C. L., & Hogan Jr., C. J. (2020). Multidimensional nanoparticle characterization through ion mobility-mass spectrometry. *Analytical Chemistry*, 92(3), 2503–2510.
- Li, M., Mulholland, G. W., & Zachariah, M. R. (2016). The effect of alignment on the electric mobility of soot. *Aerosol Science and Technology*, 50(10), 1003–1016. Li, S., Ren, Y., Biswas, P., & Stephen, D. T. (2016). Flame aerosol synthesis of nanostructured materials and functional devices: Processing, modeling, and
- Li, S., Ren, Y., Biswas, P., & Stephen, D. T. (2016). Flame aerosol synthesis of nanostructured materials and functional devices: Processing, modeling, and diagnostics. *Progress in Energy and Combustion Science*, 55, 1–59.
- Li, W., Shao, L., Zhang, D., Ro, C. U., Hu, M., Bi, X., et al. (2016). A review of single aerosol particle studies in the atmosphere of east Asia: Morphology, mixing state, source, and heterogeneous reactions. *Journal of Cleaner Production*, 112, 1330–1349.
- Liao, J. Y., Selomulya, C., Bushell, G., Bickert, G., & Amal, R. (2005). On different approaches to estimate the mass fractal dimension of coal aggregates. *Particle & Particle Systems Characterization*, 22(5), 299–309. http://dx.doi.org/10.1002/ppsc.200500978.
- Liati, A., & Dimopoulos Eggenschwiler, P. (2010). Characterization of particulate matter deposited in diesel particulate filters: Visual and analytical approach in macro-, micro- and nano-scales. *Combustion and Flame*, 157(9), 1658–1670. http://dx.doi.org/10.1016/j.combustflame.2010.02.015.
- Lide, D. R. (1992). CRC handbook of chemistry and physics. Boca Raton: CRC Press.
- Lienert, B., Porter, J., & Sharma, S. (2003). Aerosol size distributions from genetic inversion of polar nephelometer data. *Journal of Atmospheric and Oceanic Technology*, 20(10), 1403–1410.
- Liggio, J., Gordon, M., Smallwood, G., Li, S. M., Stroud, C., Staebler, R., et al. (2012). Are emissions of black carbon from gasoline vehicles underestimated? Insights from near and on-road measurements. *Environmental Science and Technology*, 46(9), 4819–4828. http://dx.doi.org/10.1021/es2033845.

- Lighty, J. S., Veranth, J. M., & Sarofim, A. F. (2000). Combustion aerosols: Factors governing their size and composition and implications to human health. Journal of the Air & Waste Management Association, 50(9), 1565–1618. http://dx.doi.org/10.1080/10473289.2000.10464197.
- Lin, M., Klein, R., Lindsay, H., Weitz, D. A., Ball, R. C., & Meakin, P. (1990). The structure of fractal colloidal aggregates of finite extent. *Journal of Colloid and Interface Science*, 137(1), 263–280.
- Link, O., Snelling, D., Thomson, K., & Smallwood, G. (2011). Development of absolute intensity multi-angle light scattering for the determination of polydisperse soot aggregate properties. *Proceedings of the Combustion Institute*, 33(1), 847–854. http://dx.doi.org/10.1016/j.proci.2010.06.073.
- Liu, C. (2019). Optical properties of black carbon aggregates. Springer Series in Light Scattering: Volume 3: Radiative Transfer and Light Scattering, 167-218.
- Liu, B. Y., Berglund, R. N., & Agarwal, J. K. (1974). Experimental studies of optical particle counters. Atmospheric Environment (1967), 8(7), 717-732.
- Liu, P., & Chakrabarty, R. K. (2016). Sensitivity analysis of aggregate morphology on mass-mobility relationship and improved parameterizations. *Aerosol Science and Technology*, 50(1), 63–70. http://dx.doi.org/10.1080/02786826.2015.1122737.
- Liu, C., Chung, C. E., Yin, Y., & Schnaiter, M. (2018). The absorption Ångström exponent of black carbon: From numerical aspects. Atmospheric Chemistry and Physics, 18(9), 6259–6273.
- Liu, L., & Mishchenko, M. I. (2005). Effects of aggregation on scattering and radiative properties of soot aerosols. *Journal of Geophysical Research*, 110(D11), http://dx.doi.org/10.1029/2004jd005649.
- Liu, B., Pui, D., Whitby, K., Kittelson, D. B., Kousaka, Y., & McKenzie, R. (1978). The aerosol mobility chromatograph: A new detector for sulfuric acid aerosols. In Sulfur in the atmosphere (pp. 99–104). Elsevier, http://dx.doi.org/10.1016/0004-6981(78)90192-0.
- Liu, Y., Song, C., Lv, G., Chen, N., Zhou, H., & Jing, X. (2018). Determination of the attractive force, adhesive force, adhesion energy and Hamaker constant of soot particles generated from a premixed methane/oxygen flame by AFM. Applied Surface Science, 433, 450–457.
- Liu, D., Whitehead, J., Alfarra, M. R., Reyes-Villegas, E., Spracklen, D. V., Reddington, C. L., et al. (2017). Black-carbon absorption enhancement in the atmosphere determined by particle mixing state. *Nature Geoscience*, 10(3), 184–188.
- Liu, F., Wong, C., Snelling, D. R., & Smallwood, G. J. (2013b). Investigation of absorption and scattering properties of soot aggregates of different fractal dimension at 532 nm using RDG and GMM. Aerosol Science and Technology, 47(12), 1393–1405.
- Liu, F., Yang, M., Hill, F. A., Snelling, D. R., & Smallwood, G. J. (2006). Influence of polydisperse distributions of both primary particle and aggregate size on soot temperature in low-fluence LII. Applied Physics B, 83, 383–395.
- Liu, F., Yon, J., & Bescond, A. (2016). On the radiative properties of soot aggregates—Part 2: Effects of coating. *Journal of Quantitative Spectroscopy and Radiative Transfer*, 172, 134–145.
- Liu, F., Yon, J., Fuentes, A., Lobo, P., Smallwood, G. J., & Corbin, J. C. (2020). Review of recent literature on the light absorption properties of black carbon: Refractive index, mass absorption cross section, and absorption function. *Aerosol Science and Technology*, 54(1), 33–51.
- Liu, J., Zhang, Q., Wang, J., & Zhang, Y. (2020). Light scattering matrix for soot aerosol: Comparisons between experimental measurements and numerical simulations. Journal of Quantitative Spectroscopy and Radiative Transfer, 246, Article 106946.
- Liu, P., Ziemann, P. J., Kittelson, D. B., & McMurry, P. H. (1995a). Generating particle beams of controlled dimensions and divergence: I. Theory of particle motion in aerodynamic lenses and nozzle expansions. Aerosol Science and Technology, 22(3), 293–313. http://dx.doi.org/10.1080/02786829408959748.
- Liu, P., Ziemann, P. J., Kittelson, D. B., & McMurry, P. H. (1995b). Generating particle beams of controlled dimensions and divergence: II. Experimental evaluation of particle motion in aerodynamic lenses and nozzle expansions. *Aerosol Science and Technology*, 22(3), 314–324. http://dx.doi.org/10.1080/02786829408959749, arXiv:10.1080/02786829408959749.
- Loh, N. D., Hampton, C. Y., Martin, A. V., Starodub, D., Sierra, R. G., Barty, A., et al. (2012). Fractal morphology, imaging and mass spectrometry of single aerosol particles in flight. *Nature*, 486, 513–517. http://dx.doi.org/10.1038/nature11222.
- Luo, J., Zhang, Y., Wang, F., Wang, J., & Zhang, Q. (2018). Applying machine learning to estimate the optical properties of black carbon fractal aggregates. Journal of Quantitative Spectroscopy and Radiative Transfer, 215, 1–8.
- Ma, L. (2011). Analysis of error in soot characterization using scattering-based techniques. Particuology, 9(3), 210–214. http://dx.doi.org/10.1016/j.partic.2011. 02.002.
- Ma, L., Kranendonk, L., Cai, W., Zhao, Y., & Baba, J. (2009). Application of simulated annealing for simultaneous retrieval of particle size distribution and refractive index. *Journal of Aerosol Science*, 40(7), 588–596.
- Ma, B., & Long, M. B. (2014). Combined soot optical characterization using 2-D multi-angle light scattering and spectrally resolved line-of-sight attenuation and its implication on soot color-ratio pyrometry. *Applied Physics B*, 117, 287–303. http://dx.doi.org/10.1007/s00340-014-5834-x.
- Mai, H., & Flagan, R. C. (2018). Scanning DMA data analysis I. Classification transfer function. Aerosol Science and Technology, 52(12), 1382–1399. http://dx.doi.org/10.1080/02786826.2018.1528005.
- Malmborg, V. B., Eriksson, A. C., Török, S., Zhang, Y., Kling, K., Martinsson, J., et al. (2019). Relating aerosol mass spectra to composition and nanostructure of soot particles. *Carbon*, 142, 535–546. http://dx.doi.org/10.1016/j.carbon.2018.10.072.
- Mandelbrot, B. (1977). Fractals: Form, Chance, and Dimension. San Francisco: W. H. Freeman and Company, http://dx.doi.org/10.1002/zamm.19790590830.
- Mao, J., & Li, J. (2014). Dust particle size distribution inversion based on the multi population genetic algorithm. TAO: Terrestrial, Atmospheric and Oceanic Sciences, 25(6), 791. http://dx.doi.org/10.3319/TAO.2014.06.12.01(A).
- Maricq, M. M., Podsiadlik, D. H., & Chase, R. E. (2000). Size distributions of motor vehicle exhaust PM: A comparison between ELPI and SMPS measurements. Aerosol Science and Technology, 33(3), 239–260. http://dx.doi.org/10.1080/027868200416231.
- Maricq, M. M., Xu, N., & Chase, R. E. (2006). Measuring particulate mass emissions with the electrical low pressure impactor. Aerosol Science and Technology, 40(1), 68–79. http://dx.doi.org/10.1080/02786820500466591.
- Markowski, G. R. (1987). Improving Twomey's algorithm for inversion of aerosol measurement data. Aerosol Science and Technology, 7(2), 127-141.
- Marple, V. A., & Liu, B. Y. H. (1974). Characteristics of laminar jet impactors. *Environmental Science and Technology*, 8(7), 648–654. http://dx.doi.org/10.1021/es60092a003.
- Marra, J., Voetz, M., & Kiesling, H. J. (2010). Monitor for detecting and assessing exposure to airborne nanoparticles. *Journal of Nanoparticle Research*, 12(1), 21–37. http://dx.doi.org/10.1007/s11051-009-9695-x.
- Martin, J. W., Salamanca, M., & Kraft, M. (2022). Soot inception: Carbonaceous nanoparticle formation in flames. *Progress in Energy and Combustion Science*, 88, Article 100956.
- Martin, J. E., Schaefer, D. W., & Hurd, A. J. (1986). Fractal geometry of vapor-phase aggregates. Physical Review A, 33(5), 3540.
- Martins, F. J., Kronenburg, A., & Beyrau, F. (2021). Single-shot two-dimensional multi-angle light scattering (2D-MALS) technique for nanoparticle aggregate sizing. Applied Physics B, 127, 1–15.
- Masel, R. I. (1996). Principles of adsorption and reaction on solid surfaces, Vol. 3. John Wiley & Sons.
- Massabò, D., Bernardoni, V., Bove, M. C., Brunengo, A., Cuccia, E., Piazzalunga, A., et al. (2013). A multi-wavelength optical set-up for the characterization of carbonaceous particulate matter. *Journal of Aerosol Science*, 60, 34–46. http://dx.doi.org/10.1016/j.jaerosci.2013.02.006.
- Matuschek, G., Karg, E., Schröppel, A., Schulz, H., & Schmid, O. (2007). Chemical investigation of eight different types of carbonaceous particles using thermoanalytical techniques. *Environmental Science and Technology*, 41(24), 8406–8411. http://dx.doi.org/10.1021/es062660v.
- McMurry, P. H. (2000). A review of atmospheric aerosol measurements. Atmospheric Environment, 34(12-14), 1959-1999.
- McMurry, P. H., Litchy, M., Huang, P.-F., Cai, X., Turpin, B. J., Dick, W. D., et al. (1996). Elemental composition and morphology of individual particles separated by size and hygroscopicity with the TDMA. Atmospheric Environment, 30(1), 101–108.

- McMurry, P. H., & Stolzenburg, M. R. (1989). On the sensitivity of particle size to relative humidity for Los Angeles aerosols. Atmospheric Environment (1967), 23(2), 497–507, http://dx.doi.org/10.1016/0004-6981(89)90593-3.
- McMurry, P. H., Takano, H., & Anderson, G. R. (1983). Study of the ammonia (gas)-sulfuric acid (aerosol) reaction rate. *Environmental Science and Technology*, 17(6), 347–352.
- McMurry, P. H., Wang, X., Park, K., & Ehara, K. (2002). The relationship between mass and mobility for atmospheric particles: A new technique for measuring particle density. *Aerosol Science & Technology*, 36(2), 227–238. http://dx.doi.org/10.1080/027868202753504083.
- Meakin, P. (1987). Fractal aggregates. Advances in Colloid and Interface Science, 28, 249–331. http://dx.doi.org/10.1016/0001-8686(87)80016-7, URL https://www.sciencedirect.com/science/article/pii/0001868687800167.
- Meakin, P. (1999). A historical introduction to computer models for fractal aggregates. Journal of Sol-Gel Science and Technology, 15, 97–117. http://dx.doi.org/10.1023/A:1008731904082.
- Meakin, P., Donn, B., & Mulholland, G. W. (1989). Collisions between point masses and fractal aggregates. Langmuir, 5(2), 510–518. http://dx.doi.org/10.1021/
- Medalia, A., & Heckman, F. (1971). Morphology of aggregates: VII. Comparison chart method for electron microscopic determination of carbon black aggregate morphology. *Journal of Colloid and Interface Science*, 36(2), 173–190. http://dx.doi.org/10.1016/0021-9797(71)90162-7.
- Mei, F., McMeeking, G., Pekour, M., Gao, R. S., Kulkarni, G., China, S., et al. (2020). Performance assessment of Portable Optical Particle Spectrometer (Pops). Sensors, 20(21), 6294. http://dx.doi.org/10.3390/s20216294.
- Melas, A. D., Isella, L., Konstandopoulos, A. G., & Drossinos, Y. (2014). Morphology and mobility of synthetic colloidal aggregates. *Journal of Colloid and Interface Science*, 417, 27–36. http://dx.doi.org/10.1016/j.jcis.2013.11.024.
- Menser, J., Daun, K., Dreier, T., & Schulz, C. (2016). Laser-induced incandescence from laser-heated silicon nanoparticles. Applied Physics B, 122, 1-15.
- Mertes, S., Schröder, F., & Wiedensohler, A. (1995). The particle detection efficiency curve of the TSI-3010 CPC as a function of the temperature difference between saturator and condenser. Aerosol Science and Technology, 23(2), 257–261. http://dx.doi.org/10.1080/02786829508965310.
- Meyer, T. R., Halls, B. R., Jiang, N., Slipchenko, M. N., Roy, S., & Gord, J. R. (2016). High-speed, three-dimensional tomographic laser-induced incandescence imaging of soot volume fraction in turbulent flames. *Optics Express*, 24(26), 29547–29555.
- Michelsen, H. A. (2006). Laser-induced incandescence of flame-generated soot on a picosecond time scale. Applied Physics B, 83, 443-448.
- Michelsen, H. (2017). Probing soot formation, chemical and physical evolution, and oxidation: A review of in situ diagnostic techniques and needs. *Proceedings* of the Combustion Institute, 36(1), 717–735.
- Michelsen, H. A., Campbell, M. F., Johansson, K. O., Tran, I. C., Schrader, P. E., Bambha, R. P., et al. (2022). Soot-particle core-shell and fractal structures from small-angle X-ray scattering measurements in a flame. Carbon, 196, 440–456.
- Michelsen, H. A., Campbell, M. F., Tran, I. C., Johansson, K. O., Schrader, P. E., Bambha, R. P., et al. (2022). Distinguishing gas-phase and nanoparticle contributions to small-angle x-ray scattering in reacting aerosol flows. *The Journal of Physical Chemistry A*, 126(19), 3015–3026.
- Michelsen, H. A., Colket, M. B., Bengtsson, P. E., D'anna, A., Desgroux, P., Haynes, B. S., et al. (2020). A review of terminology used to describe soot formation and evolution under combustion and pyrolytic conditions. ACS Nano, 14(10), 12470–12490.
- Michelsen, H. A., Liu, F., Kock, B. F., Bladh, H., Boïarciuc, A., Charwath, M., et al. (2007). Modeling laser-induced incandescence of soot: A summary and comparison of LII models. *Applied Physics B*, 87, 503–521.
- Michelsen, H., Schulz, C., Smallwood, G., & Will, S. (2015). Laser-induced incandescence: Particulate diagnostics for combustion, atmospheric, and industrial
- applications. *Progress in Energy and Combustion Science*, 51, 2–48.

 Migliorini, F., Belmuso, S., Ciniglia, D., Dondè, R., & De Iuliis, S. (2022). A double pulse LII experiment on carbon nanoparticles: insight into optical properties. *Physical Chemistry Chemical Physics*, 24(33), 19837–19843.
- Miller, A., Frey, G., King, G., & Sunderman, C. (2010). A handheld electrostatic precipitator for sampling airborne particles and nanoparticles. Aerosol Science and Technology, 44(6), 417–427. http://dx.doi.org/10.1080/02786821003692063.
- Mirzaei, M., & Rafsanjani, H. K. (2017). An automatic algorithm for determination of the nanoparticles from tem images using circular hough transform. *Micron*, 96. 86–95. http://dx.doi.org/10.1016/j.micron.2017.02.008.
- Mishchenko, M. I. (2009). Electromagnetic scattering by nonspherical particles: A tutorial review. *Journal of Quantitative Spectroscopy and Radiative Transfer*, 110(11), 808–832. http://dx.doi.org/10.1016/j.jqsrt.2008.12.005.
- Mishchenko, M. I., Travis, L. D., & Mackowski, D. W. (1996). T-matrix computations of light scattering by nonspherical particles: A review. *Journal of Quantitative*
- Spectroscopy and Radiative Transfer, 55(5), 535–575.

 Mitchell, J., Di Stasio, S., LeGarrec, J. L., Florescu-Mitchell, A. I., Narayanan, T., & Sztucki, M. (2009). Small angle x-ray scattering study of flame soot nanoparticle
- aggregation and restructuring. *Journal of Applied Physics*, 105(12), Article 124904.

 Mitchell, J., Le Garrec, J. L., Florescu-Mitchell, A. I., & Di Stasio, S. (2006). Small-angle neutron scattering study of soot particles in an ethylene–air diffusion flame. *Combustion and Flame*, 145(1–2), 80–87.
- Mitchell, J. B. A., LeGarrec, J. L., Saidani, G., Lefeuvre, F., & Di Stasio, S. (2013). Synchrotron radiation studies of additives in combustion, III: Ferrocene. *Energy & Fuels*, 27(8), 4891–4898. http://dx.doi.org/10.1021/ef400758a.
- Moallemi, A., Kazemimanesh, M., Corbin, J. C., Thomson, K., Smallwood, G., Olfert, J. S., et al. (2019). Characterization of black carbon particles generated by a propane-fueled miniature inverted soot generator. *Journal of Aerosol Science*, 135, 46–57. http://dx.doi.org/10.1016/j.jaerosci.2019.05.004.
- Moallemi, A., Modini, R. L., Lapyonok, T., Lopatin, A., Fuertes, D., Dubovik, O., et al. (2022). Information content and aerosol property retrieval potential for different types of in situ polar nephelometer data. *Atmospheric Measurement Techniques*, 15(19), 5619–5642. http://dx.doi.org/10.5194/amt-15-5619-2022.
- Modini, R. L., Corbin, J. C., Brem, B. T., Irwin, M., Bertò, M., Pileci, R. E., et al. (2021). Detailed characterization of the CAPS single-scattering albedo monitor (CAPS PMssa) as a field-deployable instrument for measuring aerosol light absorption with the extinction-minus-scattering method. *Atmospheric Measurement Techniques*. 14(2), 819–851.
- Moghaddam, S. T., Hadwin, P. J., & Daun, K. J. (2017). Soot aggregate sizing through multiangle elastic light scattering: Influence of model error. *Journal of Aerosol Science*, 111, 36-50.
- Moore, R. H., Wiggins, E. B., Ahern, A. T., Zimmerman, S., Montgomery, L., Campuzano Jost, P., et al. (2021). Sizing response of the Ultra-High Sensitivity Aerosol Spectrometer (UHSAS) and Laser Aerosol Spectrometer (LAS) to changes in submicron aerosol composition and refractive index. Atmospheric Measurement Techniques, 14(6), 4517–4542. http://dx.doi.org/10.5194/amt-14-4517-2021.
- Moore, R. H., Wiggins, E. B., Wiggins, A. T., Zimmerman, S., Montgomery, L., Campuzano Jost, P., et al. (2021). Sizing response of the ultra-high sensitivity aerosol spectrometer (UHSAS) and laser aerosol spectrometer (LAS) to changes in submicron aerosol composition and refractive index. *Atmospheric Measurement Techniques*, 14(6), 4517–4542. http://dx.doi.org/10.5194/amt-14-4517-2021.
- Moosmüller, H., Chakrabarty, R. K., & Arnott, W. P. (2009). Aerosol light absorption and its measurement: A review. *Journal of Quantitative Spectroscopy and Radiative Transfer*, 110(11), 844–878. http://dx.doi.org/10.1016/j.jqsrt.2009.02.035.
- Moosmüller, H., Chakrabarty, R., Ehlers, K., & Arnott, W. (2011). Absorption Ångström coefficient, brown carbon, and aerosols: Basic concepts, bulk matter, and spherical particles. Atmospheric Chemistry and Physics, 11(3), 1217–1225.
- Morán, J., Li, L., Ouyang, H., Qiao, Y., Olson, B. A., & Hogan Jr., C. J. (2023). Characterization of the bidimensional size and charge distribution of sub-and supermicrometer particles in an electrostatic precipitator. *Powder Technology*, Article 118578.
- Morán, J., Yon, J., & Poux, A. (2020). Monte carlo aggregation code (MCAC) Part 1: Fundamentals. Journal of Colloid and Interface Science, 569, 184-194.

- Morán, J., Yon, J., Poux, A., Corbin, F., Ouf, F. X., & Siméon, A. (2020). Monte Carlo aggregation code (MCAC) Part 2: Application to soot agglomeration, highlighting the importance of primary particles. *Journal of Colloid and Interface Science*, 575, 274–285. http://dx.doi.org/10.1016/j.jcis.2020.04.085.
- Moteki, N., Adachi, K., Ohata, S., Yoshida, A., Harigaya, T., Koike, M., et al. (2017). Anthropogenic iron oxide aerosols enhance atmospheric heating. *Nature Communications*. 8(15329). 1–11. http://dx.doi.org/10.1038/ncomms15329.
- Moteki, N., & Kondo, Y. (2007). Effects of Mixing State on Black Carbon Measurements by Laser-Induced Incandescence. Aerosol Science and Technology, 41(4), 398–417. http://dx.doi.org/10.1080/02786820701199728.
- Moteki, N., Ohata, S., Yoshida, A., & Adachi, K. (2023). Constraining the complex refractive index of black carbon particles using the complex forward-scattering amplitude. *Aerosol Science and Technology*, (just-accepted), 1–21.
- Mountain, R. D., Mulholland, G. W., & Baum, H. (1986). Simulation of aerosol agglomeration in the free molecular and continuum flow regimes. *Journal of Colloid and Interface Science*, 114(1), 67–81. http://dx.doi.org/10.1016/0021-9797(86)90241-9.
- Müller, J. O., Su, D. S., Wild, U., & Schlögl, R. (2007). Bulk and surface structural investigations of diesel engine soot and carbon black. *Physical Chemistry Chemical Physics*, 9(30), 4018–4025.
- Mullins, J., & Williams, A. (1987). The optical properties of soot: A comparison between experimental and theoretical values. Fuel, 66(2), 277–280. http://dx.doi.org/10.1016/0016-2361(87)90255-9.
- Nakagawa, M., Nakayama, T., Sasago, H., Ueda, S., Venables, D. S., & Matsumi, Y. (2016). Design and characterization of a novel single-particle polar nephelometer. *Aerosol Science and Technology*, 50(4), 392–404. http://dx.doi.org/10.1080/02786826.2016.1155105.
- Naseem, T., & Durrani, T. (2021). The role of some important metal oxide nanoparticles for wastewater and antibacterial applications: A review. Environmental Chemistry and Ecotoxicology, 3, 59–75. http://dx.doi.org/10.1016/j.enceco.2020.12.001.
- Naseri, A., Sipkens, T., Rogak, S., & Olfert, J. (2021). An improved inversion method for determining two-dimensional mass distributions of non-refractory materials on refractory black carbon. *Aerosol Science and Technology*, 55(1), 104–118.
- Naseri, A., Sipkens, T., Rogak, S., & Olfert, J. (2022). Optimized instrument configurations for tandem particle mass analyzer and single particle-soot photometer experiments. *Journal of Aerosol Science*, 160, Article 105897.
- Nie, X., & Mao, Q. (2022). Inversion of aerosol particle size distribution using an improved stochastic particle swarm optimization algorithm. *Remote Sensing*, 14(16), 4085.
- Nishida, R. T., Johnson, T. J., Boies, A. M., & Hochgreb, S. (2019a). Measuring aerosol active surface area by direct ultraviolet photoionization and charge capture in continuous flow. Aerosol Science and Technology, 53(12), 1429–1440. http://dx.doi.org/10.1080/02786826.2019.1661958.
- Nishida, R. T., Johnson, T. J., Boies, A. M., & Hochgreb, S. (2019b). Measuring aerosol active surface area by direct ultraviolet photoionization and charge capture in continuous flow. Aerosol Science and Technology, 53(12), 1429–1440. http://dx.doi.org/10.1080/02786826.2019.1661958.
- Nishida, R., Johnson, T., Hassim, J., Graves, B., Boies, A., & Hochgreb, S. (2020). A simple method for measuring fine-to-ultrafine aerosols using bipolar charge equilibrium. ACS Sensors, 5(2), 447–453. http://dx.doi.org/10.1021/acssensors.9b02143.
- Ochoterena, R., Andersson, M., & Andersson, S. (2020). Apparent soot size and concentration in combusting diesel jets at high gas pressures and temperatures measured by combining quasi-simultaneous LII, elastic light scattering and light extinction. SAE International Journal of Advances and Current Practices in Mobility, 2(2020-01-0787), 1578–1591.
- Oh, C., & Sorensen, C. (1997). The effect of overlap between monomers on the determination of fractal cluster morphology. *Journal of Colloid and Interface Science*, 193(1), 17–25. http://dx.doi.org/10.1006/jcis.1997.5046.
- Olfert, J., & Collings, N. (2005). New method for particle mass classification The couette centrifugal particle mass analyzer. *Journal of Aerosol Science*, 36, 1338–1352. http://dx.doi.org/10.1016/j.jaerosci.2005.03.006.
- Olfert, J. S., Dickau, M., Momenimovahed, A., Saffaripour, M., Thomson, K., Smallwood, G., et al. (2017). Effective density and volatility of particles sampled from a helicopter gas turbine engine. Aerosol Science and Technology, 51(6), 704-714.
- Olfert, J. S., Kulkarni, P., & Wang, J. (2008). Measuring aerosol size distributions with the fast integrated mobility spectrometer. *Journal of Aerosol Science*, 39(11), 940–956. http://dx.doi.org/10.1016/j.jaerosci.2008.06.005.
- Olfert, J., & Rogak, S. (2019). Universal relations between soot effective density and primary particle size for common combustion sources. *Aerosol Science and Technology*, 53(5), 485–492. http://dx.doi.org/10.1080/02786826.2019.1577949.
- Olfert, J., Symonds, J., & Collings, N. (2007). The effective density and fractal dimension of particles emitted from a light-duty diesel vehicle with a diesel oxidation catalyst. *Journal of Aerosol Science*, 38(1), 69–82.
- Olfert, J. S., & Wang, J. (2009). Dynamic characteristics of a fast-response aerosol size spectrometer. Aerosol Science and Technology, 43(2), 97–111. http://dx.doi.org/10.1080/02786820802495488.
- Olofsson, N. E., Johnsson, J., Bladh, H., & Bengtsson, P. E. (2013). Soot sublimation studies in a premixed flat flame using laser-induced incandescence (LII) and elastic light scattering (ELS). Applied Physics B, 112, 333–342.
- Olofsson, N. E., Simonsson, J., Török, S., Bladh, H., & Bengtsson, P. E. (2015). Evolution of properties for aging soot in premixed flat flames studied by laser-induced incandescence and elastic light scattering. *Applied Physics B*, 119, 669–683.
- Oltmann, H., Reimann, J., & Will, S. (2010). Wide-angle light scattering (WALS) for soot aggregate characterization. *Combustion and Flame*, 157(3), 516–522. http://dx.doi.org/10.1016/j.combustflame.2009.10.011.
- Oltmann, H., Reimann, J., & Will, S. (2012). Single-shot measurement of soot aggregate sizes by wide-angle light scattering (WALS). Applied Physics B, 106, 171–183.
- Orhan, O., Haffner-Staton, E., La Rocca, A., & Fay, M. (2016). Characterisation of flame-generated soot and soot-in-oil using electron tomography volume reconstructions and comparison with traditional 2D-TEM measurements. *Tribology International*, 104, 272–284. http://dx.doi.org/10.1016/j.triboint.2016.09.
- Orsini, D., Wiedensohler, A., Stratmann, F., & Covert, D. (1999). A new volatility tandem differential mobility analyzer to measure the volatile sulfuric acid aerosol fraction. *Journal of Atmospheric and Oceanic Technology*, 16(6), 760–772.
- Ossler, F., Canton, S. E., & Larsson, J. (2009). X-ray scattering studies of the generation of carbon nanoparticles in flames and their transition from gas phase to condensed phase. *Carbon*, 47(15), 3498–3507.
- Ossler, F., Vallenhag, L., Canton, S. E., Mitchell, J. B. A., Le Garrec, J. L., Sztucki, M., et al. (2013). Dynamics of incipient carbon particle formation in a stabilized ethylene flame by in situ extended-small-angle-and wide-angle X-ray scattering. Carbon, 51, 1–19.
- Otsu, N. (1979). A threshold selection method from gray-level histograms. IEEE Transactions on Systems, Man, and Cybernetics, 9(1), 62-66.
- Ouf, F. X., Bourrous, S., Fauvel, S., Kort, A., Lintis, L., Nuvoli, J., et al. (2019a). True density of combustion emitted particles: a comparison of results highlighting the influence of the organic contents. *Journal of Aerosol Science*, 134, 1–13.
- Ouf, F. X., Bourrous, S., Vallières, C., Yon, J., & Lintis, L. (2019b). Specific surface area of combustion emitted particles: Impact of primary particle diameter and organic content. *Journal of Aerosol Science*, 137, http://dx.doi.org/10.1016/J.JAEROSCI.2019.105436.
- Ouf, F. X., Yon, J., Ausset, P., Coppalle, A., & Maillé, M. (2010). Influence of sampling and storage protocol on fractal morphology of soot studied by transmission electron microscopy. Aerosol Science and Technology, 44(11), 1005–1017. http://dx.doi.org/10.1080/02786826.2010.507228.
- Oxford, C. R., Chakrabarty, R. K., & Williams, B. J. (2022). Evaluation of assumptions made by hygroscopic tandem differential mobility analyzer inversion routines. *Journal of Aerosol Science*, 162, Article 105955.

- Pagels, J., Khalizov, A. F., McMurry, P. H., & Zhang, R. Y. (2009). Processing of soot by controlled sulphuric acid and water condensation—Mass and mobility relationship. Aerosol Science and Technology, 43(7), 629–640.
- Palazzo, N., Kögl, M., Bauer, P., Mannazhi, M. N., Zigan, L., Huber, F. J. T., et al. (2019). Investigation of soot formation in a novel diesel fuel burner. *Energies*, 12(10), 1993.
- Palazzo, N., Zigan, L., Huber, F. J., & Will, S. (2020). Impact of oxygenated additives on soot properties during diesel combustion. Energies, 14(1), 147.
- Pan, Y. L., Aptowicz, K., Arnold, J., Cheng, S., Kalume, A., Piedra, P., et al. (2022). Review of elastic light scattering from single aerosol particles and application in bioaerosol detection. *Journal of Quantitative Spectroscopy and Radiative Transfer*, Article 108067.
- Pan, X., Liu, H., Wu, Y., Tian, Y., Sun, Y., Xie, C., et al. (2019). Dynamic shape factor and mixing state of refractory black carbon particles in winter in Beijing using an AAC-DMA-SP2 tandem system. Atmospheric Chemistry and Physics Discussions, 1–31.
- Pang, Y., Wang, Y., Wang, Z., Zhang, Y., Liu, L., Kong, S., et al. (2022). Quantifying the fractal dimension and morphology of individual atmospheric soot aggregates. *Journal of Geophysical Research: Atmospheres*, 127(5), e2021JD036055.
- Park, K., Cao, F., Kittelson, D. B., & McMurry, P. H. (2003). Relationship between particle mass and mobility for diesel exhaust particles. *Environmental Science and Technology*, 37(3), 577–583.
- Park, K., Dutcher, D., Emery, M., Pagels, J., Sakurai, H., Scheckman, J., et al. (2008). Tandem measurements of aerosol properties—A review of mobility techniques with extensions. Aerosol Science and Technology, 42(10), 801–816.
- Park, C., Huang, J. Z., Ji, J. X., & Ding, Y. (2012). Segmentation, inference and classification of partially overlapping nanoparticles. *IEEE Transactions on Pattern Analysis and Machine Intelligence*, 35(3), 1.
- Park, K., Kittelson, D. B., & McMurry, P. H. (2003). A closure study of aerosol mass concentration measurements: comparison of values obtained with filters and by direct measurements of mass distributions. *Atmospheric Environment*. 37(9–10), 1223–1230.
- Park, K., Kittelson, D. B., & McMurry, P. H. (2004). Structural properties of diesel exhaust particles measured by transmission electron microscopy (TEM): Relationships to particle mass and mobility. Aerosol Science and Technology, 38(9), 881–889.
- Park, K., Kittelson, D. B., Zachariah, M. R., & McMurry, P. H. (2004). Measurement of inherent material density of nanoparticle agglomerates. *Journal of Nanoparticle Research*, 6(2), 267–272. http://dx.doi.org/10.1023/B:NANO.000034657.71309.e6.
- Paz, C., Cabarcos, A., Conde, M., & Gil, C. (2022). Comparison of characteristics evaluated by different fractal approaches of soot agglomerates produced by a combustion aerosol generator. Experimental Thermal and Fluid Science, 136, Article 110662. http://dx.doi.org/10.1016/j.expthermflusci.2022.110662.
- Paz, C., Cabarcos, A., Vence, J., & Gil, C. (2022). Development of an active contour based algorithm to perform the segmentation of soot agglomerates in uneven illumination TEM imaging. *Powder Technology*, 400, Article 117260.
- Peng, L., Li, Z., Zhang, G., Bi, X., Hu, W., Tang, M., et al. (2021). A review of measurement techniques for aerosol effective density. Science of the Total Environment, 778, Article 146248.
- Penner, S., Bernard, J., & Jerskey, T. (1976a). Laser scattering from moving, polydisperse particles in flames—II. preliminary experiments. *Acta Astronautica*, 3(1–2), 93–105.
- Penner, S., Bernard, J., & Jerskey, T. (1976b). Power spectra observed in laser scattering from moving, polydisperse particle systems in flames—I. Theory. Acta
- Astronautica, 3(1-2), 69-91.

 Petters, M. D. (2018). A language to simplify computation of differential mobility analyzer response functions. Aerosol Science and Technology, 52(12), 1437-1451.
- Petters, M. D. (2021). Revisiting matrix-based inversion of scanning mobility particle sizer (SMPS) and humidified tandem differential mobility analyzer (HTDMA) data. *Atmospheric Measurement Techniques*, 14(12), 7909–7928.

 Petzold, A., Ogren, J. A., Fiebig, M., Laj, P., Li, S. M., Baltensperger, U., et al. (2013). Recommendations for reporting "black carbon" measurements. *Atmospheric*
- Chemistry and Physics, 13(16), 8365–8379. http://dx.doi.org/10.5194/acp-13-8365-2013.
- Petzold, A., & Schönlinner, M. (2004). Multi-angle absorption photometry A new method for the measurement of aerosol light absorption and atmospheric black carbon. *Journal of Aerosol Science*, 35(4), 421–441. http://dx.doi.org/10.1016/j.jaerosci.2003.09.005.
- Philippin, S., Wiedensohler, A., & Stratmann, F. (2004). Measurements of non-volatile fractions of pollution aerosols with an eight-tube volatility tandem differential mobility analyzer (VTDMA-8). *Journal of Aerosol Science*, 35(2), 185–203.
- Pileci, R. E., Modini, R. L., Bertò, M., Yuan, J., Corbin, J. C., Marinoni, A., et al. (2021). Comparison of co-located refractory black carbon (rBC) and elemental carbon (EC) mass concentration measurements during field campaigns at several European sites. Atmospheric Measurement Techniques, 14(2), 1379–1403. http://dx.doi.org/10.5194/amt-14-1379-2021.
- Porod, G. (1951). Die Röntgenkleinwinkelstreuung von dichtgepackten kolloiden systemen: I. Teil. Kolloid-Zeitschrift, 124(2), 83–114. http://dx.doi.org/10.1007/BF01519615.
- Pöschl, U. (2005). Atmospheric aerosols: Ccomposition, transformation, climate and health effects. Angewandte Chemie International Edition, 44(46), 7520–7540. http://dx.doi.org/10.1002/anie.200501122.
- Pósfai, M., Gelencsér, A., Simonics, R., Arató, K., Li, J., Hobbs, P. V., et al. (2004). Atmospheric tar balls: Particles from biomass and biofuel burning. *Journal of Geophysical Research: Atmospheres*, 109(D6), http://dx.doi.org/10.1029/2003JD004169.
- Prasanna, S., Rivière, P., & Soufiani, A. (2014). Effect of fractal parameters on absorption properties of soot in the infrared region. *Journal of Quantitative Spectroscopy and Radiative Transfer*, 148, 141–155.
- Pratsinis, S. E. (1998). Flame aerosol synthesis of ceramic powders. Progress in Energy and Combustion Science, 24(3), 197-219.
- Puri, R., Richardson, T., Santoro, R., & Dobbins, R. (1993). Aerosol dynamic processes of soot aggregates in a laminar ethene diffusion flame. *Combustion and Flame*, 92(3), 320–333.
- Qian, W., Hui, X., Wang, B., Kronenburg, A., Sung, C. J., & Lin, Y. (2023). An investigation into oxidation-induced fragmentation of soot aggregates by Langevin dynamics simulations. Fuel, 334, Article 126547. http://dx.doi.org/10.1016/j.fuel.2022.126547.
- Qiao, Y., Andrews, A. J., Christen, C. E., Olson, B. A., Khariwala, S., MacLachan, B., et al. (2020). Morphological characterization of particles emitted from monopolar electrosurgical pencils. *Journal of Aerosol Science*, 142, Article 105512.
- Quiros, D. C., Hu, S., Lee, E. S., Sardar, S., Wang, X., et al. (2015). Particle effective density and mass during steady-state operation of GDI, PFI, and diesel passenger cars. *Journal of Aerosol Science*, 83, 39–54.
- Rader, D., & McMurry, P. (1986). Application of the tandem differential mobility analyzer to studies of droplet growth or evaporation. *Journal of Aerosol Science*, 17(5), 771–787.
- Rader, D., McMurry, P. H., & Smith, S. (1987). Evaporation rates of monodisperse organic aerosols in the 0.02-to 0.2-μm-diameter range. Aerosol Science and Technology, 6(3), 247–260.
- Radney, J. G., You, R., Ma, X., Conny, J. M., Zachariah, M. R., Hodges, J. T., et al. (2014). Dependence of soot optical properties on particle morphology: measurements and model comparisons. *Environmental Science and Technology*, 48(6), 3169–3176.
- Radney, J. G., & Zangmeister, C. D. (2016). Practical limitations of aerosol separation by a tandem differential mobility analyzer–aerosol particle mass analyzer. *Aerosol Science and Technology*, 50(2), 160–172.
- Ramachandran, G., & Kandlikar, M. (1996). Bayesian analysis for inversion of aerosol size distribution data. Journal of Aerosol Science, 27(7), 1099-1112.
- Rastogi, A., Zivcak, M., Sytar, O., Kalaji, H. M., He, X., Mbarki, S., et al. (2017). Impact of metal and metal oxide nanoparticles on plant: A critical review. Frontiers in Chemistry, 5, 78. http://dx.doi.org/10.3389/fchem.2017.00078.

- Rawat, V. K., Buckley, D. T., Kimoto, S., Lee, M.-H., Fukushima, N., & Hogan Jr., C. J. (2016). Two dimensional size-mass distribution function inversion from differential mobility analyzer-aerosol particle mass analyzer (DMA-APM) measurements. *Journal of Aerosol Science*, 92, 70–82.
- Reavell, K., Hands, T., & Collings, N. (2002). A fast response particulate spectrometer for combustion aerosols. SAE Transactions, http://dx.doi.org/10.4271/2002-01-2714...
- Reimann, J., Kuhlmann, S. A., & Will, S. (2009). 2D aggregate sizing by combining laser-induced incandescence (LII) and elastic light scattering (ELS). Applied Physics B. 96, 583–592.
- Rice, S. B., Chan, C., Brown, S. C., Eschbach, P., Han, L., Ensor, D. S., et al. (2013). Particle size distributions by transmission electron microscopy: An interlaboratory comparison case study. *Metrologia*, 50(6), 663. http://dx.doi.org/10.1088/0026-1394/50/6/663.
- Riemer, N., Ault, A., West, M., Craig, R., & Curtis, J. (2019). Aerosol mixing state: Measurements, modeling, and impacts. *Reviews of Geophysics*, 57(2), 187–249. Rissler, J., Nordin, E. Z., Eriksson, A. C., Nilsson, P. T., Frosch, M., Sporre, M. K., et al. (2014). Effective density and mixing state of aerosol particles in a near-traffic urban environment. *Environmental Science and Technology*, 48(11), 6300–6308.
- Ristimäki, J., Virtanen, A., Marjamäki, M., Rostedt, A., & Keskinen, J. (2002). On-line measurement of size distribution and effective density of submicron aerosol particles. *Journal of Aerosol Science*, 33(11), 1541–1557.
- R'mili, B., Bihan, O. L. C. L., Dutouquet, C., Aguerre-Charriol, O., & Frejafon, E. (2013). Particle sampling by TEM grid filtration. Aerosol Science and Technology, 47(7), 767–775. http://dx.doi.org/10.1080/02786826.2013.789478.
- Rockne, K. J., Taghon, G. L., & Kosson, D. S. (2000). Pore structure of soot deposits from several combustion sources. *Chemosphere*, 41(8), 1125–1135. http://dx.doi.org/10.1016/S0045-6535(00)00040-0.
- Rogak, S. N., & Flagan, R. C. (1992). Bipolar diffusion charging of spheres and agglomerate aerosol particles. *Journal of Aerosol Science*, 23(7), 693–710. http://dx.doi.org/10.1016/0021-8502(92)90037-V.
- Rogak, S. N., Flagan, R. C., & Nguyen, H. V. (1993). The mobility and structure of aerosol agglomerates. Aerosol Science and Technology, 18(1), 25-47.
- Rosner, D. E., & Tandon, P. (2017). Knudsen transition effects on the thermophoretic properties of fractal-like aggregates: Implications for thermophoretic sampling of high-pressure flames. *Aerosol Science and Technology*, 51(11), 1262–1274. http://dx.doi.org/10.1080/02786826.2017.1353061.
- Rothenbacher, S., Messerer, A., & Kasper, G. (2008). Fragmentation and bond strength of airborne diesel soot agglomerates. *Particle and Fibre Toxicology*, 5(9), 4339–4346. http://dx.doi.org/10.1186/1743-8977-5-9.
- Saarikoski, S., Makela, T., Hillamo, R., Aalto, P. P., Kerminen, V., & Kulmala, M. (2005). Physico-chemical characterization and mass closure of size-segregated atmospheric aerosols in hyytiala, Finland. Boreal Environment Research, 10(5), 385.
- Sachdeva, K., & Attri, A. K. (2008). Morphological characterization of carbonaceous aggregates in soot and free fall aerosol samples. Atmospheric Environment, 42(5), 1025–1034.
- Saffaripour, M., Thomson, K. A., Smallwood, G. J., & Lobo, P. (2020). A review on the morphological properties of non-volatile particulate matter emissions from aircraft turbine engines. *Journal of Aerosol Science*, 139, Article 105467. http://dx.doi.org/10.1016/j.jaerosci.2019.105467.
- Samson, R., Mulholland, G. W., & Gentry, J. (1987). Structural analysis of soot agglomerates. Langmuir, 3(2), 272-281.
- Santoro, R., Semerjian, H., & Dobbins, R. (1983). Soot particle measurements in diffusion flames. Combustion and Flame, 51, 203-218.
- Schaefer, D. W., Martin, J. E., Wiltzius, P., & Cannell, D. S. (1984). Fractal geometry of colloidal aggregates. Physical Review Letters, 52(26), 2371.
- Schenk, M., Lieb, S., Vieker, H., Beyer, A., Gölzhäuser, A., Wang, H., et al. (2013). Imaging nanocarbon materials: Soot particles in flames are not structurally homogeneous. *ChemPhysChem*, 14(14), 3248–3254. http://dx.doi.org/10.1002/cphc.201300581.
- Schmid, O., Karg, E., Hagen, D. E., Whitefield, P. D., & Ferron, G. A. (2007). On the effective density of non-spherical particles as derived from combined measurements of aerodynamic and mobility equivalent size. *Journal of Aerosol Science*, 38(4), 431–443.
- Schmidt-Ott, A. (1988). I nsitu measurement of the fractal dimensionality of ultrafine aerosol particles. Applied Physics Letters, 52(12), 954-956.
- Schneider, C. A., Rasband, W. S., & Eliceiri, K. W. (2012). NIH image to imagej: 25 years of image analysis. *Nature Methods*, 9(7), 671–675. http://dx.doi.org/10.1038/nmeth.2089.
- Schnitzler, E., Dutt, A., Charbonneau, A., Olfert, J., & Jaeger, W. (2014). Soot aggregate restructuring due to coatings of secondary organic aerosols derived from aromatic precursors. *Environmental Science and Technology*, 48, 14309–14316. http://dx.doi.org/10.1021/es503699b.
- Schnitzler, E. G., Gac, J. M., & Jäger, W. (2017b). Coating surface tension dependence of soot aggregate restructuring. *Journal of Aerosol Science*, 106, 43–55. http://dx.doi.org/10.1016/j.jaerosci.2017.01.005.
- Schulz, C., Kock, B. F., Hofmann, M., Michelsen, H., Will, S., Bougie, B., et al. (2006). Laser-induced incandescence: recent trends and current questions. *Applied Physics B*, 83, 333–354.
- Schwarz, J. P., Gao, R. S., Fahey, D. W., Thomson, D. S., Watts, L. A., Wilson, J. C., et al. (2006). Single-particle measurements of midlatitude black carbon and light-scattering aerosols from the boundary layer to the lower stratosphere. *Journal of Geophysical Research: Atmospheres, 111*(D16), http://dx.doi.org/10.1029/2006JD007076.
- Scrivner, S., Taylor, T. W., Sorensen, C. M., & Merklin, J. (1986). Soot particle size distribution measurements in a premixed flame using photon correlation spectroscopy. *Applied Optics*, 25(2), 291–297.
- Sedlacek, A. J., Onasch, T. B., Nichman, L., Lewis, E. R., Davidovits, P., Freedman, A., et al. (2018). Formation of refractory black carbon by SP2-induced charring of organic aerosol. Aerosol Science and Technology, 52(12), 1345–1350. http://dx.doi.org/10.1080/02786826.2018.1531107.
- Sengul, A. B., & Asmatulu, E. (2020). Toxicity of metal and metal oxide nanoparticles: A review. *Environmental Chemistry Letters*, 18, 1659–1683. http://dx.doi.org/10.1007/s10311-020-01033-6.
- Shao, W., Zhang, H., & Zhou, H. (2017). Fine particle sensor based on multi-angle light scattering and data fusion. Sensors, 17(5), 1033.
- Shapiro, M., Vainshtein, P., Dutcher, D., Emery, M., Stolzenburg, M., Kittelson, D., et al. (2012). Characterization of agglomerates by simultaneous measurement of mobility, vacuum aerodynamic diameter and mass. *Journal of Aerosol Science*, 44, 24–45.
- Sheridan, P. J., Arnott, W. P., Ogren, J. A., Andrews, E., Atkinson, D. B., Covert, D. S., et al. (2005). The Reno Aerosol Optics Study: An evaluation of aerosol absorption measurement methods. *Aerosol Science and Technology*, 39(1), 1–16. http://dx.doi.org/10.1080/027868290901891.
- Shin, W. G., Mulholland, G. W., Kim, S., Wang, J., Emery, M. S., & Pui, D. Y. (2009). Friction coefficient and mass of silver agglomerates in the transition regime. *Journal of Aerosol Science*, 40(7), 573–587.
- Shu, G., & Charalampopoulos, T. T. (2017). Development of a method to characterize chain-like aggregates in diffusion flames using dynamic light scattering. Applied Optics, 56(4), 1132–1141.
- Simmler, M., Meier, M., Rank, L., Buth, G., Plech, A., & Nirschl, H. (2022). Beamline setup for in situ measurements of particles in turbulent spray flames using small angle X-ray scattering. *Proceedings of the Combustion Institute*.
- Sinclair, D. (1953). Light scattering instruments as an aid in air pollution measurements. Air Repair, 3(1), 51-56.
- Sinclair, D., & La Mer, V. K. (1949). Light scattering as a measure of particle size in aerosols. The production of monodisperse aerosols. *Chemical Reviews*, 44(2), 245–267.
- Sipkens, T. A. (2018). Advances in the modeling of time-resolved laser-induced incandescence (Ph.D. thesis), University of Waterloo.
- Sipkens, T. A., Corbin, J. C., Koukoulas, T., Oldershaw, A., Lavoie, T., Oliaee, J. N., et al. (2022). Comparison of measurement systems for assessing number- and mass-based particle filtration efficiency. *Journal of Occupational and Environmental Hygiene*, 19(10-11), http://dx.doi.org/10.1080/15459624.2022.2114596.
- Sipkens, T. A., Frei, M., Baldelli, A., Kirchen, P., Kruis, F. E., & Rogak, S. N. (2021). Characterizing soot in TEM images using a convolutional neural network. Powder Technology, 387, 313–324.

- Sipkens, T., Mansmann, R., Daun, K., Petermann, N., Titantah, J., Karttunen, M., et al. (2014). In situ nanoparticle size measurements of gas-borne silicon nanoparticles by time-resolved laser-induced incandescence. *Applied Physics B*, 116, 623–636.
- Sipkens, T. A., Menser, J., Dreier, T., Schulz, C., Smallwood, G. J., & Daun, K. J. (2022). Laser-induced incandescence for non-soot nanoparticles: recent trends and current challenges. *Applied Physics B.* 128(4), 1–31. http://dx.doi.org/10.1007/s00340-022-07769-z.
- Sipkens, T., Olfert, J., & Rogak, S. (2020a). Inversion methods to determine two-dimensional aerosol mass-mobility distributions: A critical comparison of established methods. *Journal of Aerosol Science*, 140, Article 105484.
- Sipkens, T., Olfert, J., & Rogak, S. (2020b). Inversion methods to determine two-dimensional aerosol mass-mobility distributions II: Existing and novel Bayesian methods. *Journal of Aerosol Science*, 146, Article 105565.
- Sipkens, T. A., Olfert, J. S., & Rogak, S. N. (2020c). New approaches to calculate the transfer function of particle mass analyzers. Aerosol Science and Technology, 54(1) 111–127
- Sipkens, T., & Rogak, S. (2021). Using k-means to identify soot aggregates in transmission electron microscopy images. *Journal of Aerosol Science*, 152, Article 105699.
- Sipkens, T., Singh, N., & Daun, K. (2017). Time-resolved laser-induced incandescence characterization of metal nanoparticles. Applied Physics B, 123, 1-17.
- Sipkens, T. A., Trivanovic, U., Naseri, A., Bello, O. W., Baldelli, A., Kazemimanesh, M., et al. (2021). Using two-dimensional distributions to inform the mixing state of soot and salt particles produced in gas flares. *Journal of Aerosol Science*, 158, Article 105826.
- Slowik, J. G., Cross, E. S., Han, J. H., Kolucki, J., Davidovits, P., Williams, L. R., et al. (2007). Measurements of morphology changes of fractal soot particles using coating and denuding experiments: Implications for optical absorption and atmospheric lifetime. *Aerosol Science and Technology*, 41(8), 734–750. http://dx.doi.org/10.1080/02786820701432632.
- Smallwood, G. J., Clavel, D., Gareau, D., Sawchuk, R. A., Snelling, D. R., Witze, P. O., et al. (2002). Concurrent quantitative laser-induced incandescence and SMPS measurements of EGR effects on particulate emissions from a TDI diesel engine. SAE Transactions, 1345–1360. http://dx.doi.org/10.4271/2002-01-2715.
- Snelling, D., Link, O., Thomson, K., & Smallwood, G. (2011). Measurement of soot morphology by integrated LII and elastic light scattering. *Applied Physics B*, 104, 385–397.
- Snelling, D. R., Smallwood, G. J., Liu, F., Gülder, Ö. L., & Bachalo, W. D. (2005). A calibration-independent laser-induced incandescence technique for soot measurement by detecting absolute light intensity. *Applied Optics*, 44(31), 6773–6785.
- Song, Y., Pei, X., Liu, H., Zhou, J., & Wang, Z. (2022). Characterization of tandem aerosol classifiers for selecting particles: implication for eliminating the multiple charging effect. Atmospheric Measurement Techniques, 15(11), 3513–3526.
- Sorensen, C. (2001). Light scattering by fractal aggregates: A review. Aerosol Science & Technology, 35(2), 648–687. http://dx.doi.org/10.1080/02786820117868. Sorensen, C. M. (2011). The mobility of fractal aggregates: A review. Aerosol Science and Technology, 45(7), 765–779. http://dx.doi.org/10.1080/02786826.2011. 560909.
- Sorensen, C. M. (2013). Q-space analysis of scattering by particles: A review. Journal of Quantitative Spectroscopy and Radiative Transfer, 131, 3–12. http://dx.doi.org/10.1016/j.jqsrt.2012.12.029.
- Sorensen, C., Cai, J., & Lu, N. (1992a). Light-scattering measurements of monomer size, monomers per aggregate, and fractal dimension for soot aggregates in flames. *Applied Optics*, 31(30), 6547–6557. http://dx.doi.org/10.1364/AO.31.006547.
- Sorensen, C., Cai, J., & Lu, N. (1992b). Test of static structure factors for describing light scattering from fractal soot aggregates. Langmuir, 8(8), 2064-2069.
- Sorensen, C., & Feke, G. (1996). The morphology of macroscopic soot. Aerosol Science and Technology, 25(3), 328-337.
- Sorensen, C. M., Gebhart, J., O'Hern, T. J., & Rader, D. J. (2011). Optical measurement techniques: fundamentals and applications. John Wiley & Sons, Ltd, http://dx.doi.org/10.1002/9781118001684.ch13.
- Sorensen, C., Lu, N., & Cai, J. (1995). Fractal cluster size distribution measurement using static light scattering. *Journal of Colloid and Interface Science*, 174(2), 456–460.
- Sorensen, C., & Wang, G. (1999). Size distribution effect on the power law regime of the structure factor of fractal aggregates. Physical Review E, 60(6), 7143.
- Sorensen, C. M., Yon, J., Liu, F., Maughan, J., Heinson, W. R., & Berg, M. J. (2018). Light scattering and absorption by fractal aggregates including soot. *Journal of Quantitative Spectroscopy and Radiative Transfer*, 217, 459–473. http://dx.doi.org/10.1016/j.jqsrt.2018.05.016.
- Stephens, M., Turner, N., & Sandberg, J. (2003). Particle identification by laser-induced incandescence in a solid-state laser cavity. *Applied Optics*, 42(19), 3726–3736. http://dx.doi.org/10.1364/AO.42.003726.
- Stipe, C. B., Higgins, B. S., Lucas, D., Koshland, C. P., & Sawyer, R. F. (2005). Inverted co-flow diffusion flame for producing soot. *Review of Scientific Instruments*, 76(2), Article 023908. http://dx.doi.org/10.1063/1.1851492.
- Stocker, T. (2014). Climate change 2013: The physical science basis: Working group I contribution to the fifth assessment report of the intergovernmental panel on climate change. Cambridge University Press.
- Stolzenburg, M. R. (1988). An ultrafine aerosol size distribution measuring system (Ph.D. thesis), University of Minnesota.
- Stolzenburg, M. R. (2018). A review of transfer theory and characterization of measured performance for differential mobility analyzers. Aerosol Science and Technology, 52(10), 1194–1218.
- Stolzenburg, M. R., & McMurry, P. H. (1991). An ultrafine aerosol condensation nucleus counter. Aerosol Science and Technology, 14(1), 48–65. http://dx.doi.org/10.1080/02786829108959470.
- Stolzenburg, M. R., & McMurry, P. H. (2008). Equations governing single and tandem DMA configurations and a new lognormal approximation to the transfer function. *Aerosol Science and Technology*, 42(6), 421–432.
- Strobel, R., Baiker, A., & Pratsinis, S. E. (2006). Aerosol flame synthesis of catalysts. Advanced Powder Technology, 17(5), 457–480. http://dx.doi.org/10.1163/156855206778440525.
- Sutcu, E., Doner, N., Liu, F., Ercetin, U., Sen, F., Yon, J., et al. (2020). Morphological and radiative characteristics of soot aggregates: Experimental and numerical research. Scientific Reports, 10(1), 411.
- Świrniak, G., & Mroczka, J. (2022). Forward and inverse analysis for particle size distribution measurements of disperse samples: A review. *Measurement*, 187, Article 110256.
- Symonds, J. P. R., Reavell, K. S., & Olfert, J. S. (2013). The CPMA-electrometer system A suspended particle mass concentration standard. *Aerosol Science and Technology*, 47(8), i-iv. http://dx.doi.org/10.1080/02786826.2013.801547.
- Sztucki, M., Narayanan, T., & Beaucage, G. (2007). In situ study of aggregation of soot particles in an acetylene flame by small-angle x-ray scattering. *Journal of Applied Physics*, 101(11), Article 114304.
- Szymanski, W. W., Nagy, A., & Czitrovszky, A. (2009). Optical particle spectrometry—Problems and prospects. *Journal of Quantitative Spectroscopy and Radiative Transfer*, 110(11), 918–929.
- Szymanski, W. W., Nagy, A., Czitrovszky, A., & Jani, P. (2002). A new method for the simultaneous measurement of aerosol particle size, complex refractive index and particle density. *Measurement Science & Technology*, 13(3), 303.
- Talebi-Moghaddam, S., Bauer, F., Huber, F., Will, S., & Daun, K. (2020). Inferring soot morphology through multi-angle light scattering using an artificial neural network. *Journal of Quantitative Spectroscopy and Radiative Transfer*, 251, Article 106957.
- Talukdar, S. S., & Swihart, M. T. (2003). An improved data inversion program for obtaining aerosol size distributions from scanning differential mobility analyzer data. Aerosol Science and Technology, 37(2), 145–161.
- Tang, X., Wang, C., Zhang, F., Wang, Q., Wang, J., Seifert, S., et al. (2019). Effect of nickel acetylacetonate addition on soot inception and growth in an ethylene flame studied by using in situ small-angle X-ray scattering. *Combustion and Flame*, 206, 390–399.

- Tavakoli, F., & Olfert, J. S. (2013). An instrument for the classification of aerosols by particle relaxation time: Theoretical models of the aerodynamic aerosol classifier. *Aerosol Science and Technology*, 47(8), 916–926. http://dx.doi.org/10.1080/02786826.2013.802761.
- Tavakoli, F., & Olfert, J. S. (2014). Determination of particle mass, effective density, mass-mobility exponent, and dynamic shape factor using an aerodynamic aerosol classifier and a differential mobility analyzer in tandem. *Journal of Aerosol Science*, 75, 35–42. http://dx.doi.org/10.1016/j.jaerosci.2014.04.010.
- Tavakoli, F., Symonds, J. P. R., & Olfert, J. S. (2014). Generation of a monodisperse size-classified aerosol independent of particle charge. *Aerosol Science and Technology*, 48(3), i-iv. http://dx.doi.org/10.1080/02786826.2013.877121.
- Tayali, N., & Bates, C. (1990). Particle sizing techniques in multiphase flows: A review. Flow Measurement and Instrumentation, 1(2), 77-105. http://dx.doi.org/10.1016/0955-5986(90)90032-3.
- Taylor, J. W., Allan, J. D., Liu, D., Flynn, M., Weber, R., Zhang, X., et al. (2015). Assessment of the sensitivity of core / shell parameters derived using the single-particle soot photometer to density and refractive index. Atmospheric Measurement Techniques, 8(4), 1701–1718. http://dx.doi.org/10.5194/amt-8-1701-2015.
- Teoh, W. Y., Amal, R., & Mädler, L. (2010). Flame spray pyrolysis: An enabling technology for nanoparticles design and fabrication. *Nanoscale*, 2(8), 1324–1347. http://dx.doi.org/10.1039/C0NR00017E.
- Thommes, M., Kaneko, K., Neimark, A. V., Olivier, J. P., Rodriguez-Reinoso, F., Rouquerol, J., et al. (2015). Physisorption of gases, with special reference to the evaluation of surface area and pore size distribution (IUPAC Technical Report). *Pure and Applied Chemistry*, 87(9–10), 1051–1069. http://dx.doi.org/10. 1515/pac-2014-1117.
- Thomson, M. J. (2022). Modeling soot formation in flames and reactors: Recent progress and current challenges. *Proceedings of the Combustion Institute*, http://dx.doi.org/10.1016/j.proci.2022.07.263.
- Tian, K., Thomson, K. A., Liu, F., Snelling, D. R., Smallwood, G. J., & Wang, D. (2006). Determination of the morphology of soot aggregates using the relative optical density method for the analysis of TEM images. *Combustion and Flame*, 144(4), 782–791.
- Tikhonov, A. N., & Arseninrs, V. Y. (1977). Solutions of ill-posed problems. V. H. Winston & Sons, http://dx.doi.org/10.1137/102104.
- Todea, A. M., Beckmann, S., Kaminski, H., & Asbach, C. (2015). Accuracy of electrical aerosol sensors measuring lung deposited surface area concentrations.
- Török, S., Malmborg, V. B., Simonsson, J., Eriksson, A., Martinsson, J., Mannazhi, M., et al. (2018). Investigation of the absorption Ångström exponent and its relation to physicochemical properties for mini-CAST soot. *Aerosol Science and Technology*, 52(7), 757–767. http://dx.doi.org/10.1080/02786826.2018. 1457767.
- Török, S., Mannazhi, M., Bergqvist, S., Le, K. C., & Bengtsson, P.-E. (2022). Influence of rapid laser heating on differently matured soot with double-pulse laser-induced incandescence. *Aerosol Science and Technology*, 56(6), 488–501.
- Tran, S., Iida, K., Yashiro, K., Murashima, Y., Sakurai, H., & Olfert, J. S. (2020). Determining the cutoff diameter and counting efficiency of optical particle counters with an aerodynamic aerosol classifier and an inkjet aerosol generator. *Aerosol Science and Technology*, 54(11), 1335–1344. http://dx.doi.org/10.1080/02786826.2020.1777252.
- Trivanovic, U., Kelesidis, G. A., & Pratsinis, S. E. (2022). High-throughput generation of aircraft-like soot. Aerosol Science and Technology, 56(8), 732–743. http://dx.doi.org/10.1080/02786826.2022.2070055.
- Trivanovic, U., Sipkens, T. A., Kazemimanesh, M., Baldelli, A., Jefferson, A. M., Conrad, B. M., et al. (2020). Morphology and size of soot from gas flares as a function of fuel and water addition. Fuel, 279, Article 118478.
- Tropp, R. J., Kuhn, P. J., & Brock, J. R. (1980). A new method for measuring the particle size distribution of aerosols. *Review of Scientific Instruments*, 51(4), 516–520. http://dx.doi.org/10.1063/1.1136227.
- Tsutsui, K., Koya, K., & Kato, T. (1998). An investigation of continuous-angle laser light scattering. Review of Scientific Instruments, 69(10), 3482-3486.
- Twomey, S. (1965). The application of numerical filtering to the solution of integral equations encountered in indirect sensing measurements. *Journal of the Franklin Institute*, 279(2), 95–109.
- Twomey, S. (1975). Comparison of constrained linear inversion and an iterative nonlinear algorithm applied to the indirect estimation of particle size distributions. Journal of Computational Physics, 18(2), 188–200.
- Ueyama, K., Ono, T., Matsukata, M., & Osima, R. (1993). Application of dynamic light scattering based on a monodisperse model as an in-situ method of measuring ultrafine particles growing and aggregating in a flame. *Journal of Chemical Engineering of Japan*, 26(6), 686–691. http://dx.doi.org/10.1252/jcej.26.686.
- Van Gulijk, C., Marijnissen, J., Makkee, M., Moulijn, J., & Schmidt-Ott, A. (2004). Measuring diesel soot with a scanning mobility particle sizer and an electrical low-pressure impactor: performance assessment with a model for fractal-like agglomerates. *Journal of Aerosol Science*, 35(5), 633–655.
- Vander Wal, R. L., & Choi, M. Y. (1999). Pulsed laser heating of soot: morphological changes. *Carbon*, 37(2), 231–239. http://dx.doi.org/10.1016/S0008-6223(98)00169-9.
- Vander Wal, R. L., Tomasek, A. J., Pamphlet, M. I., Taylor, C. D., & Thompson, W. K. (2004). Analysis of HRTEM images for carbon nanostructure quantification. Journal of Nanoparticle Research, 6, 555–568. http://dx.doi.org/10.1007/s11051-004-3724-6.
- Vander Wal, R. L., Yezerets, A., Currier, N. W., Kim, D. H., & Wang, C. M. (2007). HRTEM study of diesel soot collected from diesel particulate filters. *Carbon*, 45(1), 70–77. http://dx.doi.org/10.1016/j.carbon.2006.08.005.
- Varma, R., Moosmüller, H., & Arnott, W. P. (2003). Toward an ideal integrating nephelometer. Optics Letters, 28(12), 1007–1009. http://dx.doi.org/10.1364/OL. 28.001007.
- Verma, P., Pickering, E., Savic, N., Zare, A., Brown, R., & Ristovski, Z. (2019). Comparison of manual and automatic approaches for characterisation of morphology and nanostructure of soot particles. *Journal of Aerosol Science*, 136, 91–105.
- Virtanen, A., Ristimäki, J., Marjamäki, M., Vaaraslahti, K., Keskinen, J., & Lappi, M. (2002). Effective density of diesel exhaust particles as a function of size: Technical Report, SAE Technical Paper, http://dx.doi.org/10.4271/2002-01-0056.
- Volckens, J., & Peters, T. M. (2005). Counting and particle transmission efficiency of the aerodynamic particle sizer. *Journal of Aerosol Science*, 36(12), 1400–1408. http://dx.doi.org/10.1016/j.jaerosci.2005.03.009.
- Voutilainen, A., Kolehmainen, V., & Kaipio, J. (2001). Statistical inversion of aerosol size measurement data. *Inverse Problems in Engineering*, 9(1), 67–94. http://dx.doi.org/10.1080/174159701088027753.
- Voutilainen, A., Stratmann, F., & Kaipio, J. (1999). A new data inversion algorithm for DMPS and TDMA measurements. *Journal of Aerosol Science*, 30, S775–S776. http://dx.doi.org/10.1016/j.jaerosci.2008.07.013.
- Wan, K., Shi, X., & Wang, H. (2021). Quantum confinement and size resolved modeling of electronic and optical properties of small soot particles. *Proceedings of the Combustion Institute*, 38(1), 1517–1524. http://dx.doi.org/10.1016/j.proci.2020.07.145.
- Wang, C., Chan, Q. N., Zhang, R., Kook, S., Hawkes, E. R., Yeoh, G. H., et al. (2016). Automated determination of size and morphology information from soot transmission electron microscope (TEM)-generated images. *Journal of Nanoparticle Research*, 18(5), 1–15. http://dx.doi.org/10.1007/s11051-016-3434-x.
- Wang, X., Chancellor, G., Evenstad, J., Farnsworth, J. E., Hase, A., Olson, G. M., et al. (2009). A novel optical instrument for estimating size segregated aerosol mass concentration in real time. Aerosol Science and Technology, 43(9), 939–950.
- Wang, S. C., & Flagan, R. C. (1990). Scanning electrical mobility spectrometer. Aerosol Science and Technology, 13(2), 230–240. http://dx.doi.org/10.1080/02786829008959441.
- Wang, L., Li, F., & Xing, J. (2017). A hybrid artificial bee colony algorithm and pattern search method for inversion of particle size distribution from spectral extinction data. *Journal of Modern Optics*, 64(19), 2051–2065.

- Wang, M., Tang, Q., Mei, J., & You, X. (2018). On the effective density of soot particles in premixed ethylene flames. *Combustion and Flame*, 198, 428–435. http://dx.doi.org/10.1016/j.combustflame.2018.10.004.
- Wang, H., Zhao, B., Wyslouzil, B., & Streletzky, K. (2002). Small-angle neutron scattering of soot formed in laminar premixed ethylene flames. *Proceedings of the Combustion Institute*, 29(2), 2749–2757.
- Wang, S., Zhou, K., Lu, X., Chen, H., Yang, F., Li, Q., et al. (2021). Measurement of density and shape for single black carbon aerosols in a heavily Polluted Urban Area. Aerosol and Air Quality Research, 21(12), Article 210162. http://dx.doi.org/10.4209/aaqr.210162.
- Weeks, R., & Duley, W. (1974). Aerosol-particle sizes from light emission during excitation by TEA CO2 laser pulses. *Journal of Applied Physics*, 45(10), 4661–4662. Weingartner, E., Baltensperger, U., & Burtscher, H. (1995). Growth and structural change of combustion aerosols at high relative humidity. *Environmental Science and Technology*, 29(12), 2982–2986.
- Weingartner, E., Burtscher, H., & Baltensperger, U. (1997). Hygroscopic properties of carbon and diesel soot particles. Atmospheric Environment, 31(15), 79. http://dx.doi.org/10.1016/S1352-2310(97)00023-X.
- Wentzel, M., Gorzawski, H., Naumann, K. H., Saathoff, H., & Weinbruch, S. (2003). Transmission electron microscopical and aerosol dynamical characterization of soot aerosols. *Journal of Aerosol Science*, 34(10), 1347–1370.
- Whitby, K. T., & Vomela, R. A. (1967). Response of single particle optical counters to nonideal particles. *Environmental Science and Technology*, 1(10), 801–814. Wiedensohler, A. (1988). An approximation of the bipolar charge distribution for particles in the submicron size range. *Journal of Aerosol Science*, 19(3), 387–389. http://dx.doi.org/10.1016/0021-8502(88)90278-9.
- Wiedensohler, A., Wiesner, A., Weinhold, K., Birmili, W., Hermann, M., Merkel, M., et al. (2018). Mobility particle size spectrometers: Calibration procedures and measurement uncertainties. *Aerosol Science and Technology*, 52(2), 146–164. http://dx.doi.org/10.1080/02786826.2017.1387229.
- Will, S., Schraml, S., & Leipert, A. (1996). Comprehensive two-dimensional soot diagnostics based on laser-induced incandescence (LII). Symposium (International) on Combustion, 26(2), 2277–2284. http://dx.doi.org/10.1016/S0082-0784(96)80055-5.
- Wilson, J. C., & Liu, B. Y. (1980). Aerodynamic particle size measurement by laser-doppler velocimetry. *Journal of Aerosol Science*, 11(2), 139–150. http://dx.doi.org/10.1016/0021-8502(80)90030-0.
- Winklmayr, W., Wang, H. C., & John, W. (1990). Adaptation of the twomey algorithm to the inversion of cascade impactor data. Aerosol Science and Technology, 13(3), 322–331.
- Wolfenbarger, J. K., & Seinfeld, J. H. (1990). Inversion of aerosol size distribution data. Journal of Aerosol Science, 21(2), 227-247.
- Wozniak, M., Onofri, F., Barbosa, S., Yon, J., & Mroczka, J. (2012). Comparison of methods to derive morphological parameters of multi-fractal samples of particle aggregates from TEM images. *Journal of Aerosol Science*, 47, 12–26.
- Wu, J. S., Krishnan, S., & Faeth, G. (1997). Refractive indices at visible wavelengths of soot emitted from buoyant turbulent diffusion flames. ournal of Heat Transfer, 119(2), 230–237. http://dx.doi.org/10.1115/1.2824213.
- Xiao, K., Swanson, J. J., Pui, D. Y. H., & Kittelson, D. B. (2012). Bipolar diffusion charging of aggregates. Aerosol Science and Technology, 46(7), 794–803. http://dx.doi.org/10.1080/02786826.2012.667585.
- Xu, R. (2015). Light scattering: A review of particle characterization applications. Particuology, 18, 11-21. http://dx.doi.org/10.1016/j.partic.2014.05.002.
- Xu, L., He, Z., Zhao, Q., Mao, J., & Fu, Y. (2021). A machine learning algorithm for retrieving the geometrical characteristic parameters of soot fractal aggregates from polarized light signal. *Optik*, 236, Article 166473.
- Xue, H., Khalizov, A. F., Wang, L., Zheng, J., & Zhang, R. (2009). Effects of coating of dicarboxylic acids on the mass-mobility relationship of soot particles. Environmental Science and Technology, 43(8), 2787–2792. http://dx.doi.org/10.1021/es803287v.
- Yang, B., & Koylu, U. O. (2005). Soot processes in a strongly radiating turbulent flame from laser scattering/extinction experiments. *Journal of Quantitative Spectroscopy and Radiative Transfer*, 93(1–3), 289–299.
- Yao, Q., Asa-Awuku, A., Zangmeister, C. D., & Radney, J. G. (2020). Comparison of three essential sub-micrometer aerosol measurements: Mass, size and shape. Aerosol Science and Technology, 54(10), 1197–1209.
- Ye, M., Wang, S., Lu, Y., Hu, T., Zhu, Z., & Xu, Y. (1999). Inversion of particle-size distribution from angular light-scattering data with genetic algorithms. *Applied Optics*, 38(12), 2677–2685.
- Yon, J., Bescond, A., & Liu, F. (2015). On the radiative properties of soot aggregates part 1: Necking and overlapping. *Journal of Quantitative Spectroscopy and Radiative Transfer*, 162, 197–206. http://dx.doi.org/10.1016/j.jqsrt.2015.03.027.
- Yon, J., Liu, F., Bescond, A., Caumont-Prim, C., Rozé, C., Ouf, F. X., et al. (2014). Effects of multiple scattering on radiative properties of soot fractal aggregates. Journal of Quantitative Spectroscopy and Radiative Transfer, 133, 374–381.
- Yon, J., Morán, J., Lespinasse, F., Escudero, F., Godard, G., Mazur, M., et al. (2021). Horizontal planar angular light scattering (HPALS) characterization of soot produced in a laminar axisymmetric coflow ethylene diffusion flame. Combustion and Flame, 232, Article 111539.
- Yon, J., Morán, J., Ouf, F. X., Mazur, M., & Mitchell, J. (2021). From monomers to agglomerates: A generalized model for characterizing the morphology of fractal-like clusters. *Journal of Aerosol Science*, 151, Article 105628.
- Yon, J., Ouf, F. X., Hebert, D., Mitchell, J. B., Teuscher, N., Le Garrec, J. L., et al. (2018). Investigation of soot oxidation by coupling LII, SAXS and scattering measurements. Combustion and Flame, 190, 441–453.
- Yuan, Y., Yi, H. L., Shuai, Y., Wang, F. Q., & Tan, H. P. (2010). Inverse problem for particle size distributions of atmospheric aerosols using stochastic particle swarm optimization. *Journal of Quantitative Spectroscopy and Radiative Transfer*, 111(14), 2106–2114.
- Zangmeister, C. D., Radney, J. G., Dockery, L. T., Young, J. T., Ma, X., You, R., et al. (2014). Packing density of rigid aggregates is independent of scale. Proceedings of the National Academy of Sciences, 111(25), 9037–9041.
- Zelenyuk, A., Cai, Y., & Imre, D. (2006). From agglomerates of spheres to irregularly shaped particles: Determination of dynamic shape factors from measurements of mobility and vacuum aerodynamic diameters. *Aerosol Science and Technology*, 40(3), 197–217. http://dx.doi.org/10.1080/02786820500529406.
- Zelenyuk, A., & Imre, D. (2007). On the effect of particle alignment in the DMA. Aerosol Science and Technology, 41(2), 112-124.
- Zeng, J., Bian, A., Chen, A., Xu, W., Cheng, W., Yan, S., et al. (2023). A miniaturized aerosol sizing sensor using light-scattering angular spectrum. *Optics and Lasers in Engineering*, 160, Article 107257.
- Zhang, S. H., Akutsu, Y., Russell, L. M., Flagan, R. C., & Seinfeld, J. H. (1995). Radial differential mobility analyzer. Aerosol Science and Technology, 23(3), 357–372. http://dx.doi.org/10.1080/02786829508965320.
- Zhang, S. H., & Flagan, R. C. (1996). Resolution of the radial differential mobility analyzer for ultrafine particles. Journal of Aerosol Science, 27(8), 1179–1200.
 Zhang, C., Heinson, W. R., Liu, P., Beeler, P., Li, Q., Jiang, J., et al. (2020). Three-dimensional tomography reveals distinct morphological and optical properties of soot aggregates from coal-fired residential stoves in China. Journal of Quantitative Spectroscopy and Radiative Transfer, 254, Article 107184. http://dx.doi.org/10.1016/j.jqsrt.2020.107184.
- Zhang, R., Khalizov, A. F., Pagels, J., Zhang, D., Xue, H., & McMurry, P. H. (2008). Variability in morphology, hygroscopicity, and optical properties of soot aerosols during atmospheric processing. *Proceedings of the National Academy of Sciences*, 105(30), 10291–10296.
- Zhang, J. Y., Qi, H., Ren, Y. T., & Ruan, L. M. (2018). Simultaneous identification of optical constants and PSD of spherical particles by multi-wavelength scattering-transmittance measurement. Optical Communications, 413, 317–328.
- Zhang, J. Y., Qi, H., Wang, Y. F., Gao, B. H., & Ruan, L. M. (2019). Retrieval of fractal dimension and size distribution of non-compact soot aggregates from relative intensities of multi-wavelength angular-resolved light scattering. Optics Express, 27(2), 1613–1631.
- Zhang, H., Sorensen, C., Ramer, E., Olivier, B., & Merklin, J. (1988). In situ optical structure factor measurements of an aggregating soot aerosol. *Langmuir*, 4(4), 867–871.

- Zhang, C., Thajudeen, T., Larriba, C., Schwartzentruber, T. E., & Hogan Jr., C. J. (2012). Determination of the scalar friction factor for nonspherical particles and aggregates across the entire knudsen number range by direct simulation Monte Carlo (DSMC). Aerosol Science and Technology, 46(10), 1065–1078. http://dx.doi.org/10.1080/02786826.2012.690543.
- Zhang, F., Wang, C., Han, W., Zou, Y., Wang, J., Seifert, S., et al. (2021). Soot formation and growth with palladium acetylacetonate-toluene injection in ethylene base flames investigated by in situ synchrotron small-angle X-ray scattering. *Proceedings of the Combustion Institute, 38*(1), 1859–1866. http://dx.doi.org/10.1016/j.proci.2020.10.004.
- Zhao, B., Uchikawa, K., & Wang, H. (2007). A comparative study of nanoparticles in premixed flames by scanning mobility particle sizer, small angle neutron scattering, and transmission electron microscopy. *Proceedings of the Combustion Institute*, 31(1), 851–860. http://dx.doi.org/10.1016/j.proci.2006.08.064.
- Zhao, W., Zhao, G., Li, Y., Guo, S., Ma, N., Tang, L., et al. (2022). New method to determine black carbon mass size distribution. *Atmospheric Measurement Techniques Discussions*, 1–15. http://dx.doi.org/10.5194/amt-15-6807-2022.
- Zhao, G., Zhao, W., & Zhao, C. (2019). Method to measure the size-resolved real part of aerosol refractive index using differential mobility analyzer in tandem with single-particle soot photometer. Atmospheric Measurement Techniques, 12(7), 3541–3550.
- Zinky, W. R. (1962). A new tool for air pollution control: The aerosol particle counter. Journal of the Air Pollution Control Association, 12(12), 578-583.